MODELING OF HIGH STRAIN RATE COMPRESSION OF AUSTENITIC SHAPE MEMORY ALLOYS

Hao Yu

Dissertation Prepared for the Degree of

DOCTOR OF PHILOSOPHY

UNIVERSITY OF NORTH TEXAS

December 2017

APPROVED:

Marcus L. Young, Major Professor
Jincheng Du, Committee Member
Samir Aouadi, Committee Member
Sundeep Mukherjee, Committee Member
Srinivasan Srivilliputhur, Committee Member
Andrey Voevodin, Chair of the Department of Materials Science and Engineering
Costas Tsatsoulis, Dean of the College of Engineering
Victor Prybutok, Dean of the Toulouse Graduate School

Yu, Hao. *Modeling of High Strain Rate Compression of Austenitic Shape Memory Alloys*. Doctor of Philosophy (Materials Science and Engineering), December 2017, 166 pp., 4 tables, 60 figures, chapter references.

Shape memory alloys (SMAs) exhibit the ability to absorb large dynamic loads and, therefore, are excellent candidates for structural components where impact loading is expected. Compared to the large amount of research on the shape memory effect and/or pseudoelasticity of polycrystalline SMAs under quasi-static loading conditions, studies on dynamic loading are limited. Experimental research shows an apparent difference between the quasi-static and high strain rate deformation of SMAs. Research reveals that the martensitic phase transformation is strain rate sensitive. The mechanism for the martensitic phase transformation in SMAs during high strain rate deformation is still unclear. Many of the existing high strain rate models assume that the latent heat generated during deformation contributes to the change in the stress-strain behavior during dynamic loading, which is insufficient to explain the large stress observed during phase transformation under high strain rate deformation. Meanwhile, the relationship between the phase front velocity and strain rate has been studied. In this dissertation, a new resistance to phase transformation during high strain rate deformation is discussed and the relationship between the driving force for phase transformation and phase front velocity is established. With consideration of the newly defined resistance to phase transformation, a new model for phase transformation of SMAs during high strain rate deformation is presented and validated based on experimental results from an austenitic NiTi SMA. Stress, strain, and martensitic volume fraction distribution during high strain rate deformation are simulated using finite element analysis software ABAQUS/standard. For the first time, this dissertation presents a theoretical study of the microscopic band structure during high strain rate compressive deformation. The microscopic transformation band is generated by the phase front and leads to minor fluctuations in sample deformation. The strain rate effect on phase transformation is

studied using the model. Both the starting stress for transformation and the slope of the stress-strain curve during phase transformation increase with increasing strain rate.

Copyright 2017

By

Hao Yu

ACKNOWLEDGMENTS

First, I thank my parents for giving me life. They are my shields when I am down. They always give me the best they can to help me.

I also thank my advisor, Dr. Marcus L. Young, for choosing me as his first PhD student at the University of North Texas. He teaches me to think critically when I do research. I am extremely grateful for his patience when I work ‘slowly.’ He teaches me never to give up. His attitude to work and life inspires me and benefits me in all aspects of my life. Dr. Young also provided financial startup funds to support this research.

Furthermore, I thank Dr. Xu Nie for help with Kolsky compression bar experiments and Scott Schlegel (ATI Specialty Alloys and Components, Albany, Oregon) and Brian Van Doren (Specialty Alloys and Components, Albany, Oregon) for providing NiTi SMA rods. I also gratefully acknowledge the Center for Advanced Research and Technology at University of North Texas for access to experimental facilities used for this study. I thank Sylvia Konrath for editorial help. I also give thanks to Dr. Haitao Jiang in University of Science and Technology, Beijing, for academic help.

I thank my committee members for academic help during my study at UNT. And last but certainly not least, I thank group members, Matthew Carl, Nathan Ley, Silvia Briseno Murguia; and my friends, Ying Qiu, Zhenghang Zhao, Jinglei Wu, Chuangwei Liu, Zhiguang Ding, Baozhuo Zhang for all their help and company.

TABLE OF CONTENTS

LIST OF TABLES

LIST OF FIGURES

CHAPTER 1

INTRODUCTION

1.1 Motivation

Demands for "new-age" materials for innovative applications and novel materials with excellent properties have developed in the last several decades since the early 1960s. Shape memory alloys (SMAs) represent one set of 'smart materials' that have been used widely in aerospace, automotive, civil engineering, and biomedical fields [1, 2]. Typical properties of SMAs include high strength [3, 4], good corrosion resistance [5, 6], and excellent biocompatibility [2, 7]. Furthermore, as compared to traditional alloys, SMAs are well-known for their unique ability to return to predefined shapes, due to a reversible martensitic phase transformation driven by stress, temperature, or a magnetic field [8, 9].

When an SMA (e.g., NiTi) is deformed above the austenite finish temperature (A_f), the cubic austenitic structure transforms to a low-symmetry, monoclinic martensitic structure. Upon unloading, phase transformation results in about 6% to 10% recoverable strain, which is termed pseudoelasticity or superelasticity. When an SMA is deformed below the martensite finish temperature (M_s), reorientation of martensitic variants is activated to accommodate the loading strains, leading to fully recoverable shape change of the alloy by heating above the austenite finish temperature (A_f), which is termed the "shape memory effect."

For nearly four decades since SMAs were innovated in the 1960s, research has focused on the mechanical properties of SMAs under quasi-static deformation [10-12]. SMAs were designed for biomedical applications (e.g., eyeglass frames [13], arch wires for orthodontic correction [14, 15], and self-expanding stents [16]) or as shape memory actuators and sensors

[17] where dynamic properties of alloys are insignificant. In the past two decades since approximately 2000, interest in extending SMAs to high strain rate applications such as seismic damping, blast-mitigation or energy-absorbing devices in earthquake engineering [18-22] has grown. Much research has focused on the quasi-static mechanical properties of these materials [10-12]. Limited study of the mechanical properties of SMAs under high strain rates has curtailed further application of these materials in the aerospace and defense industries. At high strain rates, deformation occurs within a relatively short time, making it very difficult to measure experimentally. Therefore, it is difficult to analyze the microstructural evolution within the SMA. Computer modeling of the behaviors of materials is then applied to study the stress, strain, and martensitic volume fraction distribution during deformation. The objective of the present research is to develop a new model for SMAs under high strain rate deformation.

1.2 Contributions of the Dissertation

The three major contributions in the present research include the following. (1) Models for quasi-static deformation of SMAs have been established absolutely. In the case of dynamic compressive loading, transformation stresses are more sensitive to the latent heat of transformation and heat of deformation, since this energy cannot be dissipated in such a short time interval. Therefore, in current theoretical research on dynamic deformation of SMAs, quasi-static models were applied to simulate high strain rate deformation by modifying heat transfer equations. At the same time, dislocations generated during high strain rate deformation contribute substantially to the integrity of the constitutive relationship of SMAs.

The driving force for the phase transformation is related to the phase front velocity. The influence of dislocations and phase front velocity on the driving force for phase transformation is considered in the present research. A new model for high strain rate deformation of SMAs is also established. (2) During high strain rate compression, the sample is deformed by a compressive stress wave. Different from microstructural evolution during tensile deformation, no macroscopic band structure was observed experimentally. At the same time, stress wave propagation within the sample leads to heterogeneous stress distribution in the propagation direction, and to the subsequent microscopic band structure. The microscopic band structure during phase transformation is simulated for the first time. (3) The influence of temperature on the stress-strain curve has been studied experimentally in high strain rate deformation of austenitic and martensitic SMAs. Limited experimental techniques have precluded in-depth studies of the influence of strain rate on material flows during deformation. In the present research, the influence of high strain rate on material flows is studied theoretically, and the effect of strain rate on martensite finish temperature (M_f) is studied.

1.3 Arrangement of the Dissertation

The seven chapters of the dissertation are arranged as follows:

Chapter 1 summarizes the motivation and contributions of the present research. Chapter 2 provides background by introducing briefly the history of SMAs. The phase diagram and crystal structure of the different phases and precipitates in SMAs systems are discussed. The physical metallurgy and processing of NiTi alloys are discussed next. Research on the

mechanical properties of NiTi SMAs are then reviewed. Finally, phase transformation theory and various models for SMAs are introduced and briefly discussed. Chapter 3 presents a one-dimensional thermomechanical model for high strain rate deformation of austenitic shape memory alloys. For the first time, in this model, phase front velocity is related to the driving force for phase transformation. Chapter 4 describes finite element simulation of material flow during high strain rate deformation of NiTi austenitic shape memory alloys. The formation of microscopic band structure is discussed, and the influence of high strain rate on material flow is studied theoretically. Chapter 5 introduces the temperature effect on high strain rate deformation of austenitic shape memory alloys. The influence of temperature on material flow during high strain rate deformation is studied theoretically. Chapter 6 presents the conclusions and future research. Chapter 7 reports dissertation appendix data. Finally, additional characteristic experimental data related to microstructural evolution during high strain rate deformation of austenitic SMA is presented.

1.4 References

[1] Barbarino S, Flores ES, Ajaj RM, Dayyani I, Friswell MI. Smart Materials and Structures 2014;23:063001.

[2] Jani JM, Leary M, Subic A, Gibson MA. Materials & Design 2014;56:1078.

[3] Pushin V, Stolyarov V, Valiev R, Kourov N, Kuranova N, Prokof'ev E, Yurchenko L. Physics of metals and metallography 2002;94:S54.

[4] Flomenblit J, Budigina N, Richter J. High strength medical devices of shape memory alloy. Google Patents, 1999.

[5] Starosvetsky D, Gotman I. Biomaterials 2001;22:1853.

[6] Rondelli G. Biomaterials 1996;17:2003.

[7] Morgan N. Materials Science and Engineering: A 2004;378:16.

[8] Otsuka K, Wayman CM. Shape memory materials: Cambridge university press, 1999.

[9] Otsuka K, Ren X. Intermetallics 1999;7:511.

[10] Chen WW, Wu Q, Kang JH, Winfree NA. International Journal of Solids and Structures 2001;38:8989.

[11] Kockar B, Karaman I, Kim JI, Chumlyakov YI, Sharp J, Yu CJ. Acta Materialia 2008;56:3630.

[12] Benafan O, Brown J, Calkins FT, Kumar P, Stebner AP, Turner TL, Vaidyanathan R, Webster J, Young ML. International Journal of Mechanics and Materials in Design 2013;10:1.

[13] Zider RB, Krumme JF. Eyeglass frame including shape-memory elements. Google Patents, 1988.

[14] Gil F, Planell J. Journal of Biomedical Materials Research Part A 1999;48:682.

[15] Duerig TW, Melton K, Stöckel D. Engineering aspects of shape memory alloys: Butterworth-Heinemann, 2013.

[16] Stoeckel D, Pelton A, Duerig T. European radiology 2004;14:292.

[17] Kahn H, Huff M, Heuer A. Journal of Micromechanics and Microengineering 1998;8:213.

[18] Dolce M, Cardone D. International Journal of Mechanical Sciences 2001;43:2657.

[19] Van Humbeeck J. Journal of Alloys and Compounds 2003;355:58.

[20] Fugazza D. Shape-memory alloy devices in earthquake engineering: mechanical

properties, constitutive modelling and numerical simulations. Istituto Universitario di Studi Superiori di Pavia, 2003.

[21] Saadat S, Salichs J, Noori M, Hou Z, Davoodi H, Bar-On I, Suzuki Y, Masuda A. Smart materials and structures 2002;11:218.

[22] Dolce M, Cardone D. International Journal of Mechanical Sciences 2001;43:2631.

CHAPTER 2

BACKGROUND

2.1 History of SMAs

Rubber-like behavior in an Au-47.5Cd alloy was first discovered by Arne Ölander in 1932 [1, 2]. When Ölander and co-workers tested the gold-cadmium alloy, the material was found to deform when cooled and return to its original shape when heated. Similar behavior in CuZn alloys was later observed by Greninger and Mooradian in 1938 [3]. The crystallographic orientation and kinetics of reversible martensitic transformation were studied by Kurdyumov and Khandros in 1949 [4]. In 1951, Chang and Read termed this behavior the shape memory effect [5]. Extensive research was then applied in this area, and more and more alloys, including AuCd and AuAgCd, were determined to exhibit the shape memory effect. A breakthrough in the field of shape memory alloys occurred when the same effect was observed in equiatomic NiTi alloys by Buehler and his co-workers at the US Naval Ordnance Laboratory [6-8]. The relatively low cost, as compared to Au-based SMAs, and superior shape memory behavior and structural properties make NiTi alloys attractive for practical applications. Compared to copper-based SMAs (e.g., Cu-Al-Ni [9], Cu-Zr [10], Cu-Zn-Al [11], et al.) and iron-based SMAs (e.g., Fe-Mn-Si [12]) which are brittle in nature, NiTi-based SMAs show good strength and ductility. Therefore, more than 90% of all SMA applications are based on NiTi or ternary NiTiX (X=Cu, Nb, Fe, or Co, et al.) [13-15].

Due to their nearly unparalleled biocompatibility, NiTi-based SMAs were developed for bio-medical applications such as stents [16], orthodontic wire [14, 17], and implants [14]. Since the late 1990s, NiTi SMAs were extended to non-medical applications such as smart

actuators [18], devices for proportional control [14], hinges for solar panel deployment [19], and variable geometry chevrons in aerospace actuation applications [13, 20].

2.2 Phase Diagram of NiTi SMAs

To better understand the microstructure and properties of NiTi SMAs, the phase diagram is introduced in this chapter. A phase diagram is important for the scientist to tune the properties of materials through heat treatments. The Ni-Ti phase diagram was initially studied by Hunter and Bacon [21] when they measured the conductivity of NiTi alloys. Later, Vogel and Wallbaum [22] reported the eutectic $TiNi_3$ in a Ni-rich NiTi system. Another compound Ti_2Ni was reported by Laves and Wallbaum [23, 24] through X-ray investigation. However, the reaction from TiNi to Ti_2Ni and $TiNi_3$ was controversial until Duwez and Taylor [25] initially observed the decomposition of TiNi into Ti_2Ni and $TiNi_3$ at 800 ℃. Phase structure in the system was later studied by Poole and Hume-Rothery [26], who observed reversible phase transformation from high temperature NiTi phase to a hexagonal phase at 36 ℃. Based on their works, Hansen and Anderko [27] established the Ni-Ti phase diagram. Wasilewski et al. [28] identified a new phase Ti_2Ni_3 using XRD and electron probe microanalysis (EPMA). Koskimaki et al. [29] studied the phase of NiTi aged below 625 ℃ and observed a plate-shaped precipitate they termed $Ti_{11}Ni_{14}$, which other researchers later identified as Ti_3Ni_4. Therefore, different phases, such as Ti_2Ni, $TiNi_3$, Ti_2Ni_3, Ti_3Ni_4, and martensitic NiTi, have been identified in Ni-Ti phase diagram. The equilibrium Ni-Ti diagram is shown in Fig. 2.1 [30, 31].

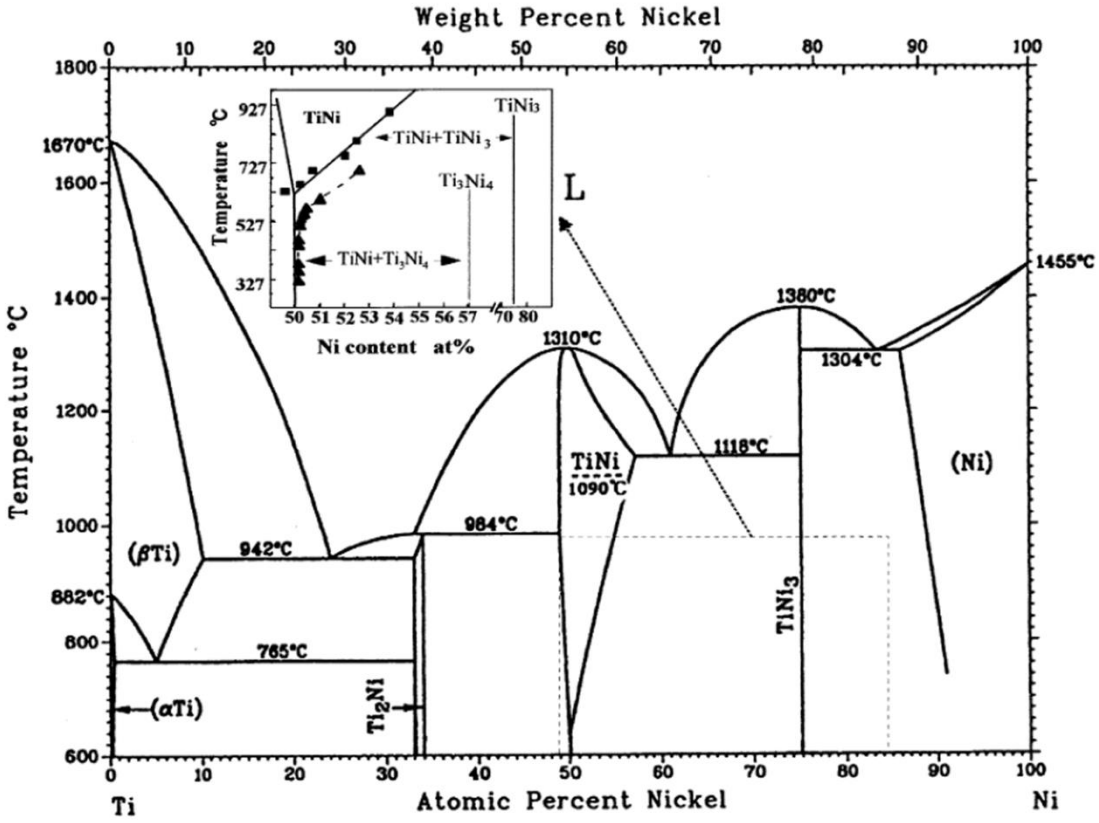

Fig. 2.1 Ni-Ti equilibrium phase diagram [30,31]

Heat treatment was applied on SMAs to improve their mechanical properties. An equilibrium phase diagram is not convenient to study phase transformation by heat treatment. Therefore, an isothermal transformation diagram (also known as time-temperature-transformation (TTT) diagram) was established to study phase transformation under different heat treatment procedures. Nishida et al. [32] studied phase transformation of Ni-rich Ti-52Ni alloys during aging heat treatment. The precipitate, Ti_3Ni_4, is observed when heat-treated at low temperature for a short time. When the sample is aged at high temperature for a long time, $TiNi_3$ phase is observed. When the sample is heat-treated at intermediary aging temperature and time, Ti_2Ni_3 precipitates form. Nishida et al. [32] also studied phase transformation by continual aging and learned that prior-formed Ti_3Ni_4 dissolved into a matrix with the formation of Ti_2Ni_3 precipitates with continued aging. The

Ti_2Ni_3 precipitates will finally dissolve into the matrix with the formation of $TiNi_3$ precipitates. The TTT diagram is shown in Fig. 2.2. Similarly, Kainuma et al. [33] provided TTT diagrams for Ti-52Ni, Ti-54Ni, and Ti-56Ni alloys.

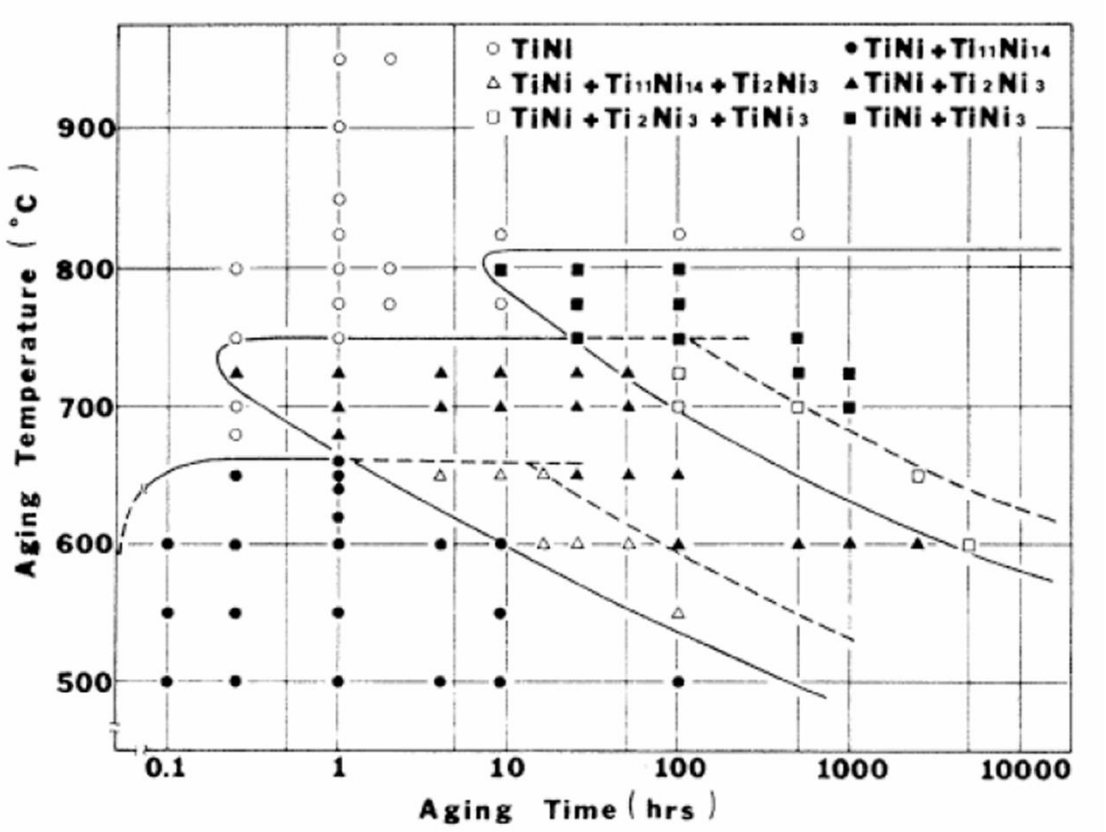

Fig. 2.2 TTT diagram for Ti-52Ni during aging [32]

2.3 Crystal Structures of Different Phases

The crystal structures of NiTi SMAs are discussed in detail by Huang et al. [34]. In their work, the structures of NiTi SMAs are modeled by first-principles calculations based on density function theory (Fig. 2.3). At relatively high temperature, NiTi is stable with *B2* structure. Huang et al. [34] observed three structures with lower energy when distorting cubic *B2* structure: the orthorhombic *B19* structure with space group *Pmma*; the monoclinic *B19'* phase with space group $P2_1/m$; and *R* phase space group *P3*. They also observed that *B19*

structure is mechanically unstable against monoclinic *B19'* structure. Different from experimental observations, the angle associated with minimum energy distortion is 107 °rather than 98 °. The authors also claim that a new phase with base-centered orthorhombic (BCO) structure is observed theoretically. The lattice parameters of these phases are shown in Table 2.1.

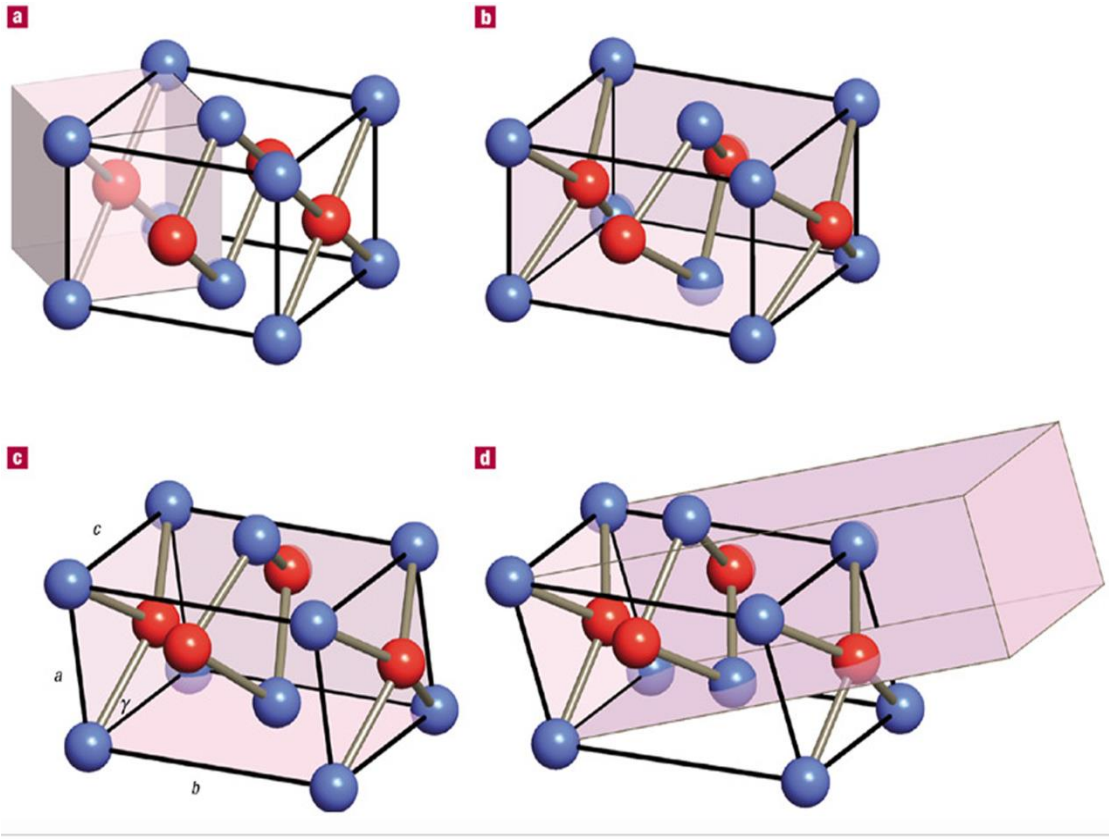

Fig.2.3 (a) The relation between the cubic *B*2 cell (shaded box) and the undistorted (tetragonal) *B*19 cell. (b) The orthorhombic *B*19 structure. (c) The distortion to the stress-stabilized *B*19' structure. (d) The BCO minimum-energy structure with further doubled conventional cell (shaded box). [34]

R phase is attractive to researchers for such special properties as small hysteresis width. Such *R* phase was first observed by Hwang et al. [35] and later well-studied by other researchers [36-38]. *R* phase is generated by the distortion of *B2* structure along <111> directions. The crystal structure of *R* phase is shown in Fig. 2.4 [39].

Table 2.1 Structural parameters relative to B2 for NiTi in the B2, B19 and B19′ structures

Structures	*a*	*b*	*c*	*γ*
B2(TMPP-LDA)	2.981	4.216	4.216	90
B2(USPP-LDA)	2.949	4.171	4.171	90
B2(USPP-GGAA)	3.009	4.255	4.255	90
B2(PAW-LDA)	2.937	4.154	4.154	90
B2(YCH-LDA)	2.977	4.210	4.210	90
B2(GS)	3.015	4.264	4.264	90
B19(TMPP-LDA)	2.817	4.573	4.112	90
B19(USPP-LDA)	2.657	4.567	4.178	90
B19(PAW-LDA)	2.637	4.557	4.170	90
B19(USPP-GGA)	2.776	4.631	4.221	90
B19(YCH-LDA)	2.859	4.582	4.078	90
BCO(TMPP-LDA)	2.918	4.891	3.943	107.2
BCO(USPP-LDA)	2.864	4.838	3.933	107.2
BCO(PAW-LDA)	2.851	4.815	3.921	107.2
BCO(USPP-GGA)	2.940	4.936	3.997	107.0
B19’(USPP-LDA)	2.861	4.600	3.970	97.8
B19’(USPP-GGA)	2.929	4.686	4.048	97.8
B19’(YCH-LDA)	2.892	4.598	4.049	97.8
B19’(KTMO)	2.898	4.646	4.108	97.8
B19’(MS)	2.885	4.622	4.120	96.8

When NiTi is heat-treated, three typical precipitates will be generated with different temperatures and times. Among these precipitates, Ni_4Ti_3 precipitate is critical for its influence on the mechanical properties of NiTi SMAs [40-44]. The Ni_4Ti_3 precipitate has a lenticular shape and a rhombohedral structure.

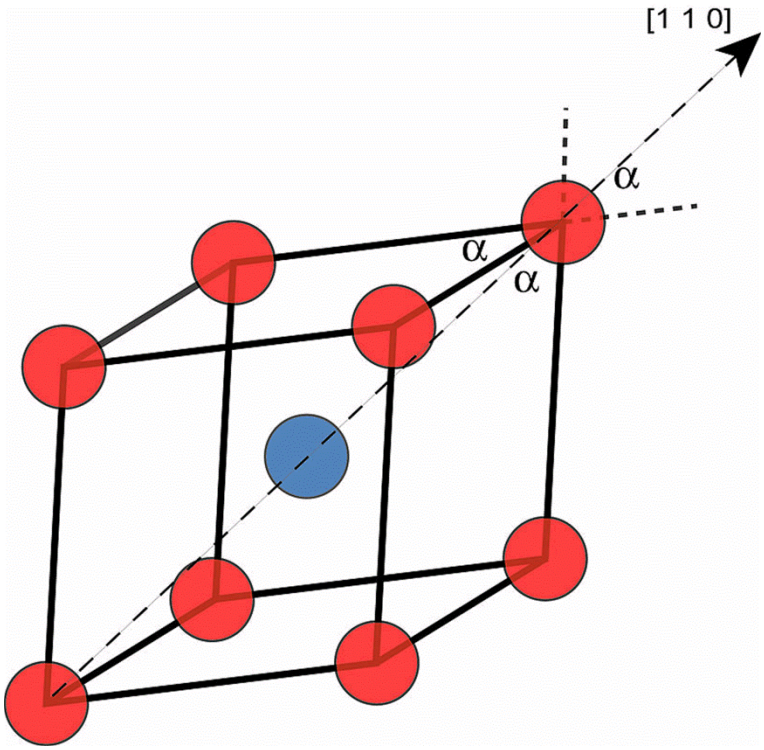

Fig. 2.4 R-phase structure [39]

Its group space is R3 with unit cell structure parameters $a = 0.6704\ nm$ and $\alpha = 113.83°$ [45-47]. Different from the space group of the parent phase (B2 structure), the Ni_4Ti_3 precipitate has only 6 symmetry operations. The orientation relationship between coherent precipitate Ni_4Ti_3 and parent phase is $[010]_{Ni_4Ti_3} \parallel [\bar{2}\bar{1}3]_{NiTi}$ and $(001)_{Ni_4Ti_3} \parallel (111)_{NiTi}$. Therefore, there are 8 possible crystallographic orientations at 4 pairs of Ni_4Ti_3 precipitates in the NiTi matrix [48]. The microstructure of Ni_4Ti_3 is shown in Fig. 2.5 [49].

Ti_2Ni is another set of precipitates that often forms around grain boundaries, weakening the mechanical properties of NiTi alloys [50-52]. Ti_2Ni has a cubic structure with space group

Fd3m. Unit cell parameter is $a = 1.1278\ nm$ [52]. Ti_2Ni can easily react with oxygen, thereby forming a brittle Ti_2NiO_x phase [43]. Ti_2Ni also leads to an increased number of defects in the NiTi matrix [50, 51]. In the alloy with Ti_2Ni precipitates, thermal cycling destabilizes the structure and properties of NiTi alloy [53]. The microstructure of Ti_2Ni is shown in Fig. 2.6 [54].

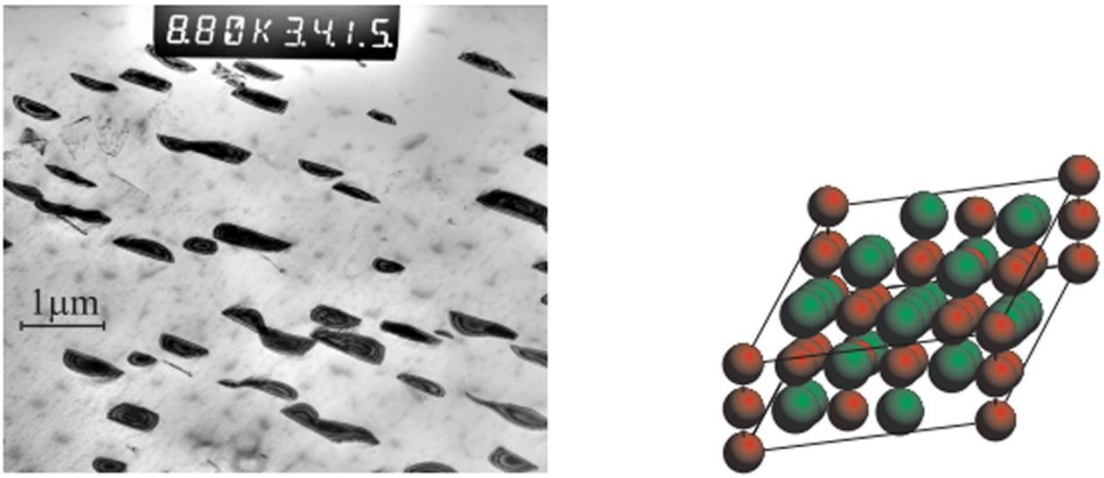

Fig.2.5 Ni_4Ti_3 precipitates (a) a TEM micrograph of NiTi B2 matrix with Ni_3Ti_4 precipitates after stress-free aging at 530 ℃ for 11 hours; (b) the arrangement of atoms in one unit cell of the rhombohedral structure of the Ni_4Ti_3 precipitate. [49]

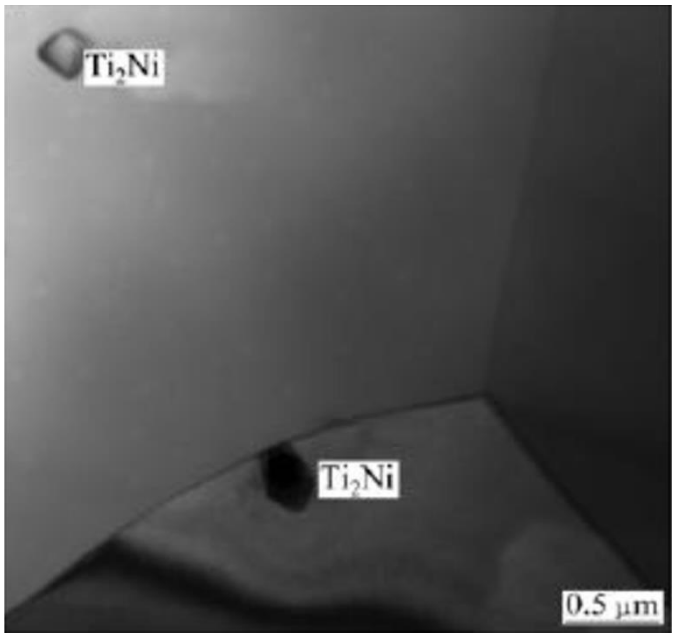

Fig. 2.6 Micrograph of Ti_2Ni precipitates [54]

$TiNi_3$, a hexagonal structure with unit parameter *a = 0.5101 nm, c = 0.83067 nm,* is formed when NiTi is aged at high temperature for an extended period of time. The space group of $TiNi_3$ is $P6_3/mmc$ [55]. $TiNi_3$ precipitates increase mechanical properties, and lead to high strength (1400–2000 MPa) and retention of 10–20% ductility and $TiNi_3$ microstructure (Fig. 2.7) [56].

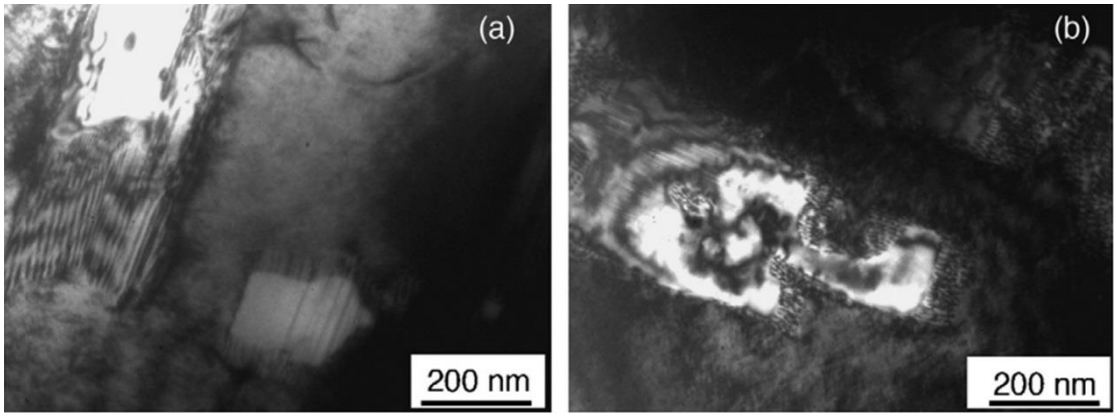

Fig. 2.7 Bright field TEM images of $TiNi_3$ precipitates after aging at 800 ℃ for 0.5h [56]

2.4 Shape Memory Effect and Psedoelasticity

The phase diagram and crystal structure of different phases in the NiTi system were introduced in previous sections. As was discussed above, martensitic phase transformation can be activated by applied stress or thermal cycling, and can lead to the two special properties of SMAs: shape memory effect and pseudoelasticity [13, 49, 57]. Superelasticity, or pseudoelasticity, is a materials property that results from the fully recoverable deformation of austenite during loading and unloading. This phenomenon is related to stress-induced martensitic transformation. The shape memory effect is a materials property that refers to the fully recoverable deformation of martensite upon heating after loading and unloading. The detail of shape memory effect and pseudoelasticity (Fig. 2.8) [15] explains that material

behavior is related to temperatures A_s, A_f, M_s and M_f, which were introduced in Chapter 1.

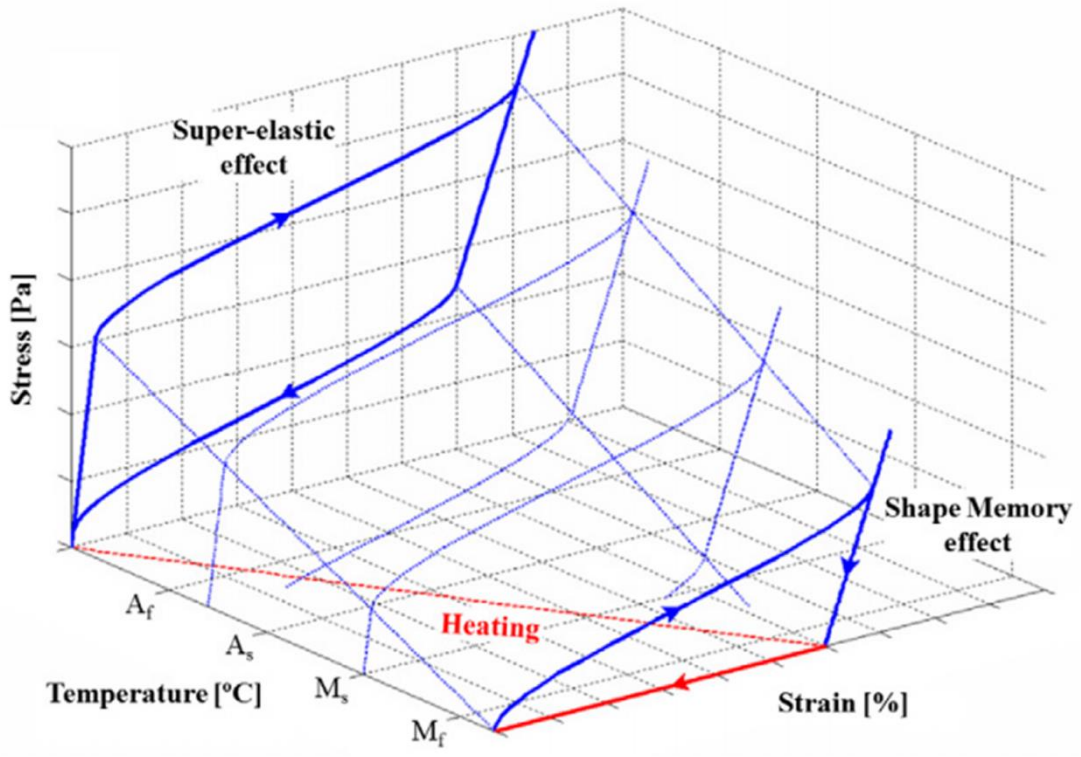

Fig. 2.8 Schematic show of shape memory effect and pseudoelasticity [15]

The SME could be divided into one-way shape memory (OWSM) [58-60], and two-way shape memory (TWSM) [14, 61-64] [51, 65, 66]. The self-accommodation variants of martensite are formed during the cooling of austenitic SMA. These martensitic variants can be reoriented by applied stress and lead to shape deformation. The shape is recovered after the sample reverts to the austenitic phase. No change of shape occurs when the sample is cooled below M_f. This phenomenon is defined as OWSM. If the specimen could be deformed backward and forward during thermal cycling, it would then be called TWSM. In TWSM of SMA, the sample can remember its martensitic shape after trainning. Schematic pictures of OWSM and TWSM are shown in Fig. 2.9 [13].

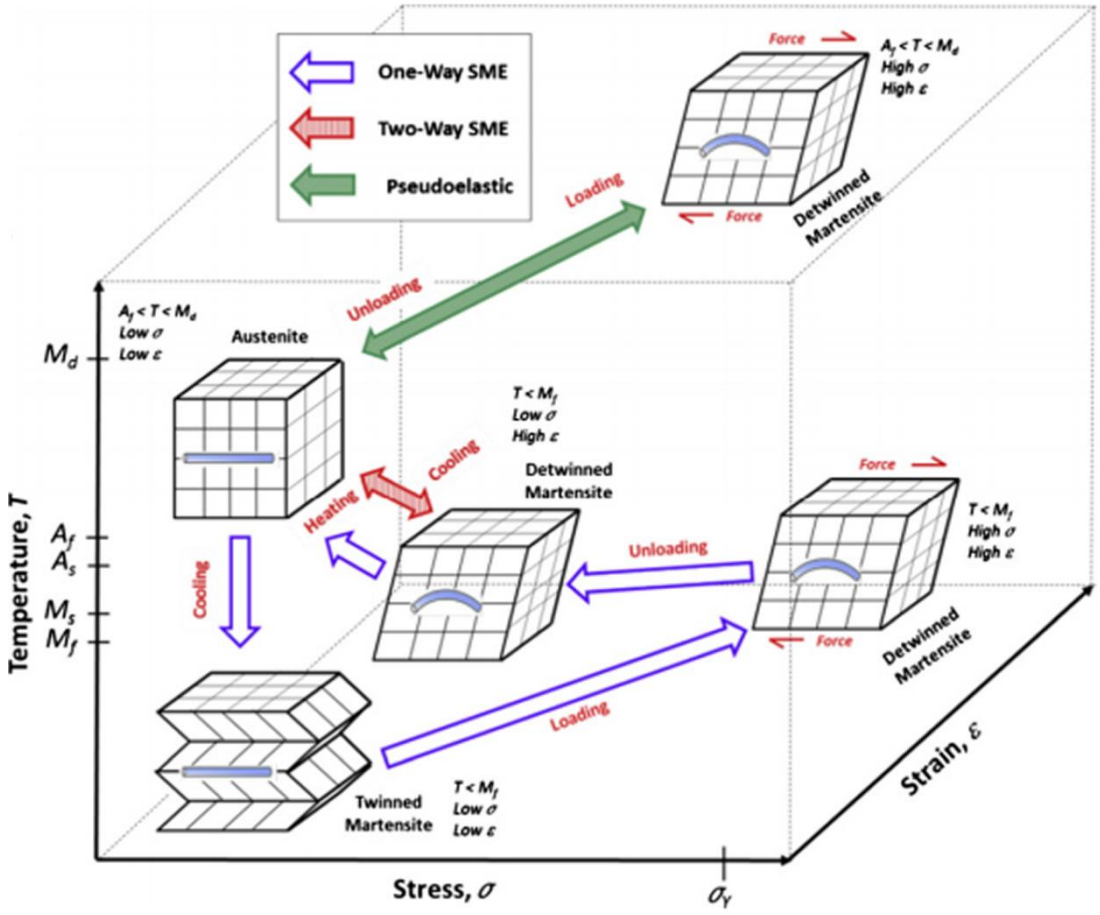

Fig. 2.9 Schematic of one-way SME, two-way SME and pseudoelastic [13]

2.5 Applications of SMAs

Automotive [67, 68], aerospace [20, 69], and biomedical [70-73] applications of SMAs, which were discussed briefly in Chapter 1, will be discussed in detail here. Generally speaking, SME can be used to generate motion, and SE can be used in energy storage applications [13, 14].

2.5.1 Automotive Applications

SMAs have been widely designed as sensors and actuators for their mechanical simplicity and compactness [13]. Compared to traditional electromagnetic actuators, SMA

actuators reduce the scale, weight and cost of automotive components and offer substantial performance [67, 68]. General Motors (GM), a pioneer in SMA automotive applications, has earned 247 patents [13]. Recently, SMA actuators have been used in Chevrolet Corvettes to actuate the hatch vent to release air from the trunk. Their excellent performance at high strain rate deformation has led to SMA design for automatic pedestrian protection systems to minimize pedestrian injuries during impact collision. Details of the application of SMAs for the automotive industry are shown in Fig. 2.10 [13]. Although SMAs have many potential applications in the automotive industry, only a few have actually been implemented due to the limited range of SMA transformation temperatures, lifetime, hysteresis width, and stability. Therefore, further research is needed to overcome the challenges [13].

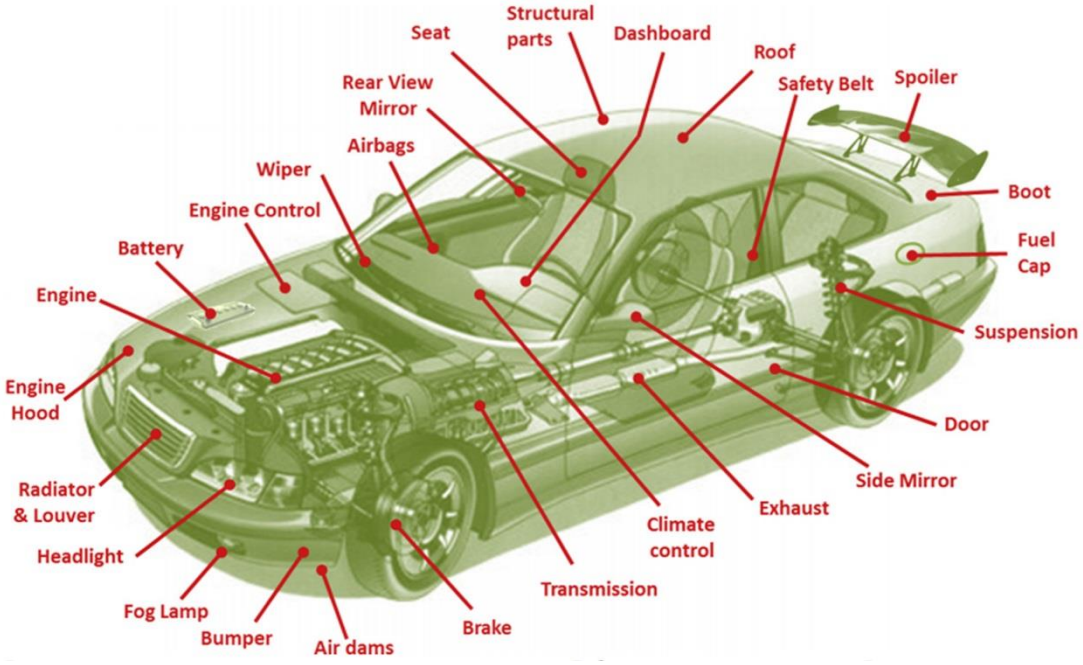

Fig.2.10 Existing and potential SMA applications in the automotive domain [13]

2.5.2 Aerospace Applications

SMAs have been widely used in aerospace as actuators [20, 74], structural connectors,

vibration dampers, sealers, release or deployment mechanisms [13, 75, 76], inflatable structures, manipulators [77], and pathfinders [78]. The most well-known application of SMAs in aerospace engineering is the variable geometry chevron (VGC) developed by Boeing first for GR90-115B jet engines in Boeing 777-300 ER commercial aircraft [79-81]. The VGC is designed to reduce noise during take-off and increase cruise efficiency during the remainder of the flight (Fig. 2.11) [13]. Multi-component applications with SMA forms are subjected to non-homogeneous loading and large deformation. SMAs are selected for their high damping properties [13]. Many other researchers also pursued SMA aerospace engineering applications, working with the Defense Advanced Research Projects Agency (DARPA) for aircraft smart wings [82] and the Smart Aircraft and Marine Propulsion System Demonstration (SAMPSON) program for jet engines [83].

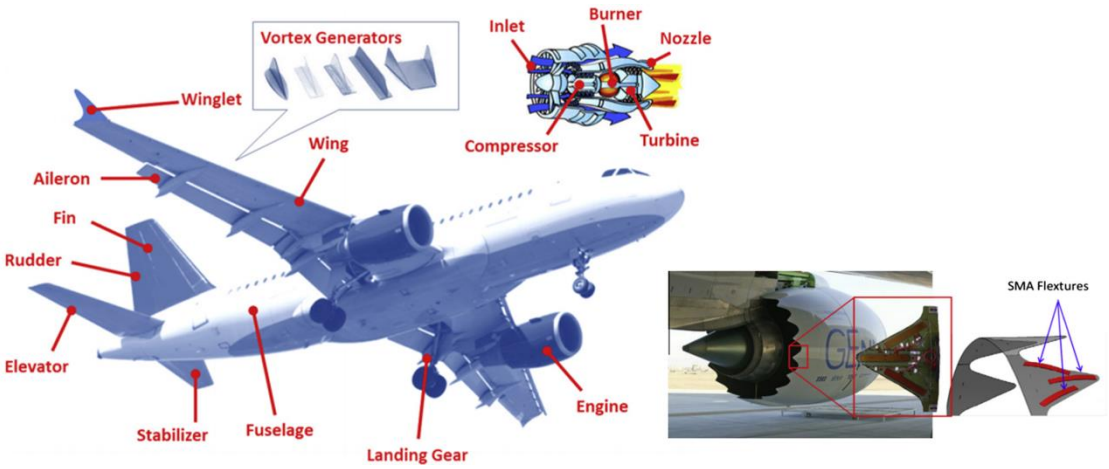

Fig. 2.11 Existing and potential SMA applications in the aerospace domain [13]

2.5.3 Biomedical Applications

NiTi SMA was designed as material for implants since the pseudoelasticity was observed by Buehler et al. in 1962 [8]. NiTi is used widely in biomedical engineering when it

is introduced in minimally invasive surgery (MIS) [84]. After the Mitek surgical product for orthopedic surgery was approved by the U.S. Food and Drug Administration (FDA) in September 1989, SMAs enjoyed a significant breakthrough in the biomedical domain [13]. Due to high corrosion resistance, bio-compatible, and non-magnetic properties, SMAs are designed as endodontics, stents, medical tweezers, sutures, anchors, implants, eyeglass frames and guide wires [70-73] (Fig. 2.12 [13]).

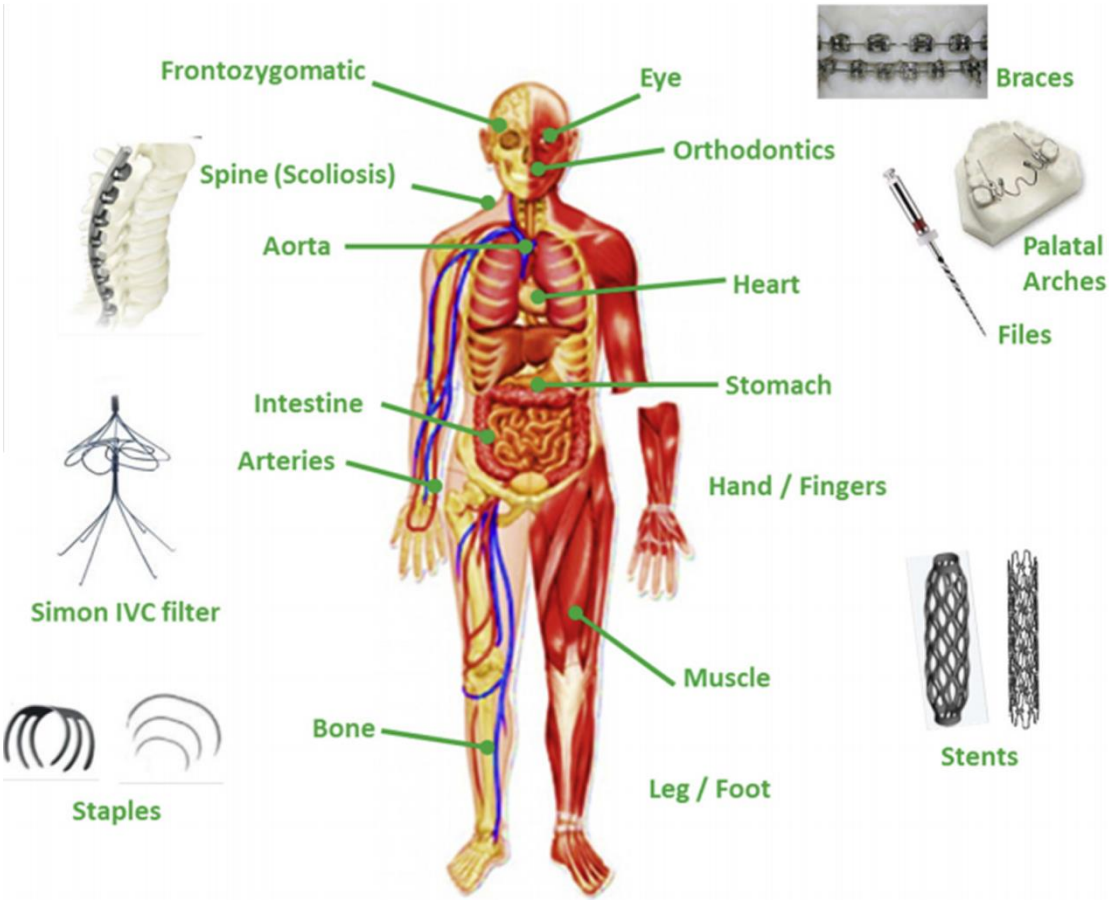

Fig.2.12 Existing and potential SMA applications in the biomedical domain [13]

2.6 Classical Models for Martensitic Phase Transformation

Martensitic transformation was discovered for the first time in the microstructure of steels after quenching. Typical features of martensitic transformation are that the

transformation is diffusionless and driven by shear stress or strain. Martensitic phase transformation is activated in typical planes and along typical directions. The crystal orientation of the martensitic phase with respect to the interface with the austenitic phase is called “habit plane.” Martensitic transformation is important to SMAs; the classical models for martensitic transformation are discussed in this section.

Early theories for the thermodynamics and kinetics of martensitic transformation are attributed to Kaufman and Cohen [85-87]. The Gibbs free energy of martensitic and austenitic phase is written as:

$$G_{M/A} = H_{M/A} - TS_{M/A} \tag{2.1}$$

where G, H and S are Gibbs free energy, enthalpy and entropy. The footnote M and A represents martensite and austenite, respectively. The martensitic and austenitic phase has the same energy at temperature T_0. As shown in Fig. 2.13, overcooling is needed to activate phase transformation. The energy generated by overcooling overcomes the transformation barrier by the energy from interface distortion and strain energy.

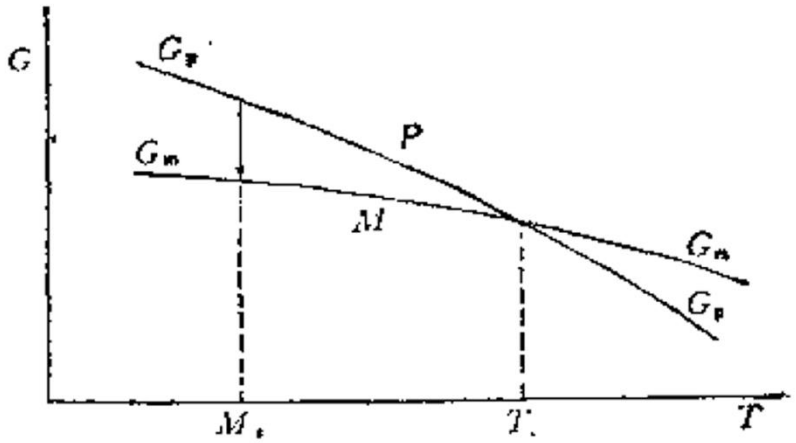

Fig. 2.13 Gibbs free energy of parent and martensitic phase [86]

The nucleation of martensite is assumed by Kaufman and Cohen and is shown in Fig.

2.14. Energy change during the nucleation of martensite is written as:

$$\Delta G = \frac{4}{3}\pi r^2 c\Delta g + \frac{4}{3}\pi r^2 c\left(\frac{Ac}{r}\right) + 2\pi r^2\sigma \tag{2.2}$$

where $A \approx \mu(\gamma^2 + \varepsilon_n^2)$, r and c are the radius and thickness of the nucleation, respectivley. Δg is the difference between the free energy of the two phases. σ is the interface energy per unit area. γ and μ are shear strain and shear modulus, respectively. ε_n is body strain.

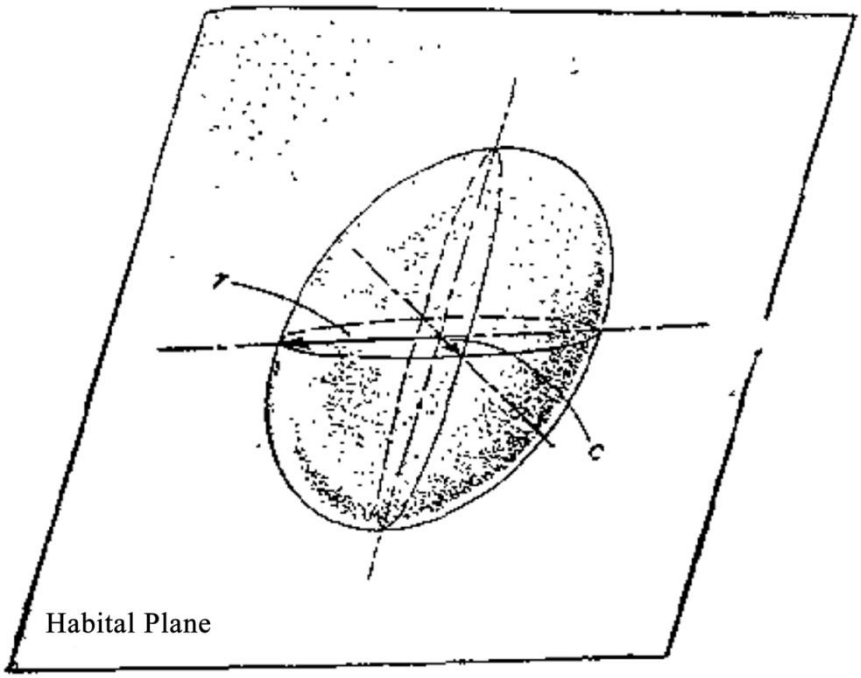

Fig. 2.14 Nucleation of martensitic phase in austenitic phase [85]

According to the assumption above, the transformation barrier is

$$\Delta G^* = \frac{32}{3}\pi\left(\frac{A^2\sigma^2}{\Delta g^4}\right) \tag{2.3}$$

Olson and Cohen [88] calculated the energy barrier for Fe-30%Ni with M_s = 233K. Overcooling is assumed to be 200K and Δg = -1318.8 J/mol. The energy barrier ΔG^* is calculated as 5.4×10^8 J/mol, which is an extremely high value.

Olson and Cohen [89-91] improved the model by considering dislocation. Thus, the energy barrier decreases, and the martensite is assumed to be nucleated at the stacking fault of the parent phase. They took into consideration the transformation from face center cubic

(FCC) to body center cubic (BCC) structure. The close-packed plane of FCC structure is (1 1 1) plane, which is shown in Fig. 2.15. The atoms in the (1 1 1) plane of the FCC structure have the same arrangement as those in the (1 1 0) plane of the BCC structure. Therefore, martensitic transformation can be seen as the shear of atoms in the (1 1 1) plane in the FCC phase to the (1 1 0) plane in the BCC phase (Fig. 2.16). The shear vector is $\frac{1}{18}[1\ 2\ 1]$. According to the model, another shear vector $\frac{1}{8}[1\ 1\ 0]$ is needed to relocate the atoms in the (1 1 0) plane to form the BCC structure (Fig. 2.17). Normal dislocation in the FCC structure is $\frac{1}{2}[1\ 1\ 0]$. The first shear vector $\frac{1}{18}[1\ 2\ 1]$ can be seen as the decomposing of $\frac{1}{2}[1\ 1\ 0]$ dislocation as:

$$\frac{1}{2}[1\ 1\ 0] \rightarrow \frac{1}{6}[1\ 2\ 1] + \frac{1}{6}[2\ 1\ \bar{1}] \tag{2.4}$$

The second step of the shear needs the decomposing of dislocations in the BCC phase. Normal dislocation in the BCC structure is $\frac{1}{2}[1\ 1\ 1]$, and we have

$$\frac{1}{2}[1\ 1\ 0] \rightarrow \frac{1}{8}[1\ 1\ 0] + \frac{1}{4}[1\ 1\ 2] + \frac{1}{8}[1\ 1\ \bar{4}] \tag{2.5}$$

Therefore, martensitic phase transformation is activated by the two steps of shear through the decomposing of dislocations.

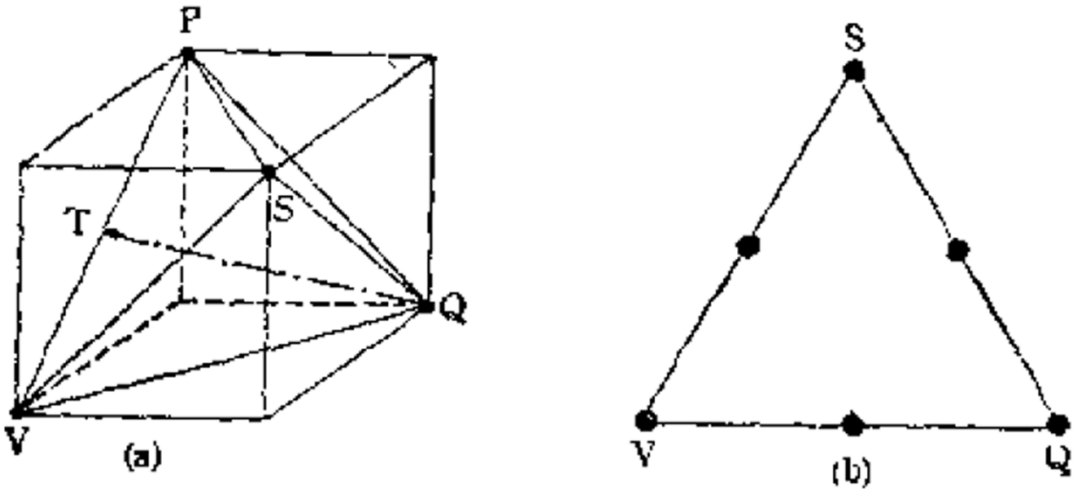

Fig. 2.15 Schematic of (a) BCC structure (b) close packed plane of BCC structure [89]

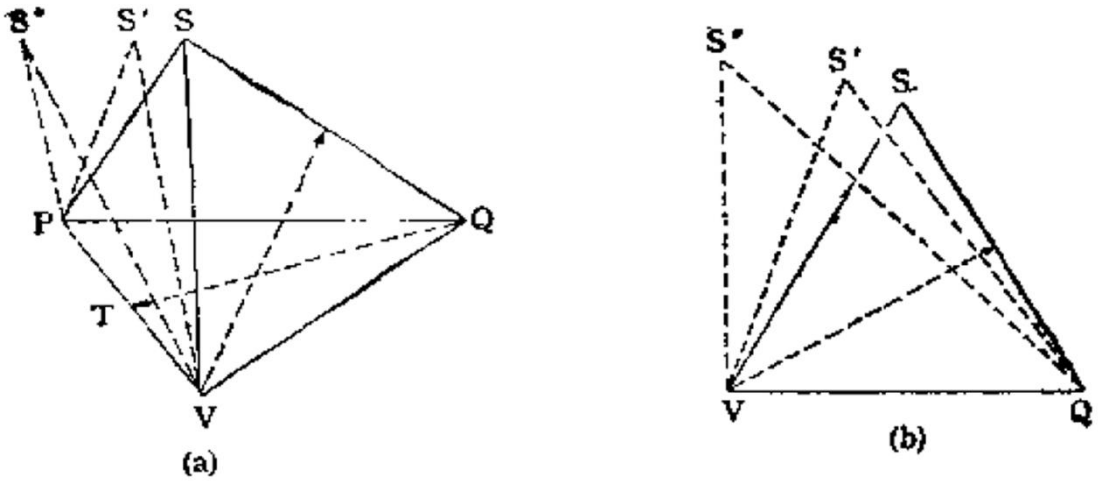

Fig. 2.16 Schematic of the shear from BCC to FCC [89]

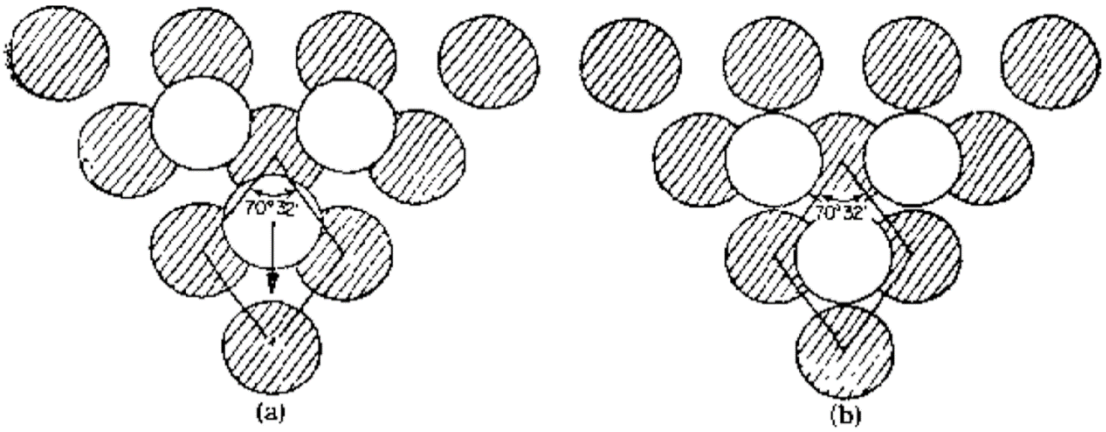

Fig. 2.17 Schematic of relocation of atoms on (110) plane [89]

The classical theories discussed above considered only the orientation difference between the parent and martensitic phases. The habital relationship is not correctly given through these models. Therefore, phenomenological models were established with the consideration of habital planes and habital directions during phase transformation. The two typical early models include B-M model, which was established by Bowles and Mackenzie [92-94]; and W-L-R model, which was established by Wechsler, Lieberman and Read [95, 96]. In these phenomenological models [92-96], matrix algorithms are applied to calculate the relationship between austenitic and martensitic phases. Transformation from parent phase (FCC) to martensitic phase (BCC) in Jaswon and Wheeler's research [97] follows the *K-S*

(named after Kurdjamov and Sachs) relationship [98], which is $(111)_f \parallel (101)_b$ and $(1\bar{1}0)_f \parallel (11\bar{1})_b$. Therefore, the three independent coordinate axes of *I* which are I_x, I_y and I_z are:

$$\begin{cases} [111]_f \parallel [101]_b \\ [1\bar{1}0]_f \parallel [11\bar{1}]_b \\ [1\bar{1}0]_f \times [111]_f \parallel [11\bar{1}]_b \times [101]_b \; or \; [\bar{1}\bar{1}2]_f \parallel [1\bar{2}\bar{1}]_b \end{cases} \tag{2.6}$$

Transformation from FCC to BCC can be written in the matrix ***F/B*** and the relationship between coordinate systems in ***F***, ***B***, and ***I*** is that

$$\boldsymbol{(F/B) = (F/I)(I/B)} \tag{2.7}$$

The coordinate systems in ***F*** is $I_x = \frac{1}{\sqrt{3}}[111]_f$, $I_y = \frac{1}{\sqrt{2}}[1\bar{1}0]_f$ and $I_z = \frac{1}{\sqrt{6}}[\bar{1}\bar{1}2]_f$. We assume that

$$(\boldsymbol{F/I}) = \begin{bmatrix} a_1 & b_1 & c_1 \\ a_2 & b_2 & c_2 \\ a_3 & b_3 & c_3 \end{bmatrix} \tag{2.8}$$

Therefore, we have

$$\begin{cases} \frac{1}{\sqrt{6}}\begin{bmatrix} -1 \\ -1 \\ 2 \end{bmatrix}_f = (\boldsymbol{F/I})\begin{bmatrix} 1 \\ 0 \\ 0 \end{bmatrix}_I = \begin{bmatrix} a_1 & b_1 & c_1 \\ a_2 & b_2 & c_2 \\ a_3 & b_3 & c_3 \end{bmatrix}\begin{bmatrix} 1 \\ 0 \\ 0 \end{bmatrix}_I = \begin{bmatrix} a_1 \\ a_2 \\ a_3 \end{bmatrix}_I \\ \frac{1}{\sqrt{2}}\begin{bmatrix} 1 \\ -1 \\ 0 \end{bmatrix}_f = (\boldsymbol{F/I})\begin{bmatrix} 0 \\ 1 \\ 0 \end{bmatrix}_I = \begin{bmatrix} a_1 & b_1 & c_1 \\ a_2 & b_2 & c_2 \\ a_3 & b_3 & c_3 \end{bmatrix}\begin{bmatrix} 0 \\ 1 \\ 0 \end{bmatrix}_I = \begin{bmatrix} b_1 \\ b_2 \\ b_3 \end{bmatrix}_I \\ \frac{1}{\sqrt{3}}\begin{bmatrix} 1 \\ 1 \\ 1 \end{bmatrix}_f = (\boldsymbol{F/I})\begin{bmatrix} 0 \\ 0 \\ 1 \end{bmatrix}_I = \begin{bmatrix} a_1 & b_1 & c_1 \\ a_2 & b_2 & c_2 \\ a_3 & b_3 & c_3 \end{bmatrix}\begin{bmatrix} 0 \\ 0 \\ 1 \end{bmatrix}_I = \begin{bmatrix} c_1 \\ c_2 \\ c_3 \end{bmatrix}_I \end{cases} \tag{2.9}$$

The transformation matrix ***F/I*** is then solved as

$$(\boldsymbol{F/I}) = \frac{1}{\sqrt{6}}\begin{bmatrix} -1 & \sqrt{3} & \sqrt{2} \\ -1 & -\sqrt{3} & \sqrt{2} \\ 2 & 0 & \sqrt{2} \end{bmatrix} \tag{2.10}$$

Similarly, the matrix ***B/I*** is solved as:

$$(\boldsymbol{B/I}) = \frac{1}{\sqrt{6}}\begin{bmatrix} 1 & \sqrt{2} & \sqrt{3} \\ -2 & \sqrt{2} & 0 \\ -1 & -\sqrt{2} & \sqrt{3} \end{bmatrix} \tag{2.11}$$

Therefore, the transformation from FCC to BCC can be represented by the matrix:

$$(\boldsymbol{B/F}) = \frac{1}{6}\begin{bmatrix} -1+2\sqrt{6} & -1 & 2+\sqrt{6} \\ 2+\sqrt{6} & 2+\sqrt{6} & -4 \\ 1 & 1+2\sqrt{6} & -2+\sqrt{6} \end{bmatrix} \tag{2.12}$$

When considering lattice parameters such as the lattice parameter of austenite is a and martensite is α and c, respectively, the transformation matrix is

$$\begin{bmatrix} x\alpha \\ y\alpha \\ zc \end{bmatrix}_b = (\boldsymbol{B/F}) \begin{bmatrix} xa \\ ya \\ za \end{bmatrix}_f \tag{2.13}$$

In 1924, Bain devised a simple way for the transformation from FCC to BCT (Fig. 2.18) [99]. The martensitic phase with a BCC structure is assumed to be generated from the FCC austenitic phase by simple compression. Therefore, Bain transformation from FCC to BCT is represented by matrix **B** as

$$\mathbf{B} = \begin{bmatrix} \eta_1 & 0 & 0 \\ 0 & \eta_1 & 0 \\ 0 & 0 & \eta_2 \end{bmatrix} = \begin{bmatrix} \sqrt{2}a/a_0 & 0 & 0 \\ 0 & \sqrt{2}a/a_0 & 0 \\ 0 & 0 & c/a_0 \end{bmatrix} \tag{2.14}$$

According to the Bain shear, minimum displacement is needed for atoms to move to the new position. Therefore, Bain's model provides a simple and reasonable assumption for martensitic transformation from FCC to BCC structure. Wechsler, Lieberman and Read [95, 96] extended Bain's model to general martensitic transformation with the consideration of twinning structure of martensite. The model is then concluded as W-L-R model [95, 96], and the relationship is written as:

$$\boldsymbol{P_I = R\bar{P}B} \tag{2.15}$$

where $\boldsymbol{P_I}$ is deformation in the invariant plane, $\boldsymbol{R}$ is rotation of the matrix, $\boldsymbol{B}$ is Bain deformation discussed above, and $\boldsymbol{\bar{P}}$ is shear by twinning, slip of dislocation and stacking fault. Bowles and Mackenzie [92-94] established a model similar to W-L-R model, and is

given as:

$$\boldsymbol{P_1 P_2 = RB} \tag{2.16}$$

where $\boldsymbol{P_1}$ and $\boldsymbol{P_2}$ are deformation in invariant planes. The other terms have the same definition as that in the W-L-R model. The W-L-R model has been applied to predict martensitic transformation from the B2 structure to the 9R structure in CuZnAl SMAs [100].

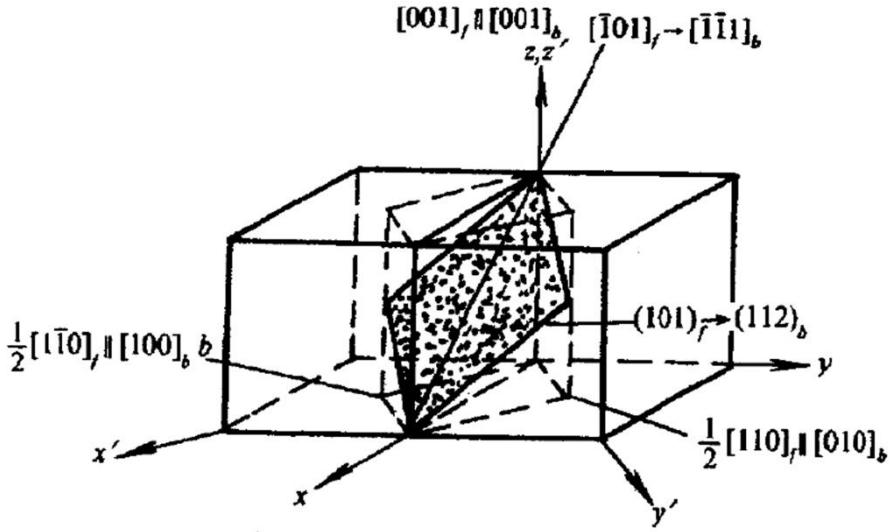

Fig.2.18 Transformation from FCC to BCT by Bain shear [99]

According to the W-L-R model, the habital plane is the plane without deformation and rotation. Therefore, the vector $\boldsymbol{z}$ in the habital plane has the same length before and after phase transformation.

$$\boldsymbol{z^T P^T B^T B P z = z^T z} \tag{2.17}$$

Equation (2.17) can by simplified with the assumption $\boldsymbol{BP = D}$. Therefore, the W-L-R model and equation (2.17) can be rewritten as:

$$\boldsymbol{P_I = RD} \tag{2.18}$$

$$\boldsymbol{z^T D^T D z = z^T z} \tag{2.19}$$

In these equations, the matrix $\boldsymbol{D}$ can be decomposed to an orthogonal matrix $\boldsymbol{R_f}$ and a symmetric matrix $\boldsymbol{D_s}$ and therefore

$$\boldsymbol{D} = \boldsymbol{R_f D_s} \tag{2.20}$$

The symmetric matrix $\boldsymbol{D_s}$ can be diagonalized by unitary congruence

$$\boldsymbol{D_s} = \boldsymbol{R_d D_d R_d^T} \tag{2.21}$$

with $\boldsymbol{R_d^T} = \boldsymbol{R_d^{-1}}$ and the diagonal matrix $\boldsymbol{D_d}$ having the form as

$$\boldsymbol{D_d} = \begin{bmatrix} \lambda_1 & 0 & 0 \\ 0 & \lambda_2 & 0 \\ 0 & 0 & \lambda_3 \end{bmatrix} \tag{2.22}$$

We also have the relationship as

$$\boldsymbol{z} = \boldsymbol{R_d z_d} \tag{2.23}$$

Therefore, the relationship in (2.19) can be rewritten as

$$\boldsymbol{z_d^T}(\boldsymbol{D^T D} - \boldsymbol{\lambda^2 I})\boldsymbol{z_d} = \boldsymbol{0} \tag{2.24}$$

where $\boldsymbol{I}$ is the unit matrix and $\boldsymbol{\lambda}$ is the eigenvalue. From (2.24) we have

$$\mathrm{Det}(\boldsymbol{D^T D} - \boldsymbol{\lambda^2 I}) = \boldsymbol{0} \tag{2.25}$$

The equations can be solved easily on the orthogonal basis. Therefore, three vectors in the invariant plane are taken to build the new orthogonal basis; the three vectors are the unit shear vector $d = (d_1, d_2, d_3)$, the normal vector of the plane $f = (f_1, f_2, f_3)$ and the vector $t = d \otimes f = (t_1, t_2, t_3)$. The vectors in the parent lattice can be related to that in the orthogonal basis through the matrix:

$$\boldsymbol{R(c/o)} = \begin{bmatrix} d_1 & f_1 & t_1 \\ d_2 & f_2 & t_2 \\ d_3 & f_3 & t_3 \end{bmatrix} \tag{2.26}$$

The shear matrix in the orthogonal basis is

$$\boldsymbol{P_o} = \begin{bmatrix} 1 & g & 0 \\ 0 & 1 & 0 \\ 0 & 0 & 1 \end{bmatrix} \tag{2.27}$$

where g is the value of shear deformation. The Bain matrix and $\boldsymbol{D^T D}$ in the orthogonal basis can be rewritten as:

$$\boldsymbol{B_o = R^T(c/o)B_cR(c/o)} \tag{2.28}$$

$$\boldsymbol{(D^TD)_o = P_o^TB_o^TB_oP_o} \tag{2.29}$$

Therefore, equation (2.25) can be rewritten as:

$$(\lambda^2)^3 - T(\lambda^2)^2 + Q\lambda^2 - H = 0 \tag{2.30}$$

where $H = Det[(\boldsymbol{D^TD})_o]$, $T = Tr[(\boldsymbol{D^TD})_o]$, $Q = \sum_{ij}^{3}\left(J_{jj}J_{ii} - J_{ij}^2\right)$ and J_{ij} is the element in the matrix $\boldsymbol{J = (D^TD)_o}$.

During phase transformation from *B2* to *9R*, we have the parameter of *B2* structure a_0 = 0.29348 nm and the parameters of *9R* structure a = 0.44465 nm, b = 0.26617 nm, c = 1.91925 nm, β = 89.21°. Therefore, shear g is solved as 0.194080; the eigenvalues are $\lambda_1^2 = 1$, $\lambda_2^2 = 1.136325$, $\lambda_3^2 = 0.867839$; the habital plane is $(\bar{1},\ 7.71151,\ 9.323679)$ and the normal direction of the habital plane is $(-0.082367,\ 0.635174,\ 0.767965)$. The transformation matrix $\boldsymbol{P_I}$

$$\boldsymbol{P_I} = \begin{bmatrix} 1.065402 & -0.008865 & -0.004891 \\ 0.008887 & 0.995086 & -0.086275 \\ 0.021132 & 0.097811 & 0.928036 \end{bmatrix} \tag{2.31}$$

The calculated value of the habital plane matches well with the experimental value, which is $(\bar{1},\ 6.88,\ 7.90)$.

2.7 Martensitic Phase Transformation Models for SMAs

Constitutive models for SMAs have been developed in the last decades since early 1990s. Generally speaking, the models can be divided into three groups: microscopic thermodynamic, micro-macro, and macroscopic. Microscopic models are established on SMA microstructures such as phase boundary, grain boundary, and twinning, to name a few. Compared to the microscopic models, micro-macro models focus on the properties at meso

scales. To save time for computer calculation, macroscopic models are established based on experimental data. Microstructural evolution is not included in macroscopic models. The three groups of models are discussed in detail in the following sections.

2.7.1 Microscopic Thermodynamic Models

Microscopic models focus on SMA microstructural features such as phase nucleation, martensite twin and so on. System energy and stress strain curves are modeled by Ginzburg-Landau theory or molecular dynamics. The earliest models for SMAs using Landau theory were developed by Falk [101] and later extended by Ball and James [102], Levitas et al. [103], Wang et al. [104], Cho et al. [105], and Zhong and Zhu [106]. Energy distribution is related to temperature and strain. Equilibrium status is obtained in the energy minima. Molecular dynamics are applied to model phase transformation, mechanical properties, and the microstructural evolution of SMAs. System energy is established in atomic scales. The potential energy among Ni-Ti, Ni-Ni, Ti-Ti atoms is written as Φij. The energy of embedding an atom into the system is Fi, which is related to the electron density ρij of the atomic system. Lennard-Jones (LJ) [107] or embedded-atom-method (EAM) [108] potentials are the two main potentials for atomic energy. Uehara et al. [109] successfully model the phase transformation behavior of SMAs composed of 31,000 atoms with EAM potential. Chowdhury et al. [110] used the molecular dynamics method to model the influence of Ni_4Ti_3 precipitates on transformation. The following section discusses in detail microscopic models based on molecular dynamics.

In molecular dynamics models, Netwon's equations are applied to describe the motion

of atoms. The motion of *i*th atom is related to energy potential by [111]:

$$m_i\ddot{r}_i = -\partial\phi/\partial r_i \tag{2.32}$$

where m_i is the mass of the atom, r_i is the position vector of the atom, and ϕ is the potential energy of interaction between atoms. The temperature of the system is [111]:

$$T = \frac{2E_K}{3NK_b} \tag{2.33}$$

where K_b is the Boltzmann constant, E_K is the total kinetic energy and *N* is the number of atoms in the system. Internal stress σ^{int} is related to virial stress σ^{vir}, which equals Cauchy stress in continuum mechanics as [112]:

$$\boldsymbol{\sigma^{vir}}(\boldsymbol{r}) = \frac{1}{J}\boldsymbol{h}\sigma^{int}\boldsymbol{h^T} = \frac{1}{\Omega}\sum_i\left[-m_i\boldsymbol{v_i}\otimes\boldsymbol{v_i} + \sum_{i\neq j}\frac{\partial\phi(r_{ij})}{\partial r_{ij}}\frac{\boldsymbol{r_{ij}}\otimes\boldsymbol{r_{ij}}}{r_{ij}}\right] \tag{2.34}$$

where $\boldsymbol{h}$ is the cell tensor, J is the volume change, Ω is the current cell volume, $\boldsymbol{v_i}$ is the velocity vector of the *i*th atom, and $\boldsymbol{r_{ij}}$ is the relative position vector of atom *j* with respect to atom *i*. The strain between any two atoms *i* and *j* is given by [113]:

$$\varepsilon_{ij}^{\alpha\beta} = \frac{1}{2}\left(\frac{\partial u_{ij}^{\alpha}}{\partial r_{ij}^{\beta}(0)} + \frac{\partial u_{ij}^{\beta}}{\partial r_{ij}^{\alpha}(0)}\right) \approx \frac{1}{2[r_{ij}(0)]^2}\left(u_{ij}^{\alpha}r_{ij}^{\beta}(0) + u_{ij}^{\beta}r_{ij}^{\alpha}(0)\right) \tag{2.35}$$

Therefore, the strain of atom *i* interacts with *N* others and can be written as:

$$\varepsilon_i^{\alpha\beta} = \frac{1}{N}\sum_{j=1}^{N}\varepsilon_{ij}^{\alpha\beta} \tag{2.36}$$

In microscopic models, the choice of potential is important; and the two popular energy potentials for molecular dynamic models are Lennard-Jones (LJ) [107] and embedded-atom-method (EAM) [108]. Uehara et al. [109] used EAM potential function for molecular dynamic models for NiAl SMAs. The potential is expressed as

$$\phi = \sum_i F(\rho_i) + \frac{1}{2}\sum_i\sum_{i\neq j}\phi_{ij}(r_{ij}) \tag{2.37}$$

where electron density ρ_i can be written as

$$\rho_i = \sum_{i\neq j}\tilde{\rho}(r_{ij}) = \sum_{i\neq j}\{N^s\tilde{\rho}^s(r_{ij}) + N^d\tilde{\rho}^d(r_{ij})\} \tag{2.38}$$

where

$$\tilde{\rho}^s(r_{ij}) = \tilde{\rho}^d(r_{ij}) = |\sum_I C_I R_I|^2/4\pi \quad (2.39)$$

$$R_I = \frac{(2\zeta_I)^{n_I+1/2}}{[(2n_I)!]^{1/2}} r_{ij}^{n_I-1} exp(-\zeta_I r_{ij}) \quad (2.40)$$

Here, N^s, N^d, C_I, ζ_I, n_I are parameters depending on the species of the atom. The embedding function *F* is given as:

$$F(\rho) = k_1\rho^{1/2} + k_2\rho + k_3\rho^2 \quad (2.41)$$

where k_1, k_2, and k_3 are parameters for Ni and Al. The potential energy for a two-body term as the distance between two atoms is given as:

$$\phi_{ij}(r_{ij}) = Z_i(r_{ij})Z_j(r_{ij})/r_{ij} \quad (2.42)$$

$$Z(r_{ij}) = Z_0(1 + \beta r_{ij}^{\upsilon})exp(-\alpha r_{ij}) \quad (2.43)$$

Here Z_0, β, υ, and α are parameters for Ni and Al.

The author considers two configurations of grain structures (Fig. 2.19). Model A is composed of two square and two octagonal grains, while model B consists of four hexagonal grains. Crystal orientation in a grain is varied for each grain by rotation around the z-axis by an angle θ. Crystal orientations in grains G1-G4 are $\theta_1 - \theta_4$. Crystal orientations ($\theta_1 - \theta_4$) of model A are 0 °, 63.4 °, 11.3 °, and 33.7 °. Crystal orientations of model B are 18.4 °, 11.3 °, 33.7 °, and 14.0 °. Crystal orientations of model B1-B6 are shown in Table 2.2. Figures 2.20 and 2.21 show variations in atomic configuration throughout loading, unloading, heating and cooling, depicted with the local structure for model A and B, respectively. Figure 2.22 represents stress–strain curves during loading for models B1–B6 and model A, in which the initial bias due to relaxation is offset by the origin.

Table 2.2 Crystal orientations for simulations of B1-B6 in units of degrees				
Model	θ_1	θ_2	θ_3	θ_4
B1	18.4	11.3	26.6	33.7
B2	-18.4	11.3	26.6	-33.7
B3	63.4	56.3	71.6	78.7
B4	-63.4	56.3	71.6	-78.7
B5	63.4	11.3	18.4	78.7
B6	-63.4	11.3	18.4	-78.7

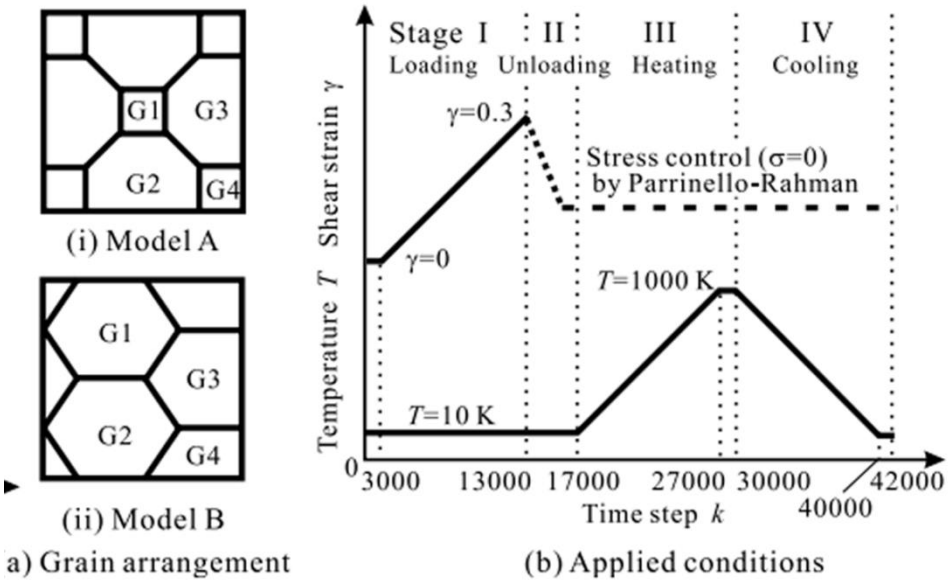

Fig. 2.19 Illustration of grain arrangement (a) and the applied profile of mechanical and thermal conditions (b) [109]

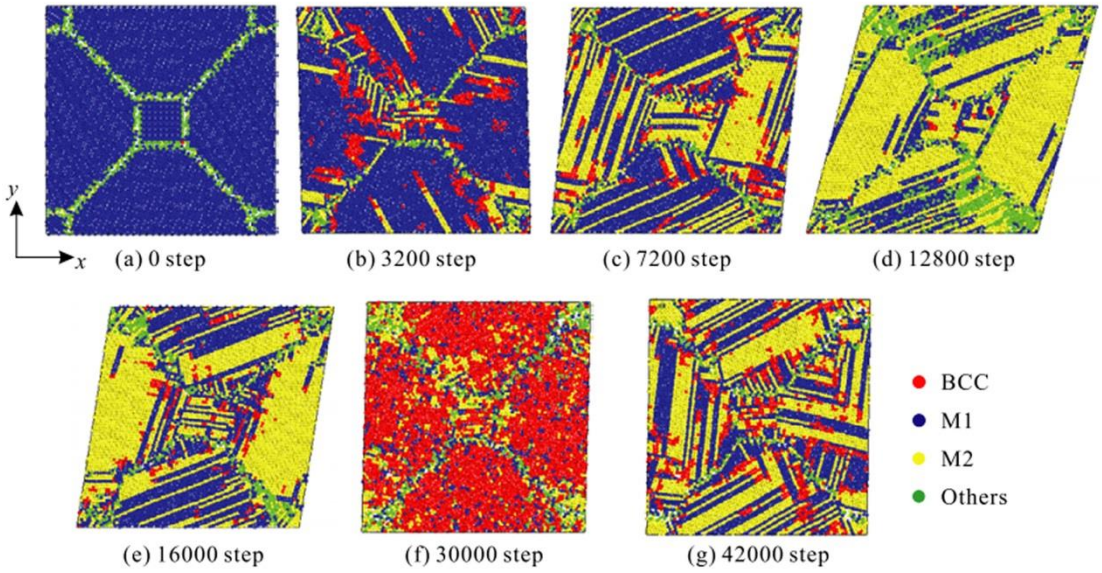

Fig. 2.20 Configuration of atoms during loading, unloading, heating and cooling for model A: (a) initial state, (b) after relaxation, (c) during loading, (d) after loading, (e) after unloading, (f) after heating and (g) after cooling [109]

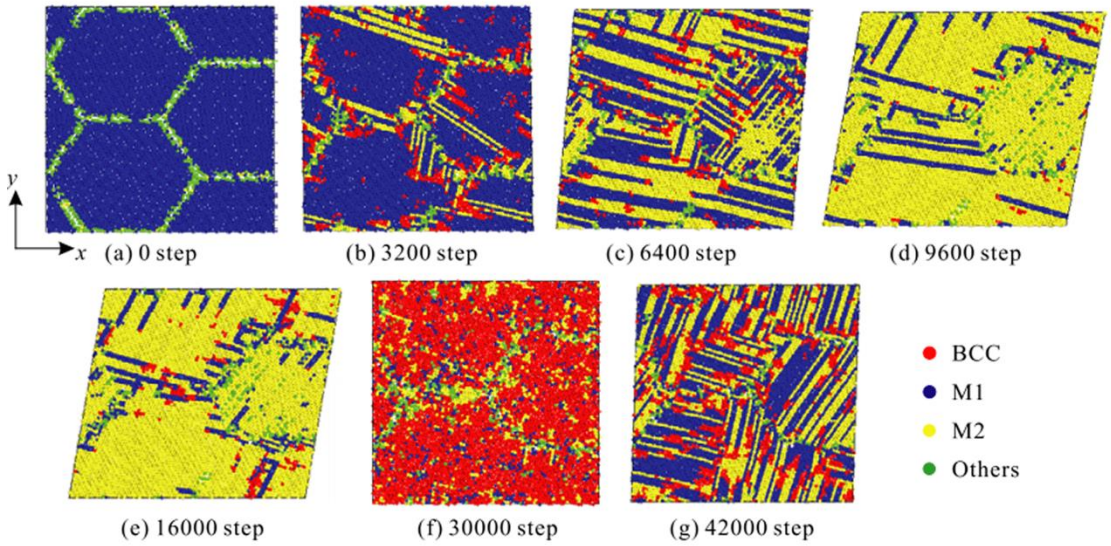

Fig. 2.21 Configuration of atoms during loading, unloading, heating and cooling for model B: (a) initial state, (b) after relaxation, (c) during loading, (d) after loading, (e) after unloading, (f) after heating and (g) after cooling [109]

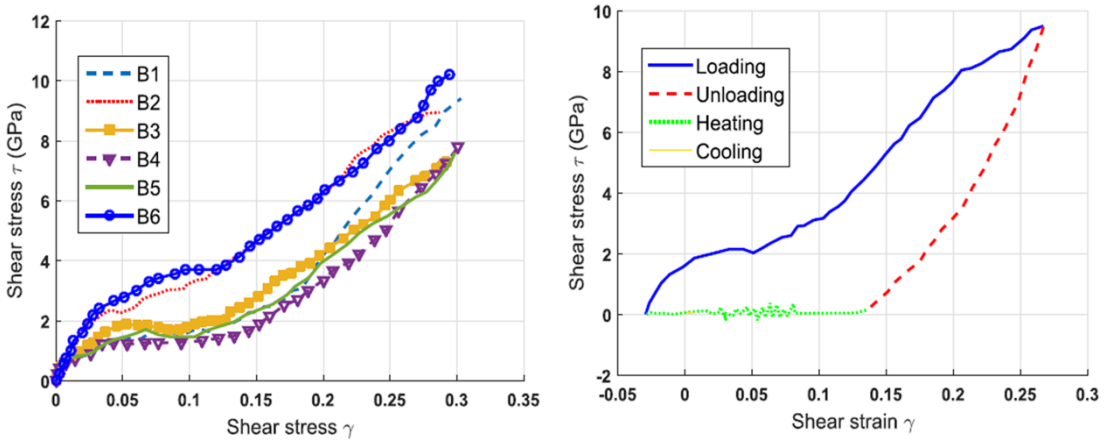

Fig. 2.22 (a) Stress–strain curves during loading for variously oriented models, B1–B6 (b) Stress–strain relation during loading, unloading, heating and cooling for model A [109]

2.7.2 Micro-macro Models

Compared to microscopic models, micro-macro models focus on the properties at meso scales. Mechanical properties on transformation systems are established. The macroscopic behaviors of SMAs are obtained from the vector sum of the behaviors of single grains by Mori-Tanaka scheme [114], or Sach and Taylor approaches [115]. The transformation strain

of each transformation system is assumed to be related to the transformation plane normal vector and direction vector. Total transformation strain is volume product of the transformation strain of each martensitic variant. Traction continuity is often applied to solve system stress strain. Stupkiewicz and Gorzynska-Lengiewicz [116] studied forward transformation of SMAs with 528 transformation systems. Anand and Gurtin [117] compare the difference between 192 and 24 transformation systems, and a similar stress strain curve is noticed in their research. The reorientation of martensite is studied by Yu et al. [118-120] Similar work can be found in Thamburaja et al. [121, 122], and Ostwald [123].

The following section discusses in detail micro-macro models using the model of Yu et al. [120]. When dealing with small deformation in single crystal NiTi SMAs, total strain tensor $\boldsymbol{\varepsilon}$ is composed of three parts; i.e., elastic strain tensor $\boldsymbol{\varepsilon^e}$, strain tensor $\boldsymbol{\varepsilon^m}$ caused by thermo-elastic martensitic transformation; reorientation and detwinning of twinned martensite; and plastic strain tensor $\boldsymbol{\varepsilon^p}$. The relationship is written as:

$$\boldsymbol{\varepsilon} = \boldsymbol{\varepsilon^e} + \boldsymbol{\varepsilon^m} + \boldsymbol{\varepsilon^p} \tag{2.44}$$

Strain tensor $\boldsymbol{\varepsilon^m}$ can be decomposed into three parts; i.e., martensite transformation strain $\boldsymbol{\varepsilon^{tr}}$, reorientation strain $\boldsymbol{\varepsilon^{re}}$, and detwinning strain $\boldsymbol{\varepsilon^{de}}$:

$$\boldsymbol{\varepsilon^m} = \boldsymbol{\varepsilon^{tr}} + \boldsymbol{\varepsilon^{re}} + \boldsymbol{\varepsilon^{de}} \tag{2.45}$$

The model considers 24 martensite variants. Transformation strain $\boldsymbol{\varepsilon^{tr}}$ is related to the martensitic volume fraction ξ_{tr}^{α} and strain tensor Λ^{α} of each variant by equation:

$$\boldsymbol{\varepsilon^{tr}} = \sum_{\boldsymbol{\alpha=1}}^{\boldsymbol{24}} \xi_{tr}^{\alpha} \boldsymbol{\Lambda}^{\alpha} \tag{2.46}$$

where

$$\boldsymbol{\Lambda}^{\alpha} = \frac{1}{2} g^{tr} (\boldsymbol{m}^{\alpha} \otimes \boldsymbol{n}^{\alpha} + \boldsymbol{n}^{\alpha} \otimes \boldsymbol{m}^{\alpha}) \tag{2.47}$$

In this equation, g^{tr} is the magnitude of shearing deformation caused by transformation. $\boldsymbol{m}^{\alpha}$ and $\boldsymbol{n}^{\alpha}$ are transformation orientation and habit plane normal vectors, respectively. In their model, strain caused by the reorientation of twinned martensite is chosen the same as that of Thamburaja et al. [124] and is expressed as:

$$\boldsymbol{\varepsilon}^{\boldsymbol{re}} = \sum_{\boldsymbol{j>i}}^{\boldsymbol{24}} \sum_{\boldsymbol{i=1}}^{\boldsymbol{23}} \lambda^{ij}\, \mathbf{S}^{ij} \tag{2.48}$$

where λ^{ij} represents the amount of martensite transformed from *j*th to *i*th orientation due to reorientation of twinned martensite variants. $\mathbf{S}^{ij}$ is the orientation tensor which is expressed as:

$$\mathbf{S}^{ij} = \boldsymbol{\Lambda}^{i} - \boldsymbol{\Lambda}^{j} \tag{2.49}$$

When the term λ^{ij} is determined, the volume fraction of αth variant ξ_{re}^{α} can be calculated by the equation as:

$$\xi_{re}^{\alpha} = \sum_{\boldsymbol{j>i}}^{\boldsymbol{24}} \sum_{\boldsymbol{i=1}}^{\boldsymbol{23}} k^{\alpha ij}\, \lambda^{ij} \text{ with } \alpha = 1,2,\ldots, 24 \tag{2.50}$$

$$k^{\alpha ij} = \begin{cases} 1 & if\ \alpha = i \\ -1 & if\ \alpha > i\ and\ \alpha = j \\ 0 & otherwise \end{cases} \tag{2.51}$$

Therefore, the total volume fraction of martensite is expressed as:

$$\xi^{\alpha} = \xi_{tr}^{\alpha} + \xi_{re}^{\alpha} \tag{2.52}$$

During the process of martensite detwinning, strain is defined as the sum of the transition amount between two sub-variants, which is therefore written as:

$$\boldsymbol{\varepsilon}^{\boldsymbol{de}} = \sum_{\boldsymbol{\alpha=1}}^{\boldsymbol{24}} \xi^{\alpha}(\lambda^{\alpha} - \lambda_0^{\alpha})\boldsymbol{P}_{de}^{\alpha} \tag{2.53}$$

Here the volume fractions of two sub-variants in αth martensite variant are λ^{α} and $1 - \lambda^{\alpha}$, respectively. λ_0^{α} is the initial value of martensitic volume fraction. Orientation tensor $\boldsymbol{P}_{de}^{\alpha}$ has the form:

$$\boldsymbol{P}_{de}^{\alpha} = \frac{1}{2}(\boldsymbol{a}^{\alpha}\otimes\boldsymbol{w}^{\alpha} + \boldsymbol{w}^{\alpha}\otimes\boldsymbol{a}^{\alpha}) \tag{2.54}$$

In their model, plastic deformation is considered. Plastic strain is composed of two parts as:

$$\boldsymbol{\varepsilon}^{p} = \boldsymbol{\varepsilon}_{A}^{P} + \boldsymbol{\varepsilon}_{M}^{P} \tag{2.55}$$

In the BCC crystal, there are 12 primary slip systems. Therefore, total plastic strain caused by slip in austenite is written as:

$$\dot{\boldsymbol{\varepsilon}}_{A}^{p} = (1-\xi)\sum_{\beta=1}^{12}\dot{\gamma}_{A}^{\beta}\boldsymbol{P}_{A}^{\beta} \tag{2.56}$$

$$\boldsymbol{P}_{A}^{\beta} = \frac{1}{2}\left(\boldsymbol{s}_{A}^{\beta}\otimes\boldsymbol{I}_{A}^{\beta} + \boldsymbol{I}_{A}^{\beta}\otimes\boldsymbol{s}_{A}^{\beta}\right) \tag{2.57}$$

$$\xi = \sum_{\alpha=1}^{24}\xi^{\alpha} \tag{2.58}$$

where $\dot{\gamma}_{A}^{\beta}$ is the dislocation slipping rate of βth system in the austenitic phase, $\boldsymbol{P}_{A}^{\beta}$ is orientation tensor, $\boldsymbol{s}_{A}^{\beta}$ is slip direction, and $\boldsymbol{I}_{A}^{\beta}$ is slip plane normal of the βth system. ξ is total volume fraction of the martensitic phase. Plastic strain of the martensitic phase is related to deformation of the twinnning systems. There are 11 twinnning systems for NiTi martensite. Therefore, plastic strain of the martensite is:

$$\dot{\boldsymbol{\varepsilon}}_{M}^{p} = \xi\sum_{\beta_1=1}^{11}\dot{f}_{M}^{\beta_1}\boldsymbol{\Lambda}_{M}^{\beta_1} \tag{2.59}$$

$$\boldsymbol{\Lambda}_{M}^{\beta_1} = \frac{1}{2}g_{twin}^{\beta_1}\left(\boldsymbol{m}_{twin}^{\beta_1}\otimes\boldsymbol{n}_{twin}^{\beta_1} + \boldsymbol{n}_{twin}^{\beta_1}\otimes\boldsymbol{m}_{twin}^{\beta_1}\right) \tag{2.60}$$

where $\dot{f}_{M}^{\beta_1}$ is the rate of twinning volume fraction for β_1th twinning system of martensite, $\boldsymbol{\Lambda}_{M}^{\beta_1}$ is strain of theβ_1th twinning system, $\boldsymbol{m}_{twin}^{\beta_1}$ and $\boldsymbol{n}_{twin}^{\beta_1}$ are twinning orientation and twinning plane normal, respectively. $g_{twin}^{\beta_1}$ is the magnitude of shearing deformation of the β_1th twinning system. In a representative volume element (RVE) of NiTi SMA, Helmholtz free energy ψ can be written as:

$$\psi = \psi^{e} + \psi^{m} + \psi^{p} \tag{2.61}$$

where ψ^e is elastic energy, ψ^m is reorientation and detwinning energy, ψ^p is plastic energy. They have the form:

$$\begin{cases} \psi^e(\boldsymbol{\varepsilon}^e, \xi) = \frac{1}{2}\boldsymbol{\varepsilon}^e : C(\xi) : \boldsymbol{\varepsilon}^e \\ \psi^m(T, \xi^\alpha, t) = c\left[(T - T_0) - Tln\left(\frac{T}{T_0}\right)\right] + \mu(T - T_0)\sum_{\alpha=1}^{24}\xi^\alpha + \frac{1}{2}\sum_{\alpha=1}^{24}H(\xi^\alpha)^2 + \int_0^t \sum_{\alpha=1}^{24}\xi^\alpha X_M^\alpha \left|\dot{\lambda}^\alpha\right| dt \\ \dot{\psi}^p = (1-\xi)\sum_{\beta=1}^{12}R_A^\beta\left|\dot{\gamma}_A^\beta\right| + \xi\sum_{\beta_1=1}^{11}Q_M^{\beta_1}\dot{f}_M^{\beta_1} \end{cases} \tag{2.62}$$

Clausius dissipative inequality can be applied to the equation as:

$$\Gamma = \dot{w} - \dot{\psi} - \eta\dot{T} - \frac{\boldsymbol{q}\cdot\nabla T}{T} \geq 0 \tag{2.63}$$

where $\dot{w}$ is the external power and can be written as $\dot{w} = \boldsymbol{\sigma} : \dot{\boldsymbol{\varepsilon}}$. Therefore, the driving force for transformation π_{tr}^α, reorientation π_{re}^{ij}, detwinning π_{de}^α, plastic deformation of austenite F_{Aslip}^β and plastic deformation of martensite $F_{Mtwin}^{\beta_1}$ can be written as:

$$\pi_{tr}^\alpha = \boldsymbol{\sigma}: [\boldsymbol{\Lambda}^\alpha + (\lambda^\alpha - \lambda_0^\alpha)\boldsymbol{P}_{de}^\alpha] - \mu(T - T_0) - \boldsymbol{H}\xi^\alpha - \frac{1}{2}\boldsymbol{\varepsilon}^e : \Delta\boldsymbol{C} : \boldsymbol{\varepsilon}^e \tag{2.64}$$

$$\pi_{re}^{ij} = \boldsymbol{\sigma}: \left[\boldsymbol{S}^{ij} + \sum_{\boldsymbol{\alpha=1}}^{\boldsymbol{24}}(\lambda^\alpha - \lambda_0^\alpha)k^{\alpha ij}\boldsymbol{P}_{de}^\alpha\right] - \sum_{\boldsymbol{\alpha=1}}^{\boldsymbol{24}}k^{\alpha ij}H\xi^\alpha \tag{2.65}$$

$$\pi_{de}^\alpha = |\boldsymbol{\sigma}: \boldsymbol{P}_{de}^\alpha| - X_M^\alpha \tag{2.66}$$

$$F_{Aslip}^\beta = |\boldsymbol{\sigma}: \boldsymbol{P}_A^\alpha| - R_A^\beta \tag{2.67}$$

$$F_{Mtwin}^{\beta_1} = \boldsymbol{\sigma}: \boldsymbol{\Lambda}_M^{\beta_1} - Q_M^{\beta_1} \tag{2.68}$$

The simulated stress strain curve by the micro-macro model is compared with the experimental result by Shaw and Kyriakides [57]. Simulated results match well with experiment under different temperatures. The comparation between the model and experimental results in shown in Fig. 2.23.

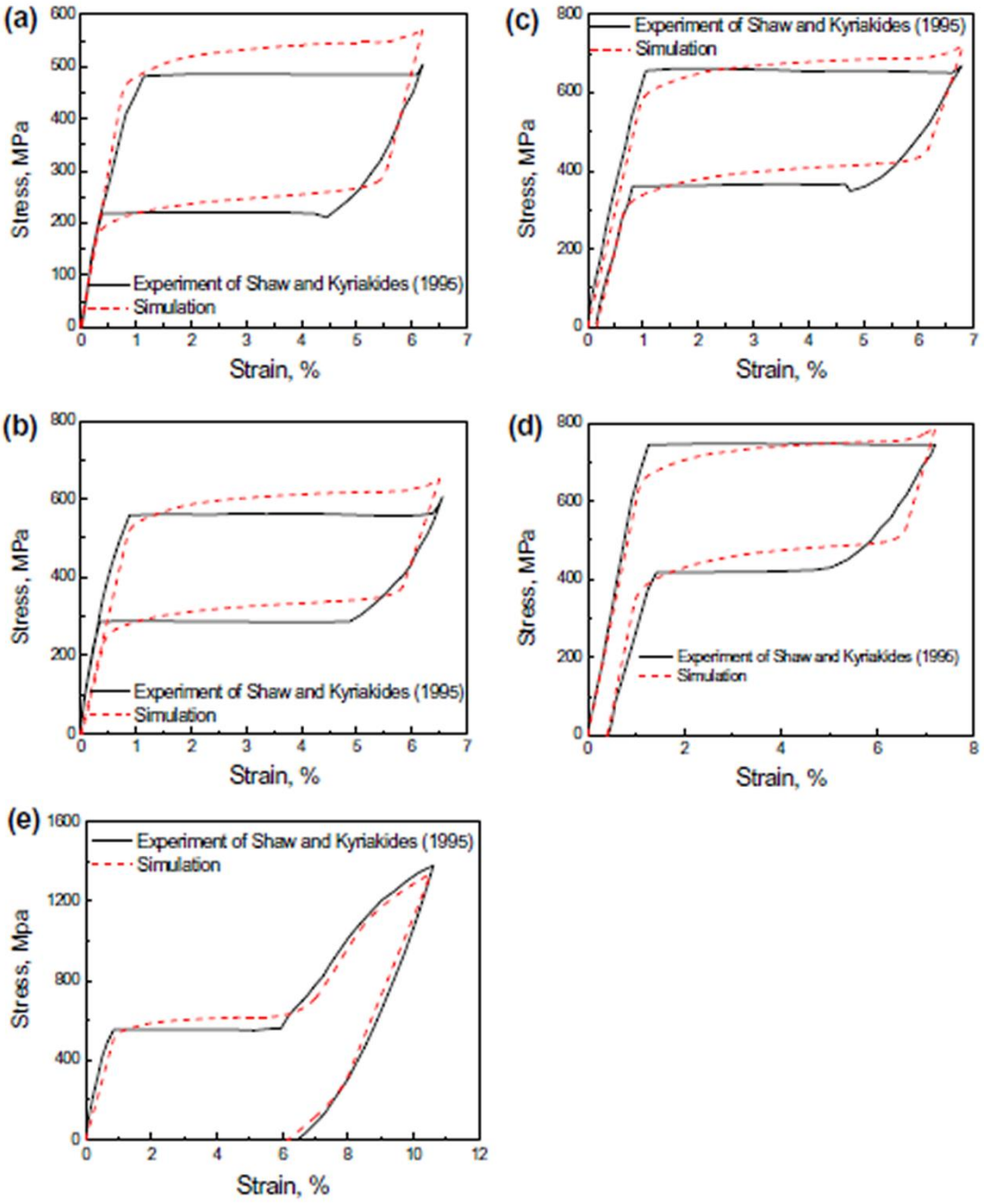

Fig. 2.23 Stress–strain curves of the NiTi shape memory alloy (initially austenite) in uniaxial tension-unloading tests at different temperatures: (a) 333 K; (b) 343 K; (c) 353 K; (d) 363 K; (e) 343 K (with high applied stress) [120]

2.7.3 Macroscopic Models

To save time for computer calculation, macroscopic models are established based on experimental data. The phenomenological model was first established by Tanaka and Nagaki

[125] and later extended by other researchers [126-131]. Compared to microscopic and micro-macro models, only macroscopic parameters are considered. Total energy of the system is composed of Gibbs free energy of austenitic phase, martensitic phase and free energy of mixture. Free energy of the sample is related to temperature, stress, strain, and martensitic volume fraction. Typical macroscopic models can be referred to as models of Lagoudas et al. [132-135], Lexcellent et al. [136], Auricchio et al. [137-139], and Zaki et al. [126, 129, 140-142]. In research by Lagoudas et al. [132-135], martensitic transformation is described by a theory similar to J2-type plasticity theory. Phase transformation has the same direction as flow stress direction, and yield surfaces are introduced for transformation. Minimum Gibbs free energy and the increase of entropy during phase transformation are the base assumptions for the constitutive model. Gibbs free energy of the whole system is composed of elastic energy, transformation-related energy and temperature-related energy. The driving force for transformation is then related to system stress, strain, and temperature. Gibbs free energy is established vis a vis transformation hardening. Transformation hardening functions are established with exponential, cosine, and polynomial forms, respectively. Transformation-induced plasticity isalso considered. In the recent model, nonlinear hardening equations are chosen to smooth stress strain curves of SMAs. Based on this model, the irrecoverable plastic deformation during phase transformation is studied. The model is later extended to simulate magnetic-field-induced phase transformation by adding to the Gibbs free energy additional items related to the magnetic field. Phase transformation during crack propagation is also studied in the model. In research by Lexcellent et al. [136], the reorientation of martensite variants is first considered. The interaction energy of martensite

variants is added to the total Gibbs free energy. In the research, J2 and J3 flow rules are taken to model tension-compression asymmetry. Phase transformation near the crack was also considered. Auricchio et al. model [137-139] the fatigue properties of SMAs during cyclic loading. Plastic deformation and phase transformation behavior of dense and porous SMAs were modeled recently in their group. The reorientation of martensite under nonproportional loading is modeled by Zaki [137-139].

The following section discusses in detail macroscopic models by taking Zaki and Moumni's model [129, 142] as representative. In their model, the Helmholtz free energy potential ϕ is related to temperature T, martensitic volume fraction ξ, local transformation strain tensor for austenite ε_A and martensite ε_M, and local martensite orientation strain tensor ε^{ori} as:

$$\phi\left(T, \varepsilon_A, \varepsilon_M, \varepsilon^{ori}, \xi\right) = (1-\xi)\phi_A + \xi\phi_M + I_{AM} \tag{2.69}$$

where

$$\begin{cases} \phi_A(\boldsymbol{\varepsilon_A}) = \frac{1}{2}\boldsymbol{\varepsilon_A}\colon \boldsymbol{K_A}\colon \boldsymbol{\varepsilon_A} \\ \phi_M(\boldsymbol{\varepsilon_M}, \boldsymbol{\varepsilon^{ori}}, T) = \frac{1}{2}(\boldsymbol{\varepsilon_M} - \boldsymbol{\varepsilon^{ori}})\colon \boldsymbol{K_M}\colon (\boldsymbol{\varepsilon_M} - \boldsymbol{\varepsilon^{ori}}) + C_0 + \zeta\left(T - A_f^0\right) \\ I_{AM} = G\frac{\xi^2}{2} + b_1\frac{\xi^2}{2}\left(\frac{2}{3}\boldsymbol{\varepsilon^{tr}}\colon\boldsymbol{\varepsilon^{tr}}\right) + b_2\frac{\xi}{2}(1-\xi)\left(\frac{2}{3}\boldsymbol{\varepsilon^{tr}}\colon\boldsymbol{\varepsilon^{tr}}\right) \end{cases} \tag{2.70}$$

where $\boldsymbol{K_A}$ is elastic stiffness tensor of austenite, $\boldsymbol{K_M}$ is elastic stiffness tensor of martensite, C_0 is the value of heat density of phase transformation $C(T)$ for $T = A_f^0$ and $\boldsymbol{\sigma} = 0$. ζ controls the influence of temperature on transformation stress. Transformation hardening energy ϕ_{KT} is written as:

$$\phi_{KT} = \lambda_1\xi + \lambda_2(1-\xi) + \lambda_3\left(\varepsilon_{max}^{tr} - \sqrt{\frac{2}{3}\boldsymbol{\varepsilon}^{tr}\colon\boldsymbol{\varepsilon}^{tr}}\right) + \boldsymbol{\lambda}\colon[(1-\xi)\boldsymbol{\varepsilon}_A + \xi\boldsymbol{\varepsilon}_M - \boldsymbol{\varepsilon}] \tag{2.71}$$

where $\boldsymbol{\varepsilon}$ is macroscopic strain, and λ_1, λ_2, λ_3, and $\boldsymbol{\lambda}$ are Lagrange multipliers associated with the following Kuhn-Tucker conditions:

$$\begin{cases} \lambda_1 \geq 0, \text{and } \lambda_1 \xi = 0 \\ \lambda_2 \geq 0, \text{and } \lambda_2 (1-\xi) = 0 \\ \lambda_3 \geq 0 \text{ and } \lambda_3 \left(\varepsilon_{max}^{tr} - \sqrt{\frac{2}{3} \boldsymbol{\varepsilon}^{ori} : \boldsymbol{\varepsilon}^{ori}} \right) = 0 \end{cases} \tag{2.72}$$

The constitutive equation is then reduced to an optimization of Lagrangian:

$$L\left(T, \boldsymbol{\varepsilon}, \boldsymbol{\varepsilon}_A, \boldsymbol{\varepsilon}_M, \boldsymbol{\varepsilon}^{ori}, \xi\right) = (1-\xi)\phi_A + \xi \phi_M + I_{AM} + \phi_{KT} \tag{2.73}$$

Therefore, dissipation energy D_p is written as:

$$D_p = [a_1(1-\xi) + a_2 \xi] \left| \dot{\xi} \right| + \xi^2 \boldsymbol{\varepsilon}^{ori} \sqrt{\frac{2}{3} \boldsymbol{\varepsilon}^{tr} : \boldsymbol{\varepsilon}^{tr}} \tag{2.74}$$

In the equation, a_1 and a_2 control the width of the pseudoelastic hysteresis loop for $\xi = 0$ and 1. The driving force for forward transformation, reverse transformation and orientation is written as:

$$\begin{cases} F_\xi^F = A_\xi - [a_1(1-\xi) + a_2 \xi] \\ F_\xi^R = -A_\xi - [a_1(1-\xi) + a_2 \xi] \\ F_{ori} = \frac{F_{tr}}{\xi} = \left\| \frac{A_{tr}}{\xi} \right\| - \xi Y \text{ for } \xi > 0 \end{cases} \tag{2.75}$$

where $A_\xi = -\frac{\partial L}{\partial \xi}$ and $A_{tr} = -\frac{\partial L}{\partial \varepsilon^{tr}}$. If $F_\xi^F < 0$ and $F_\xi^R < 0$, no phase transformation is activated and $\dot{\xi} = 0$. If $F_\xi^F = 0$, forward transformation is activated. Therefore, $\dot{\xi} = 0$ when $\dot{F}_\xi^F < 0$ or $\dot{F}_\xi^F = 0$ otherwise. If $F_\xi^R = 0$, reverse transformation is activated. Therefore, $\dot{\xi} = 0$ when $\dot{F}_\xi^R < 0$ or $\dot{F}_\xi^R = 0$ otherwise. If $F_{ori} = 0$, the onset of martensite orientation is reached. Therefore,

$$\dot{\boldsymbol{\varepsilon}}^{tr} = \eta \frac{\partial F_{ori}}{\partial \boldsymbol{X}} \tag{2.76}$$

where $\boldsymbol{X}$ is the deviatoric part of $dev(A^{tr})/\xi$ and η is a positive scalar that satisfies the Kuhn-Tucker conditions:

$$\eta \geq 0, F_{ori} \leq 0, \text{ and } \eta F_{ori} = 0 \tag{2.77}$$

The comparison between experiment and model is shown in Fig. 2.24. Numerical predictions show good agreement with experimental data for both pseudoelasticity and orientation of self-accommodated martensite under various temperatures.

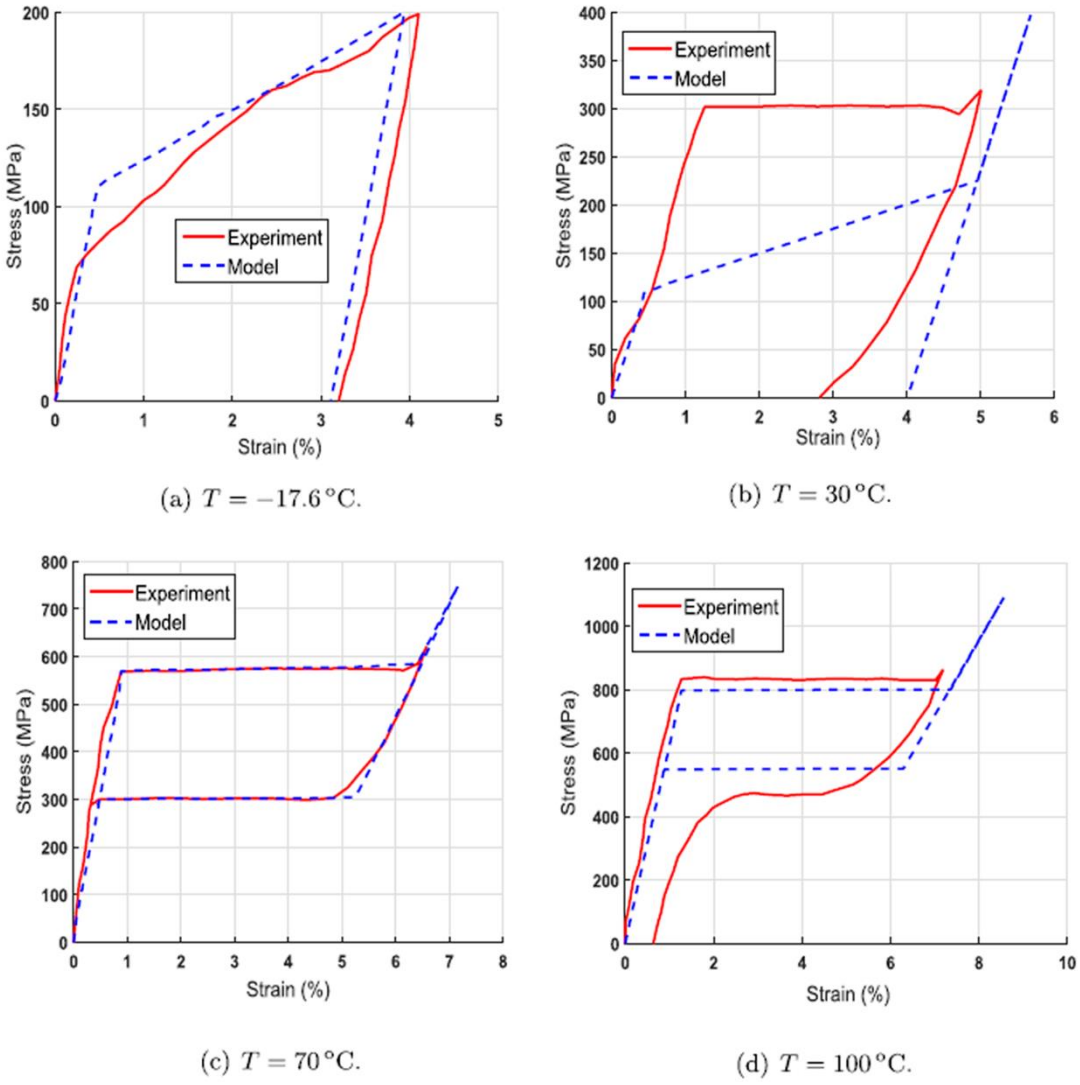

Fig.2.24 Numerical vs experimental stress-strain curves in uniaxial tension at different temperatures [129]

2.8 Review of Research on High Strain Rate Deformation of NiTi SMAs

The constitutional relationship of NiTi SMAs is strain rate sensitive. The effect of strain rate on transformation behavior in austenitic NiTi SMAs has been studied preliminarily [143-146]. C. Elibol and M.F.-X. Wagner [146] studied the effect of strain rate ranging from

10^{-4}/s to 10^{3}/s on tension, compression (Fig. 2.25) and shearing of austenitic NiTi SMAs. They reported that transformation stress as well as slopes of the stress–strain curves in the transformation region increase with increasing strain rate for all loading conditions. This phenomenon is attributed to latent heat generated during phase transformation. The relationship between the increase of temperature and strain rate was studied by Hao Yin et al. [145]. In their study, samples are loaded to 6% strain and strain rates ranging from 4.8×10^{-5}/s to 1.2×10^{-1}/s. Temperature increases from 5.2°C at 4.8×10^{-5}/s to 23°C at 1.2×10^{-1}/s. A similar trend was noticed by Aslan Ahadi et al. [144]. In their study, strain rate ranges from 4×10^{-5}/s to 1×10^{-1}/s. Temperature increases with strain rate regardless of grain size. Full-field thermographic imaging was used to map thermal changes as a function of strain rate loading. The largest change in temperature of 27.1°C occurs at deformation strain of 7% at strain rate 10^{-1}/s in the sample with grain size 90 nm.

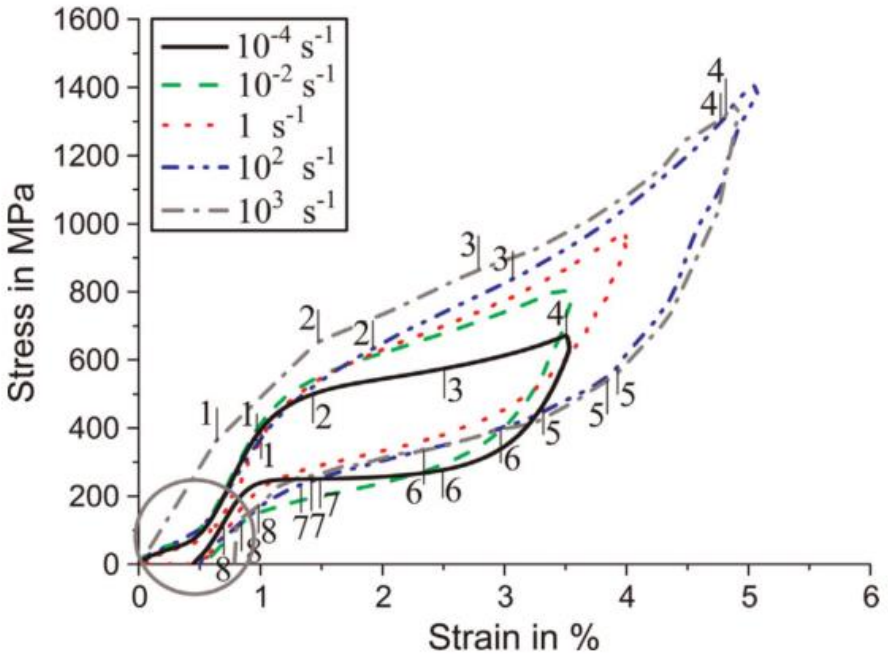

Fig. 2.25 Engineering stress–strain curves of five virgin NiTi samples at strain rates from 10^{-4} /s to 10^{-3} /s under simple compressive loading [146].

Temperature dependence of plateau stress for forward transformation (dσ/dT) ranges from 4.37 MPa/K (grain size 27 nm) to 6.43 MPa/K (grain size 90 nm). Clausius-Clapeyron equation is used to estimate the relationship between the increase of temperature and stress by Sia Nemat-Nasser et al. [143]. Temperature increase is attributed to deformation work and latent heat of phase transformation. The temperature dependence of plateau stress for forward transformation (dσ/dT) increases with strain rate. An apparent increase of plateau stress for phase transformation and slope of stress-strain curve in the transformation region is also noticed when strain rate increases from 330 /s to 1080 /s (Fig. 2.26). Chen and Bo [147] studied temperature effect on the stress strain curve of NiTi SMAs deformed at 430/s. The sample is deformed at temperatures ranging from 0 ℃ to 50 ℃. Work hardening behavior is observed with increasing temperature. Details are shown in Fig. 2.27.

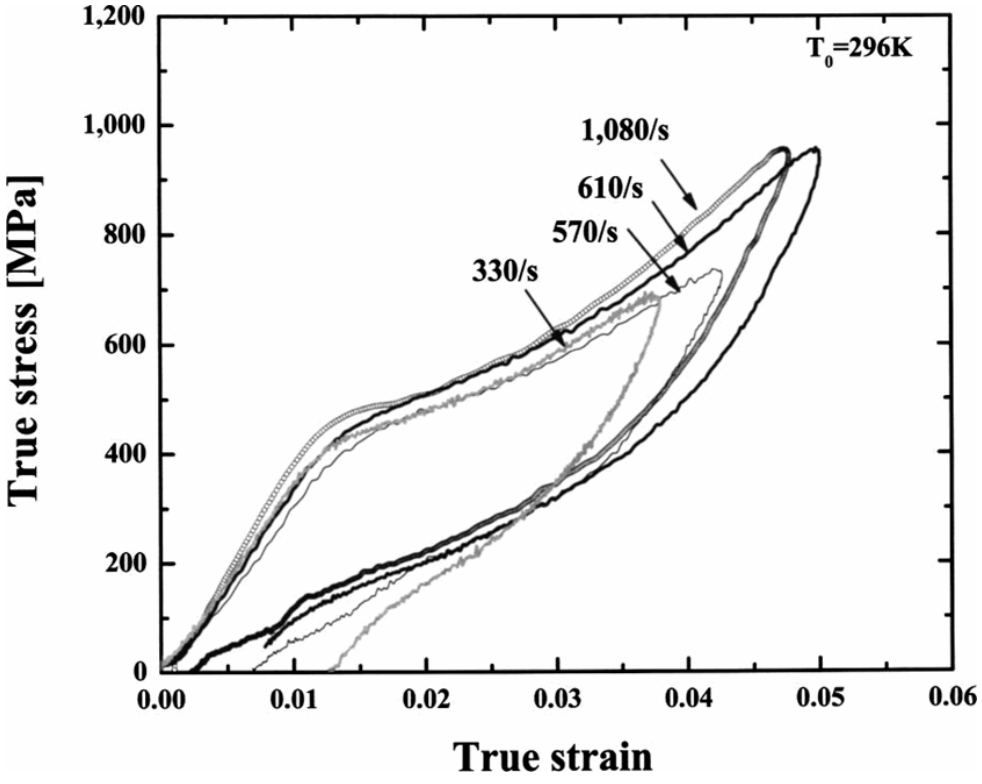

Fig. 2.26 Dynamic stress–strain relations for NiTi shape-memory alloy at indicated strain rates [143]

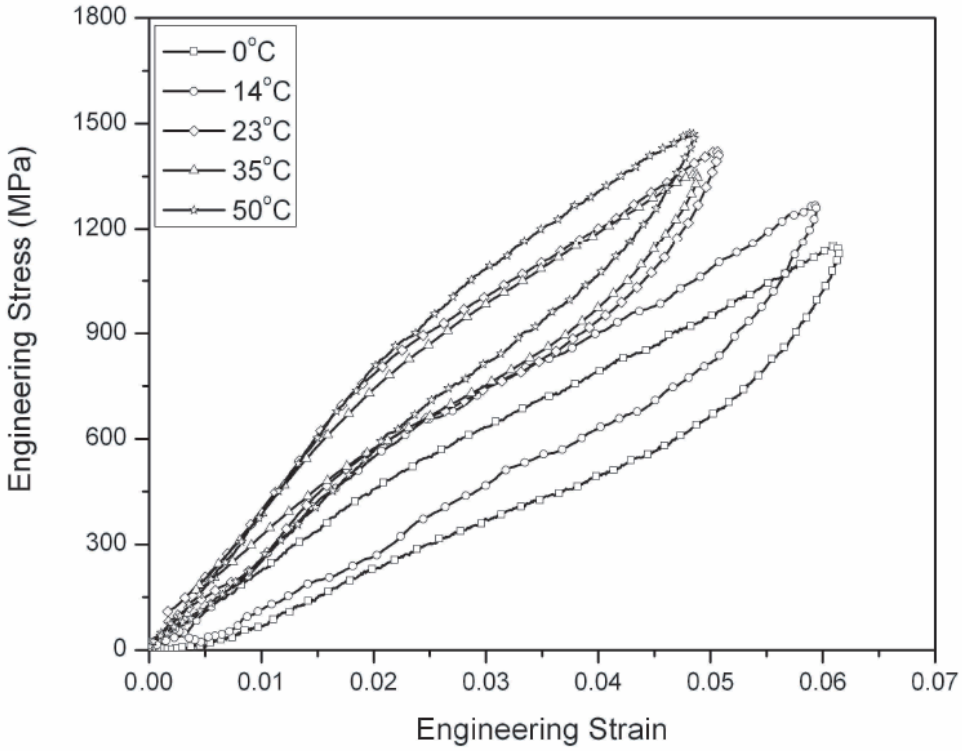

Fig. 2.27 Dynamic compressive stress strain curves of the NiTi shape memory alloys at different deformation temperature [147]

Phase boundaries of NiTi austenite and martensite propagate during deformation; the difference of phase front velocity between quasi-static and dynamic deformation has been studied briefly [57, 148, 149]. Shaw and Kyriakides [57] studied phase front velocity when the polycrystalline NiTi SMA wire is deformed at strain rates from 4×10^{-5} to 4×10^{-2} /s. They reported that propagation speed of the phase transformation front ranges from 0.25 mm/s to 2.31 mm/s at different strain rates. Compared to quasi-static deformation, a much higher velocity of phase front is noticed in high strain rate deformation. Escobar et al. [148] studied stress-induced phase transformation in NiTi at the extremely high strain rate of 10^4 /s. Velocity was 327 m/s. Niemczura and Ravi-Chandar [149] studied the propagation of phase boundaries of NiTi under quasi-dynamic conditions. The nucleation and propagation of phase fronts were noticed in their experiment, and the phase fronts move in a speed ranging from 37

m/s to 370 m/s. They also reported that the driving force for phase transformation is related to propagation speed of the phase front.

While significant experimental research on the strain rate effect on deformation of NiTi SMAs in high strain rate deformation has been performed, modeling in this field is limited. Based on experimental data, Niemczura and Ravi-Chandar [149] established a model connecting the volume fraction of transformed martensite and the speed of the phase front. In their model, the simplest tri-linear stress-strain constitutive law is applied for both quasi-static and high strain rate deformation. Strain energy is calculated by jump discontinuities in the phase front. By assuming maximum energy dissipation in the process of phase boundary propagation, the driving force for phase transformation is calculated. Chen and Lagoudas [150] established a model describing the propagation of stress waves and phase transformation fronts in NiTi SMA rod. The quasi-static thermomechanical constitutive relationship for NiTi SMAs developed by Lagoudas et al. [130, 151] was used for impact conditions. Wave equations and jump conditions in the phase fronts are considered. Two waves are assumed to coexist in the rod. One separates the tranquil and disturbed regions with acoustic speed 3300 m/s; and another separates the austenitic and martensitic phases with phase boundary speed ranging from 911 m/s to 1100 m/s. According to their model, martensitic transformation is activated when stress exceeds 165 MPa, which brings a jump of temperature and stress at the acoustic front. Stress and temperature are continuous until stress exceeds 586 MPa. A maximum increase of temperature of 56.5 K is estimated when stress equals 800 MPa. Stress increase is connected to temperature increase when the impact condition can be seen as an adiabatic process. When jump conditions meet, jump leads to a

higher stress level than stress when only the temperature effect is considered (Fig. 2.28).

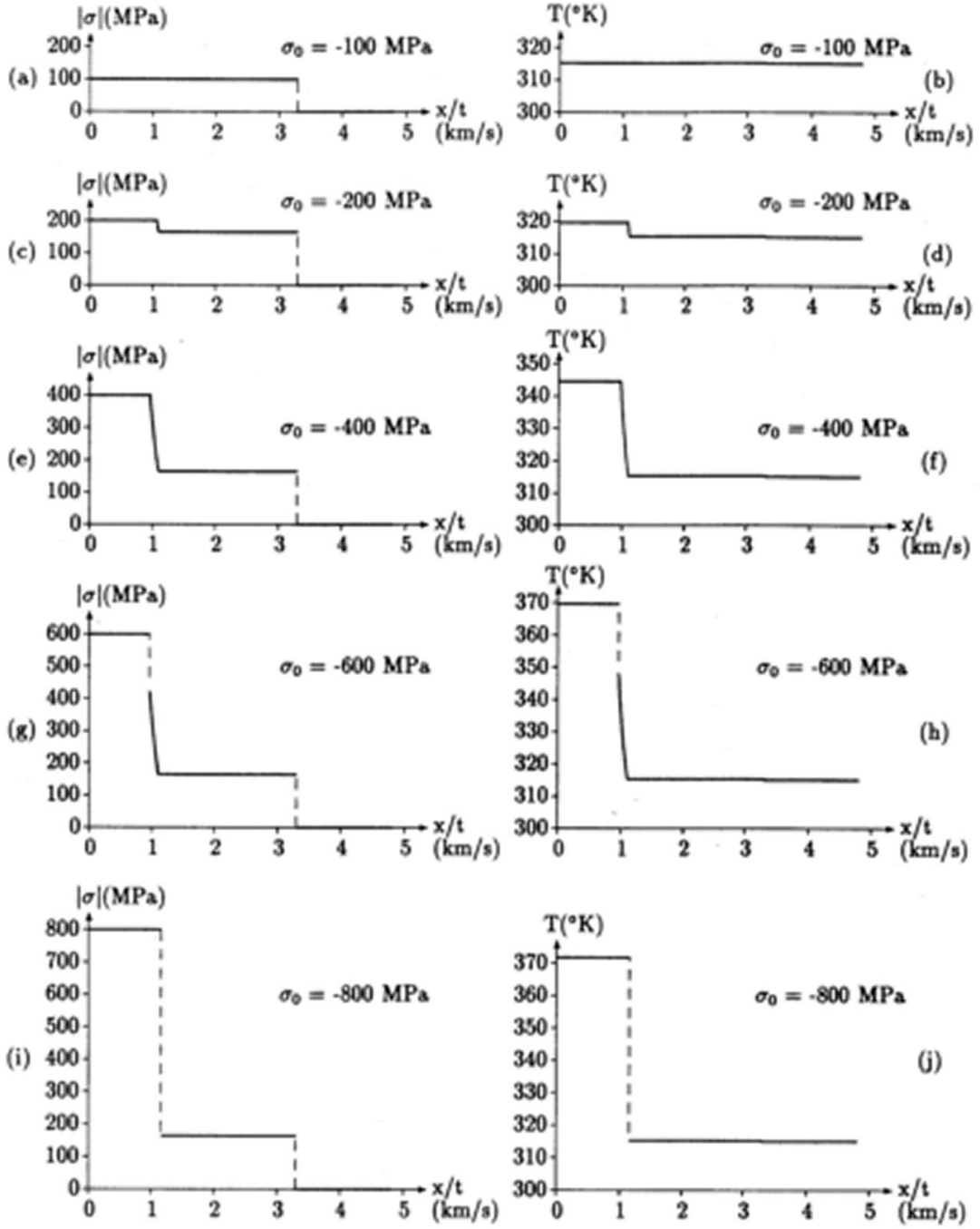

Fig.2.28 Simulated stress and temperature distribution at phase front during impact deformation [150]

Bekker et al. [152] talked about wave propagation in SMA rods in adiabatic and isothermal cases with different boundary conditions. The stress strain relationship at high strain rate deformation in their model is based on the 1-D rate-independent constitutive law

[153, 154]. Different wave structures of the solution to the impact problem are established on 1-D field equations for isothermal and adiabatic cases. According to their model, acoustic speed is 3300 m/s for both cases. Velocity for the phase front is 650 m/s for the isothermal case and 740 m/s for the adiabatic case. Based on the model similar to [150, 152], Lagoudas et al. [134] studied wave structure in the SMA rod when deformed by impact loading, and the modeling results were then compared with experimental results from split Hopkinson bar testing. The experiment is similar to that done by Shaw and Kyriakides [57] and Escobar et al. [148]. A set of strain gages are set in the specimen with a specially designed distance to each other. Strain and stress information at each strain gage is then collected. Elastic wave velocity and phase front are 3294 m/s and 723 m/s, respectively.

2.9 References

[1] Ölander A. Journal of the American Chemical Society 1932;54:3819.

[2] Ölander A. Zeitschrift für Kristallographie-Crystalline Materials 1932;83:145.

[3] A. B. Greninger and V. G. Mooradian. Transactions of the Metallurgical Society of AIME 1938;vol. 128:337.

[4] Kurdyumov G, Khandros L. On the thermoelastic equilibrium in martensitic transformations. Dokl. Akad. Nauk SSSR, vol. 66, 1949. p.211.

[5] L.C. Chang TAR. Transactions of the American Institute of Mining and Metallurgical Engineers 1951;191:47.

[6] Buehler W, Wiley R. Nickel-base alloys. Google Patents, 1965.

[7] Buehler WJ, Wang FE. Ocean Engineering 1968;1:105IN7109.

[8] Buehler W, Wiley R. The properties of TiNi and associated phases. DTIC Document, 1961.

[9] Abeyaratne R, Chu C, James RD. Philosophical Magazine A 1996;73:457.

[10] Song K, Pauly S, Zhang Y, Gargarella P, Li R, Barekar N, Kühn U, Stoica M, Eckert J. Acta Materialia 2011;59:6620.

[11] Gall K, Jacobus K, Sehitoglu H, Maier HJ. Metallurgical and Materials Transactions A 1998;29:765.

[12] Otsuka H, Yamada H, Maruyama T, Tanahashi H, Matsuda S, Murakami M. ISIJ international 1990;30:674.

[13] Jani JM, Leary M, Subic A, Gibson MA. Materials & Design 2014;56:1078.

[14] Duerig TW, Melton K, Stöckel D. Engineering aspects of shape memory alloys: Butterworth-Heinemann, 2013.

[15] Barbarino S, Flores ES, Ajaj RM, Dayyani I, Friswell MI. Smart Materials and Structures 2014;23:063001.

[16] Stoeckel D, Pelton A, Duerig T. European radiology 2004;14:292.

[17] Gil F, Planell J. Journal of Biomedical Materials Research Part A 1999;48:682.

[18] Kahn H, Huff M, Heuer A. Journal of Micromechanics and Microengineering 1998;8:213.

[19] Van Humbeeck J. Materials Science and Engineering: A 1999;273:134.

[20] Hartl DJ, Lagoudas DC. Proceedings of the Institution of Mechanical Engineers, Part G: Journal of Aerospace Engineering 2007;221:535.

[21] Hunter AM, Bacon JW. Transactions of the American Electrochemical Society

1920;37:520.

[22] Vogel R, Wallbaum HJ. Archiv fuer das Eisenhuettenwesen 1938;12:299.

[23] Laves F, H.J. Wallbaum. Naturwissenschaften 1939;27:674.

[24] Laves FaHJW. Zeir. fur Kristal. 1939;101:78.

[25] Duwez P, J.L. Taylor. Transactions AIME 1950;188:1173.

[26] Poole DM, W. Hume-Rothery. Journal of the Institute of Metals 1954-1955;83:473.

[27] Hansen M, K. Anderko. McGraw-Hill book company, Inc, New York. 1958:1049.

[28] Wasilewski RJ, S.R. Butler, J.E. Hanlon, D. Worden. Metallurgical Transactions A 1971;2:229.

[29] Koskimaki D, M.J. Marcinkowski, A.S. Sastri. Transactions of the Metallurgical Society of AIME 1969;245:1883.

[30] K. Otsuka, T. Sawamura, K. Shimizu. Physica Status Solidi (a) 1971;5 457.

[31] Hughes H. The Journal of the Iron and Steel Institute 1965;203:1019.

[32] Nishida M, Wayman CM, Honma T. Metallurgical Transactions A 1986;17:1505.

[33] Kainuma R, M. , Matsumoto, T. Honma. Tohoku Daigaku Senko Seiren Kenkyujo iho 1987;43:149.

[34] Huang X, Ackland GJ, Rabe KM. Nature materials 2003;2:307.

[35] Hwang C, Meichle M, Salamon M, Wayman C. Philosophical Magazine A 1983;47:31.

[36] Sedlak P, Frost M, Benešová B, Zineb TB, Šittner P. International Journal of Plasticity 2012;39:132.

[37] Šittner P, Landa M, Lukáš P, Novák V. Mechanics of Materials 2006;38:475.

[38] Parlinski K, Parlinska-Wojtan M. Physical Review B 2002;66:064307.

[39] Otsuka K, Ren X. Intermetallics 1999;7:511.

[40] Zhang X, Xia B, Song J, Chen B, Tian X, Hao Y, Xie C. Journal of Alloys and Compounds 2011;509:6296.

[41] Ravari BK, Farjami S, Nishida M. Acta Materialia 2014;69:17.

[42] Chen Q, Wu X, Ko T. Scripta metallurgica et materialia 1993;29:49.

[43] Kim J, Liu Y, Miyazaki S. Acta Materialia 2004;52:487.

[44] Bojda O, Eggeler G, Dlouhý A. Scripta materialia 2005;53:99.

[45] Nishida M, Yamauchi K, Itai I, Ohgi H, Chiba A. Acta metallurgica et materialia 1995;43:1229.

[46] Pitteri M, Zanzotto G. Continuum models for phase transitions and twinning in crystals: CRC Press, 2002.

[47] Duerig T, Bhattacharya K. Shape Memory and Superelasticity 2015;1:153.

[48] Saburi T, Nenno S, Fukuda T. Journal of the Less Common Metals 1986;125:157.

[49] Otsuka K, Wayman CM. Shape memory materials: Cambridge university press, 1999.

[50] Fukuda T, Deguchi A, Kakeshita T, Saburi T. Materials Transactions, JIM 1997;38:514.

[51] Nishida M, Honma T. Scripta Metallurgica 1984;18:1293.

[52] Miyazaki S, Otsuka K. Philosophical Magazine A 1985;50:393.

[53] Kwarciak J, Lekston Z, Morawiec H. Journal of Materials Science 1987;22:2341.

[54] Xie C, Zhao L, Lei T. Scripta Metallurgica et Materialia 1990;24:1753.

[55] Michal G, Sinclair R. Acta Crystallographica Section B: Structural Crystallography and Crystal Chemistry 1981;37:1803.

[56] Adharapurapu RR, Jiang F, Vecchio KS. Materials Science and Engineering: A

2010;527:1665.

[57] Shaw JA, Kyriakides S. Journal of the Mechanics and Physics of Solids 1995;43:1243.

[58] Bhattacharya K. Microstructure of martensite: why it forms and how it gives rise to the shape-memory effect: Oxford University Press, 2003.

[59] Otsuka K, Shimizu K. Scripta metallurgica 1970;4:469.

[60] Bhattacharya K, Conti S, Zanzotto G, Zimmer J. Nature 2004;428:55.

[61] Ren X, Otsuka K. Physical Review Letters 2000;85:1016.

[62] Saburi T, Nenno S. Scripta Metallurgica 1974;8:1363.

[63] Nagasawa A, Enami K, Ishino Y, Abe Y, Nenno S. Scripta Metallurgica 1974;8:1055.

[64] Wang FE, Buehler WJ. Applied Physics Letters 1972;21:105.

[65] Nishida M, Wayman C, Honma T. Scripta metallurgica 1984;18:1389.

[66] Nishida M, Honma T. Scripta metallurgica 1984;18:1299.

[67] Stoeckel D. Materials & Design 1990;11:302.

[68] Butera F, Coda A, Vergani G, SpA SG. Nanotec IT newsletter. Roma: AIRI/nanotec IT 2007:12.

[69] Bil C, Massey K, Abdullah EJ. Journal of Intelligent Material Systems and Structures 2013;24:879.

[70] Duerig T, Pelton A, Stöckel D. Materials Science and Engineering: A 1999;273:149.

[71] Machado L, Savi M. Brazilian journal of medical and biological research 2003;36:683.

[72] Morgan N. Materials Science and Engineering: A 2004;378:16.

[73] Petrini L, Migliavacca F. Journal of Metallurgy 2011;2011.

[74] Baumbick RJ. Shape memory alloy actuator. Google Patents, 2000.

[75] Lortz BK, Tang A. Separation device using a shape memory alloy retainer. Google Patents, 1998.

[76] Huett B, Willey C. 2000.

[77] Birman V. Applied Mechanics Reviews 1997;50:629.

[78] Landis GA, PP. J. IEEE 1997:865.

[79] Hartl DJ, Lagoudas DC, Calkins FT, Mabe JH. Smart Materials and Structures 2010;19:015020.

[80] Hartl DJ, Mooney JT, Lagoudas DC, Calkins FT, Mabe JH. Smart Materials and Structures 2010;19:015021.

[81] Oehler S, Hartl D, Lopez R, Malak R, Lagoudas D. Smart Materials and Structures 2012;21:094016.

[82] Kudva JN. Journal of Intelligent Material Systems and Structures 2004;15:261.

[83] Pitt D, Dunne J, White E, Garcia E. SAMPSON smart inlet SMA powered adaptive lip design and static test. 19th AIAA Applied Aerodynamics Conference. American Institute of Aeronautics and Astronautics, 2001.

[84] C. S. Open Med Dev J 2010;2:24.

[85] Kaufman L, Cohen M. Trans. AIME 1956;206:1893.

[86] Kaufman L, Cohen M. Prog. Metall Phys. 1958;7:165.

[87] Cohen M. Trans. metall. Soc. of AIME, April 1958:171.

[88] Olson OB, Cohen M. Am. Inst. Min. Engrs, New York 1982:1145.

[89] Olson G, Cohen M. Metallurgical Transactions A 1976;7:1897.

[90] Olson G, Cohen M. Metallurgical and Materials Transactions A 1976;7:1905.

[91] Olson G, Cohen M. Metallurgical and Materials Transactions A 1976;7:1915.

[92] Bowles J, Mackenzie J. Acta metallurgica 1954;2:129.

[93] Bowles J, Mackenzie JK. Acta Metallurgica 1954;2:224.

[94] Mackenzie J, Bowles J. Acta Metallurgica 1954;2:138.

[95] Lieberman DS, Wechsler MS, Read TA. J. Applied Physics 1955;28:473.

[96] Wechsler MS, Lieberman DS, Read TA. Trans. AIME 1953;197:1503.

[97] Jaswon MA, Wheeler JA. Acta Crystallographica 1948;1:216.

[98] G. K, G. S. Z. Phys. 1930;64:325.

[99] Bain EC. Trans. AIME 1924;70 25.

[100] Zhu W-J, Chen W-Y, Hsu TY. Acta Metallurgica 1985;33:2075.

[101] Falk F. Zeitschrift für Physik B Condensed Matter 1983;51:177.

[102] Ball JM, James RD. Fine Phase Mixtures as Minimizers of Energy. Analysis and Continuum Mechanics: A Collection of Papers Dedicated to J. Serrin on His Sixtieth Birthday. Berlin, Heidelberg: Springer Berlin Heidelberg, 1989. p.647.

[103] Levitas VI, Preston DL, Lee D-W. Physical Review B 2003;68:134201.

[104] Wang Y, Khachaturyan AG. Acta Materialia 1997;45:759.

[105] Cho J-Y, Idesman A, Levitas V, Park T. International Journal of Solids and Structures 2012;49:1973.

[106] Zhong Y, Zhu T. Acta Materialia 2014;75:337.

[107] Suzuki T, Shimono M. A simple model for martensitic transformation. Journal de Physique IV (Proceedings), vol. 112: EDP sciences, 2003. p.129.

[108] Sato T, Saitoh K, Shinke N. Materials Science and Engineering: A 2008;481:250.

[109] Uehara T, Asai C, Ohno N. Modelling and Simulation in Materials Science and Engineering 2009;17:035011.

[110] Chowdhury P, Patriarca L, Ren G, Sehitoglu H. International Journal of Plasticity 2016;81:152.

[111] Alder BJ, Wainwright T. J. Chem. Phys. 1959;31 459.

[112] Maranganti R, Sharma P. Revisiting quantum notions of stress. Proceedings of the Royal Society of London A: Mathematical, Physical and Engineering Sciences, vol. 466: The Royal Society, 2010. p.2097.

[113] Saitoh K-i, Liu WK. Computational Materials Science 2009;46:531.

[114] Mori T, Tanaka K. Acta metallurgica 1973;21:571.

[115] Šittner P, Novák V. International Journal of Plasticity 2000;16:1243.

[116] Stupkiewicz S, Górzyńska-Lengiewicz A. Continuum Mechanics and Thermodynamics 2012;24:149.

[117] Anand L, Gurtin ME. Journal of the Mechanics and Physics of Solids 2003;51:1015.

[118] Yu C, Kang G, Kan Q. Journal of the Mechanics and Physics of Solids 2015;82:97.

[119] Yu C, Kang G, Kan Q. Mechanics of Materials 2014;78:1.

[120] Yu C, Kang G, Kan Q. International Journal of Plasticity 2014;54:132.

[121] Thamburaja P, Pan H, Chau FS. International Journal of Plasticity 2009;25:2141.

[122] Thamburaja P, Anand L. Acta Materialia 2003;51:325.

[123] Ostwald R. Modelling and simulation of phase transformations in elasto-plastic polycrystals. 2015.

[124] Thamburaja P, Pan H, Chau F. Acta materialia 2005;53:3821.

[125] Tanaka K, Nagaki S. Ingenieur-Archiv 1982;51:287.

[126] Zaki W. Smart Materials and Structures 2010;19:025009.

[127] Hartl DJ, Chatzigeorgiou G, Lagoudas DC. International Journal of Plasticity 2010;26:1485.

[128] Boyd JG, Lagoudas DC. International Journal of Plasticity 1996;12:805.

[129] Zaki W, Moumni Z. Journal of the Mechanics and Physics of Solids 2007;55:2455.

[130] Bo Z, Lagoudas D. International Journal of Engineering Sciences 1999;37:1089.

[131] Cisse C, Zaki W, Ben Zineb T. International Journal of Plasticity 2016;76:244.

[132] Lagoudas D, Hartl D, Chemisky Y, Machado L, Popov P. International Journal of Plasticity 2012;32-33:155.

[133] Lagoudas DC, Entchev PB. Mechanics of Materials 2004;36:865.

[134] Lagoudas DC, Ravi-Chandar K, Sarh K, Popov P. Mechanics of Materials 2003;35:689.

[135] Lagoudas D, Bo Z. International Journal of Engineering Sciences 1999;37:1141.

[136] Lexcellent C, Blanc P, Creton N. Materials Science and Engineering: A 2008;481:334.

[137] Auricchio F, Boatti E, Reali A, Stefanelli U. Computer Methods in Applied Mechanics and Engineering 2016;299:440.

[138] Auricchio F, Reali A, Stefanelli U. International Journal of Plasticity 2007;23:207.

[139] Auricchio F, Taylor RL, Lubliner J. Computer Methods in Applied Mechanics and Engineering 1997;146:281.

[140] Zaki W. International Journal of Plasticity 2012;37:72.

[141] Zaki W. International Journal of Solids and Structures 2012;49:2951.

[142] Zaki W, Moumni Z. Journal of the Mechanics and Physics of Solids 2007;55:2427.

[143] Nemat-Nasser S, Yong Choi J, Guo W-G, Isaacs JB, Taya M. Journal of Engineering Materials and Technology 2005;127:83.

[144] Ahadi A, Sun Q. Acta Materialia 2014;76:186.

[145] Yin H, He Y, Sun Q. Journal of the Mechanics and Physics of Solids 2014;67:100.

[146] Elibol C, Wagner MFX. Materials Science and Engineering: A 2015;643:194.

[147] Chen W, Song B. Journal of Mechanics of Materials and Structures 2006;1:339.

[148] Escobar JC, Clifton RJ, Yang S-Y. Stress-wave-induced martensitic phase transformations in NiTi. SHOCK COMPRESSION OF CONDENSED MATTER-1999, vol. 505: AIP Publishing, 2000. p.267.

[149] Niemczura J, Ravi-Chandar K. Journal of the Mechanics and Physics of Solids 2006;54:2136.

[150] Chen Y-C, Lagoudas D. Journal of the Mechanics and Physics of Solids 2000;48:275.

[151] Bo Z, Lagoudas D. International Journal of Engineering Sciences 1999;37:1175.

[152] Bekker A, Jimenez-Victory JC, Popov P, Lagoudas DC. International Journal of Plasticity 2002;18:1447.

[153] Bekker A, Brinson L. Journal of the Mechanics and Physics of Solids 1997;45:949.

[154] Tanaka K. Journal of Pressure Vessel Technology(Transactions of the ASME) 1990;112:15

CHAPTER 3

ONE-DIMENSIONAL THERMOMECHANICAL MODEL FOR HIGH STRAIN RATE DEFORMATION OF AUSTENITIC SHAPE MEMORY ALLOYS

3.1 Abstract

Shape memory alloys (SMAs) exhibit the ability to absorb large dynamic loads and, therefore, are excellent candidates for structural components where impact loading is expected. While most models focus on the shape memory effect and/or pseudoelasticity of polycrystalline SMAs under quasi-static loading conditions; models for dynamic loading are limited. Many of the existing high strain rate models assume that the latent heat generated during deformation contributes to the change in the stress strain behavior during dynamic loading. The driving force for phase transformation is also related to the phase front velocity, which is not considered in exist models for the constitutive relationship of SMAs at high strain rate deformation. In this paper, the relationship between the driving force for phase transformation and phase front velocity is discussed. A new one-dimensional rate-dependent model is established for the dynamic loading behavior of SMAs.

3.2 Introduction

Shape memory alloys (SMAs) are widely used in aerospace, biomedical, and structural

---

This chapter is presented in its entirety from H. Yu and M.L. Young: "One-dimensional Thermomechanical Model for High Strain Rate Deformation of Austenitic Shape Memory Alloys", Journal of Alloys and Compounds, 710 (5) 858-868, July (2017) with permission from Elsevier

applications due either to pseudoelasticity or the shape memory effect, depending on their thermo-mechanical history [1-5]. NiTi-based SMAs are the most commercially successful and are readily available at the industrial scale. The most common NiTi-based SMAs include austenitic NiTi, martensitic NiTi, NiTiCu, NiTiNb, and NiTiFe; while other emerging binary and ternary NiTi-based are expected to become available depending on demand, cost, and processability [4]. Thermo-mechanical deformation and fracture behavior of these SMAs at quasi-static levels have been studied extensively [6-8]. Currently, there is a need for new materials for dynamic loading [9]. NiTi-based SMAs are promising as high strain rate materials because of their relatively large amounts of recoverable strain and high damping properties [10].

Experimental studies on the strain rate effect on the deformation behavior of NiTi SMAs have focused mainly on austenitic NiTi SMAs [10-14] and to a lesser extent on martensitic NiTi SMAs [15, 16]. The constitutive relationship of NiTi SMAs is strain rate sensitive. The effect of strain rate on transformation behavior in austenitic NiTi SMAs has been studied preliminarily [12, 14, 17, 18]. The flow stress in the transformation region increases with increasing strain rate. This phenomenon is attributed to the increase in temperature associated with deformation work and latent heat of phase transformation [18]. As strain rate increases, heat generated during deformation has less time to dissipate to the ambient through heat conduction, leading to a higher temperature within specimen, which stabilizes austenite. Therefore, a higher stress is needed for phase transformation. Although an increase in temperature during deformation has been widely used to explain the strain rate effect on the constitutive relationship of SMAs at quasi-static deformation, the temperature reaches a

saturation value at strain rates higher than 1.2×10^{-1}/s [18]. At the same time, heat conduction is insignificant at high strain rate deformation and the process is adiabatic. Limited temperature increasing at high strain rate deformation is observed in experiment [19, 20] and therefore self-heating can only partially be used to explain the large flow stress under high strain rate deformation. Nemat-Nasser et al [14] proposed a new mechanism for phase transformation in NiTi SMAs deformed at strain rate higher than a critical value. The kinetic relationship between the driving force for phase transformation and the speed of the phase boundary is studied [21, 22]. Niemczura and Ravi-Chandar [20] studied the propagation of phase boundaries of NiTi under quasi-dynamic conditions. They reported that the driving force for phase transformation is related to the speed of the propagation of the phase front.

Accurate modeling techniques potentially save not only time and money but also improve experimental design procedures. The modeling of NiTi SMAs can be classified into two groups: micromechanical and macroscopic phenomenological. The micromechanical models focus on the physical behavior of NiTi SMAs during deformation. The macroscale properties are related to such microscopic material features as transformation systems and phase boundaries. Representative models can be found in work [23-27]. Intensive computational consumption limits the use of micromechanical models for industrial application. Therefore, since macroscopic thermodynamic models improve the efficiency of computer calculation, martensitic phase transformation is represented by the change of martensitic phase fraction with macroscopic scalars such as transformation strain, irrecoverable deformation, stress and temperature. Transformation hardening is assumed to occur during phase transformation [28]. The representative models can be referred to as

Lagoudas' (Bo and Lagoudas [29], Lagoudas and Entchev [30], Lagoudas et al. [31], Hartl et al. [32]), Zaki's (Zaki [33-35], Zaki and Moumni [36, 37], Morin et al. [38, 39]), and Auricchio's [40, 41]. Similar models [42] have been developed by a combination of, alteration to, or permutation of these established models. Cisse et al. [43] presented a review paper on macroscopic models on shape memory alloys. While many rate-dependent models have been developed for quasi-static deformation of SMAs, only a few models have been developed for high strain rate deformation of SMAs. The relationship between the phase front velocity and strain rate during impact loading has been studied through different models. The constitutive relationship for dynamic deformation was assumed to be the same as that for quasi-static deformation in these models [28, 44-47]. Stress jump at the phase front was assumed to contribute to the large flow stress during phase transformation at high strain rate deformation. These models focus on localized microstructure of phase front, while the effect of strain rate on global stress-strain behavior is not well predicted. Some rate-dependent models [48, 49] have been established by a set of complicated mathematic equations to model the stress-strain behavior of SMA under fast loading conditions. The modeled stress-strain curve matches well with the experiment, while the physical mechanism is not well illustrated.

In this paper, we will present a one dimensional rate-dependent model that includes both latent heat and the kinetic relationship. The phase front velocity is incorporated into the constitutive relationship for SMA at high strain rate deformation for the first time in our model. The effect of dislocation on phase transformation during dynamic loading is considered and represented by 'transformation resistance due to dynamic loading' in our model. The phase transformation is assumed to be fully recovered and therefore the plastic

deformation in not included in present model. The paper is organized as follows: section 3.3 gives the background of high strain rate deformation and the traditional model for quasi-static deformation, section 3.4 presents a new constitutive theory by extending the thermodynamic formulation of traditional quasi-static deformation and the new term 'transformation resistance due to dynamic loading' is presented, section 3.5 shows a comparison of the results from the model with high strain rate experimental data and the influence of strain rate on stress strain curve is predicted, and section 3.6 presents our conclusions.

3.3 Background

3.3.1 Difference Between Quasi-static and High Strain Rate Deformation

The difference between high strain rate and quasi-static deformation is shown in Fig. 3.1. In wave theory, a material is composed of particles, and the stress strain behavior of the material is connected with wave velocity and particle velocities through wave functions [20]. In Fig. 3.1, the particles are represented by a set of solid balls. At high strain rate deformation, the particles are accelerated to velocity υ. According to the wave equations, local strain is related to particle velocity. Deformation is transferred by stress wave propagation through the sample with velocity C_0. The process is shown in Fig. 3.1(a) with global stress σ and global strain ε. Quasi-static deformation with the same stress σ is shown in Fig. 3.1(b). The particles marked by dark blue are compared with the particles at the same position during high strain rate deformation. During quasi-static loading, deformation is applied to the sample gradually, and extremely slowly. Unlike particles during high strain rate deformation, the particles remain static during quasi-static deformation. Therefore, strain is distributed

homogeneously throughout the sample. A similar discussion for the difference between quasi-static and high strain rate deformation is presented by Niemczura et al. [20].

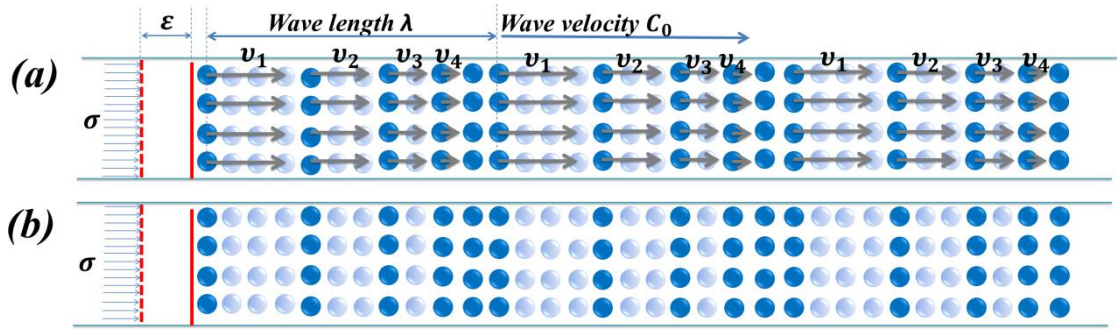

Fig.3.1 Schematic of the difference between (a) high strain rate and (b) quasi-static deformation

3.3.2 Constitutive Relationship for SMAs at Quasi-static Deformation

Our work is extended from the phenomenological model developed by Hartl et al. [32]. In this section, the three-dimensional quasi-static model is rewritten in one-dimensional form. The total Gibbs free energy is composed of the energy of the austenitic and martensitic phases and transformation energy caused by the interface energy between the two phases. These terms can be written as [32]:

$$\begin{cases} G_{A/M} = -\frac{\sigma^2}{2\rho_0 E} - \frac{1}{\rho_0}\sigma\alpha(T-T_0) - S(T-T_0) + C\left[(T-T_0) - TIn\left(\frac{T}{T_0}\right)\right] \\ G^{tr} = -\frac{1}{\rho_0}\sigma\varepsilon_{tr} + F(\xi) \end{cases} \tag{3.1}$$

respectively, where α is the thermal expansion coefficient of the material, S is the entropy of the material, C is the specific heat at a constant volume, and $F(\xi)$ is transformation hardening energy and is related to the martensitic volume fraction. The total Gibbs free energy is then written as:

$$G = (1-\xi)G_A + \xi G_M + G^{tr} = -\frac{1}{2\rho_0}\mathbb{S}(\xi)\sigma^2 - \frac{1}{\rho_0}\sigma\alpha(\xi)(T-T_0) + C(\xi)\left[(T-T_0) -\right.$$

$$TIn\left(\frac{T}{T_0}\right)\Big] - S(\xi)(T - T_0) - \frac{1}{\rho_0}\sigma\varepsilon_{tr} + F(\xi) \quad (3.2)$$

where the parameters in the above equations are defined as: $C(\xi) = C_A + \xi(C_M - C_A) = C_A + \xi\Delta C,\ S(\xi) = S_A + \xi(S_M - S_A) = S_A + \xi\Delta S$

Transformation strain ε_{tr} is related to the martensitic volume fraction ξ and the relationship is described as:

$$\dot{\varepsilon}_{tr} = g_{tr}\dot{\xi} \quad (3.3)$$

In this equation, g_{tr} is the transformation tensor, which determines the transformation strain direction and is defined as:

$$g_{tr} = \begin{cases} H\frac{\sigma}{|\sigma|};\ \dot{\xi} > 0 \\ H\frac{\varepsilon_{tr}}{|\varepsilon_{tr}|};\ \dot{\xi} < 0 \end{cases} \quad (3.4)$$

where *H* is the maximum transformation strain for the SMAs. The total strain is composed of elastic, thermal and transformation strain and can be written as:

$$\varepsilon = \varepsilon_e + \varepsilon_{th} + \varepsilon_{tr} \quad (3.5)$$

Therefore, the stress strain relationship can be written as:

$$\sigma = \mathbb{S}(\xi)^{-1}[\varepsilon - \varepsilon^{th} - \varepsilon^{tr}] = \mathbb{S}(\xi)^{-1}[\varepsilon - \alpha(\xi)(T - T_0) - g_{tr}\xi] \quad (3.6)$$

where $\mathbb{S}(\xi) = \frac{1}{E_A} + \xi\left(\frac{1}{E_M} - \frac{1}{E_A}\right) = \frac{1}{E_A} + \xi\Delta\mathbb{S},\ \alpha(\xi) = \alpha_A + \xi(\alpha_M - \alpha_A) = \alpha_A + \xi\Delta\alpha$ and α is the thermal expansion of the material.

According to second law of thermodynamics in the following form:

$$\sigma\dot{\varepsilon}_{tr} - \rho_0\frac{\partial G}{\partial\xi}\dot{\xi} = \pi_{tr}\dot{\xi} \geq 0 \quad (3.7)$$

where π_{tr} is the driving force for phase transformation and is solved as:

$$\pi_{tr} = g_{tr}\sigma + \frac{1}{2}\Delta\mathbb{S}\sigma^2 + \Delta\alpha\sigma(T - T_0) - \rho_0\Delta C\left[(T - T_0) - TIn\left(\frac{T}{T_0}\right)\right] + \rho_0\Delta S\xi(T - T_0) - f(\xi) \quad (3.8)$$

In the model, hardening energy related to the material properties is defined as $f(\xi)$ and

takes the following form [32]:

$$f(\xi)=\begin{cases}\frac{1}{2}a_1(1+\xi^{n_1}-(1-\xi)^{n_2})+a_3;\ \dot{\xi}>0\\ \frac{1}{2}a_2(1+\xi^{n_3}-(1-\xi)^{n_4})-a_3;\ \dot{\xi}<0\end{cases} \tag{3.9}$$

where $a_1=\rho_0\Delta S(M_f-M_s)$, $a_2=\rho_0\Delta S(A_s-A_f)$, and $a_3=-\frac{a_1}{4}\left(1+\frac{1}{n_1+1}-\frac{1}{n_2+1}\right)+\frac{a_2}{4}\left(1+\frac{1}{n_3+1}-\frac{1}{n_4+1}\right)$. $f(\xi)$ is related to the materials properties A_s (starting temperature for austenitic transformation), A_f (finishing temperature for austenitic transformation), M_s (starting temperature for martensitic transformation), and M_f (finishing temperature for martensitic transformation).

According to (3.7), the driving force $\pi_{tr}>0$ when $\dot{\xi}>0$ and $\pi_{tr}<0$ when $\dot{\xi}<0$. Therefore, the transformation function Φ is defined as:

$$\Phi=\begin{cases}\pi_{tr}-Y \text{ for } \dot{\xi}>0\\ -\pi_{tr}-Y \text{ for } \dot{\xi}<0\end{cases} \tag{3.10}$$

where Y is the critical barrier for the phase transformation and $Y=\frac{\rho_0\Delta S(M_s-A_f)}{2}-a_3$[32]. $\Phi\leq 0$ is satisfied during forward ($\dot{\xi}>0$) and reverse ($\dot{\xi}>0$) transformation

Based on the same model discussed above, Andani et al. [50] assumes that $\dot{\Phi}=0$ during phase transformation. Linear hardening is assumed during transformation and therefore, $n_1=n_2=n_3=n_4=1$. The martensitic volume fraction is expressed as [50]:

$$\dot{\xi}=\begin{cases}-\frac{(g_{tr}+\Delta\mathbb{S}\sigma)\dot{\sigma}+\rho_0\Delta S\dot{T}}{\rho_0\Delta S(M_s-M_f)};\ \dot{\xi}>0\\ -\frac{(g_{tr}+\Delta\mathbb{S}\sigma)\dot{\sigma}+\rho_0\Delta S\dot{T}}{\rho_0\Delta S(A_s-A_f)};\ \dot{\xi}<0\end{cases} \tag{3.11}$$

3.4 Constitutive Relationship for SMAs at High Strain Rate

3.4.1 Transformation Resistance due to Dynamic Loading f_D

The interface energy between austenite and martensite, the strain energy, and the energy

to overcome the shear resistance contribute to the resistance during martensitic phase transformation. Dislocation may be generated at the interface during high strain rate deformation, increasing flow stress during transformation. Therefore, in our work, transformation resistance f_D is assumed to represent the additional resistance during high strain rate deformation. For simplification, a linear relationship between f_D and martensitic volume fraction ξ is assumed and is expressed as:

$$f_D(\xi) = K\xi \tag{3.12}$$

where parameter K is related to strain rate and assumed to be constant when strain rate is given. Therefore, the driving force for phase transformation π_{tr} in equation (3.8) can be rewritten fort high strain rate deformation as:

$$\pi_{tr} = \Lambda\sigma + \frac{1}{2}\Delta\mathbb{S}\sigma^2 + \Delta\alpha\sigma(T - T_0) - \rho_0\Delta C\left[(T - T_0) - TIn\left(\frac{T}{T_0}\right)\right] + \rho_0\Delta S\xi(T - T_0) - f(\xi) - f_D(\xi) \tag{3.13}$$

where Λ is the transformation tensor at high strain rate deformation. The martensitic volume fraction is correspondingly rewritten as:

$$\dot{\xi} = \begin{cases} -\frac{(\Lambda + \Delta\mathbb{S}\sigma)\dot{\sigma} + \rho_0\Delta S\dot{T}}{\rho_0\Delta S(M_s - M_f) + K}; & \dot{\xi} > 0 \\ -\frac{(\Lambda + \Delta\mathbb{S}\sigma)\dot{\sigma} + \rho_0\Delta S\dot{T}}{\rho_0\Delta S(A_s - A_f) + K}; & \dot{\xi} < 0 \end{cases} \tag{3.14}$$

To calculate the transformation resistance f_D in equation (3.13), the driving force π_{tr} at high strain rate deformation should be solved by thermodynamic laws. The energy conservation at short time interval during deformation is expressed as:

$$\sigma\varepsilon + \rho_0 U + \frac{1}{2}\rho_0 v^2 = 0 \tag{3.15}$$

where the terms in the left side of equation stands for the strain energy, the internal energy, and the kinetic energy, respectively. The kinetic energy does not equal zero at high strain rate

deformation, which differs driving force π_{tr} for quasi-static and high strain rate deformation.

The kinetic energy during the phase transformation is assumed to be unrelated to the Young's modulus, temperature, and hardening function of the material. Therefore, to exclude the effect of thermal strain, the sample is assumed to be deformed under isothermal conditions. However, the isothermal assumption is more appropriate for quasi-static deformation, where kinetic energy is unimportant, than the dynamic deformation discussed here. For simplification, the assumption is made in this section and temperature increase due to heat transfer and latent heat generated during deformation will be considered in section 3.4.2. The semi-infinite length of the sample is assumed to exclude the effect of dissipation in the cross section and the effect of torsional wave propagation. Therefore, the whole procedure can be treated as a one-dimensional wave propagation in a semi-infinite rod during isothermal deformation. The boundary condition can be written as:

$$\upsilon(x,0)=0, \sigma(x,0)=0, \varepsilon(x,0)=0, \sigma(0,t)=\sigma_0, T=T_R \tag{3.16}$$

where $\upsilon(x,0), \sigma(x,0), \varepsilon(x,0)$ are the particle velocity, stress, and strain in the rod before deformation, respectively; $\sigma(0,t)$ is the stress applied on the impact end of the rod, which is assumed to be much higher than the transformation stress σ_{tr}.

According to equations (3.3) and (3.5), the total strain rate can be written as:

$$\dot{\varepsilon}=\dot{\varepsilon}_e+\dot{\varepsilon}_{tr}=\dot{\varepsilon}_e+g_{tr}\dot{\xi} \tag{3.17}$$

For a given material deformed at a given strain rate, the parameters $\rho_0\Delta S$, M_s, M_f, A_s, A_f, K, g_{tr}, and $\Delta\mathbb{S}$ in equation (3.11) are constant. According to the isothermal assumption, $\dot{T}=0$. $\dot{\sigma}$ is assumed to be a constant during deformation at a short time interval. We define $\sigma_{tr}=-\frac{g_{tr}}{\Delta\mathbb{S}}$ and $R=-\frac{\rho_0\Delta S(M_s-M_f)+K}{g_{tr}\dot{\sigma}\Delta\mathbb{S}}$ for forward transformation or $R=-\frac{\rho_0\Delta S(A_s-A_f)+K}{g_{tr}\dot{\sigma}\Delta\mathbb{S}}$

for reverse transformation, and then equation (3.17) can be rewritten as

$$\dot{\varepsilon} = \frac{\dot{\sigma}}{E} + \frac{\sigma - \sigma_{tr}}{R} \tag{3.18}$$

which is similar to the constitutive relationship of Maxwellian rate-type viscosity and has been selected as the constitutive relationship of SMA under high strain rate deformation by Faciu et al. [51]. Similar formula can be concluded from the other method (Appendix). The change of Young's modulus E due to the martensitic transformation in a small time interval is insignificant. Therefore, E is related to the wave velocity C_0 as $E = \rho_0 C_0^2$. To solve the wave structure in the material, the governing equations from one-dimensional wave theory should be added to equation (3.18):

$$\begin{cases} \frac{\partial v}{\partial x} = \frac{\partial \varepsilon}{\partial t} \\ \rho_0 \frac{\partial v}{\partial t} = \frac{\partial \sigma}{\partial x} \\ \frac{\partial \varepsilon}{\partial t} = \frac{1}{E}\frac{\partial \sigma}{\partial t} + \frac{\sigma - \sigma_{tr}}{R} \end{cases} \tag{3.19}$$

Characteristic methods [45] are applied to solve the partial differential equations (3.19). The simple wave relationship ($\sigma = -\rho_0 C_0 v$ and $v = -C_0 \varepsilon$) can be applied to satisfy the deformation in the wave front ($x = -C_0 t$). The stress in the wave front is then solved as:

$$\sigma = \sigma_{tr} + (\sigma_0 - \sigma_{tr}) exp\left(-\frac{\rho_0 C_0}{2R} x\right) \quad \text{when} \quad x = -C_0 t \tag{3.20}$$

According to equation (3.20), the stress $\sigma = \sigma_0$ when $x = 0$ and $\sigma = \sigma_{tr}$ when $x = +\infty$. By adding equation (3.20) into equation (3.18), a high strain rate deformation region is observed at $x \to 0$. Therefore, for high strain rate deformation, equation (3.20) can be simplified as:

$$\sigma = \sigma_0 - \frac{\rho_0 C_0 g_{tr} \dot{\xi}}{2} \quad \text{when} \quad x = -C_0 t \tag{3.21}$$

The above solution for the stress is limited to the wave front. The deformation at any time and position *(x, t)* can be solved by characteristic methods in the same way with boundary

conditions solved by (3.21) as:

$$\begin{cases} \sigma(x,t) = \sigma_0 - \frac{1}{2} g_{tr} \dot{\xi} \rho_0 C_0 x \\ \varepsilon(x,t) = \frac{\sigma_0}{E} + g_{tr} \dot{\xi} t - \frac{3 g_{tr} \dot{\xi} x}{2 C_0} \\ v(x,t) = v_0 + g_{tr} \dot{\xi} x - \frac{1}{2} g_{tr} \dot{\xi} C_0 t \end{cases} \tag{3.22}$$

According to the above assumptions, the deformation at high strain rate (region $x \to 0$) is taken into consideration. Therefore, equation (3.22) is simplified as:

$$\begin{cases} \sigma = \sigma_0 \\ \varepsilon = \frac{\sigma_0}{E} + g_{tr} \dot{\xi} t = \frac{\sigma_0}{E} + g_{tr} \xi \\ v = v_0 - \frac{1}{2} g_{tr} \dot{\xi} C_0 t = v_0 - \frac{1}{2} g_{tr} C_0 \xi \end{cases} \tag{3.23}$$

According to equation (3.23), the stress during phase transformation remains constant at σ_0, which is the same as predicted by Niemczura and Ravi-Chandar [20]. The deformation path related to equation (3.23) is shown in Fig. 3.2a. When stress σ_0 is applied on the impact end of the sample, the elastic stress wave is first generated to deform the sample to strain $\varepsilon_0 = \frac{\sigma_0}{E}$. The corresponding particle velocity at the same time is v_0. Phase transformation is activated when stress σ_0 is larger than the critical stress σ_{tr}. The speed of the phase front is the same as the wave velocity C_0. During phase transformation, strain increases and particle velocity decreases with the nucleation and growth of martensite. Thermodynamic equilibrium is satisfied when the strain is equal to ε_0^{real}. Flow stress remains constant during phase transformation. Therefore, kinetic energy ϕ_k during phase transformation is:

$$\phi_k = \frac{1}{2} \rho_0 v^2 = \frac{1}{2} \rho_0 v_0^2 + \frac{1}{8} \rho_0 g_{tr}^2 C_0^2 \xi^2 - \frac{1}{2} \rho_0 g_{tr} C_0 v_0 \xi \tag{3.24}$$

According to equation (3.24), kinetic energy during high strain rate deformation is related to particle velocity v_0, wave velocity C_0, and martensitic volume fraction ξ. The speed of the phase front is assumed to be the same as the wave velocity. This assumption is reasonable for deformation at extremely high strain rate. When the sample is deformed at moderate to high

strain rate, the speed of the phase boundary is lower than the acoustic speed. Kinetic energy is related to the speed of the phase front.

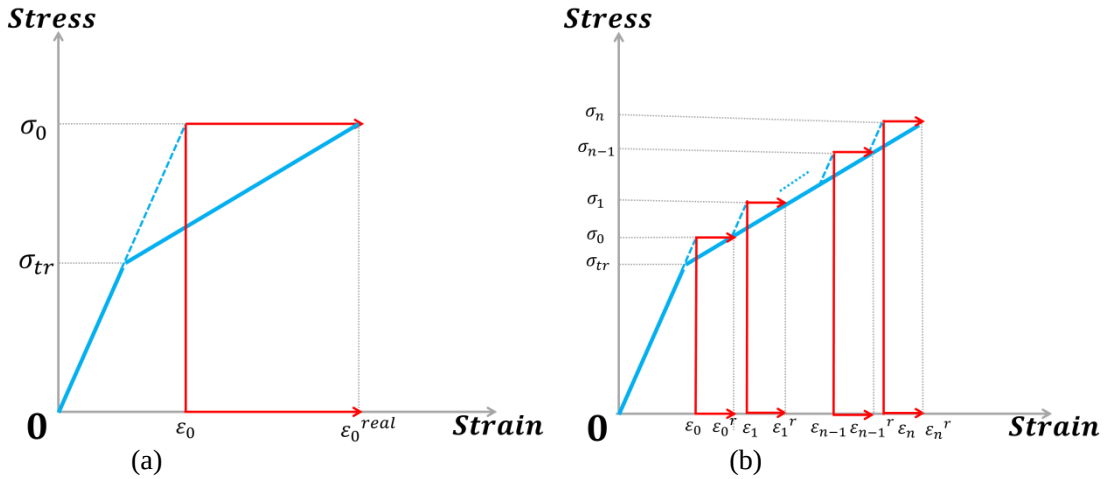

Fig.3.2 Schematic of (a) the deformation path in impact loading when $C_P = C_0$ (b) the deformation path in impact loading when $C_P \neq C_0$

When the speed of the phase boundary is no longer equivalent to the elastic wave, the phase transformation during high strain rate deformation propagates at the speed of C_P. The deformation is shown in the schematic in Fig. 3.3. The new martensitic transformation zone is generated in the pre-deformed region as illustrated in Fig. 3.3. The martensitic volume fraction of the pre-deformed and newly generated zone is ξ_{n-1} and ξ_n, respectively. The strain and stress of the two zones is ε_{n-1}, ε_n and σ_{n-1}, σ_n, respectively. During propagation of the phase boundary, jump discontinuities are observed across the phase front [20, 45]. The relationship between stress and strain is given as:

$$\begin{cases} [v] = -C_P[\varepsilon] \\ [\sigma] = -\rho_0 C_P[v] \end{cases} \tag{3.25}$$

where [] stands for the difference of the quantity across the phase front. The stress evolution during the deformation can be seen as a sequence of microscopic jumps shown in Fig. 3.2b. We assume the simple wave relationship can be applied to the phase front in each microscopic jump. Comparing equation (3.25) with the simple relationship mentioned in

section 3.4.1, kinetic energy under moderate and high strain rate can be written as:

$$\phi_k = \frac{1}{2}\rho_0 v^2 = \frac{1}{2}\rho_0 v_0^2 + \frac{1}{8}\rho_0 g_{tr}^2 C_P^2 \xi^2 - \frac{1}{2}\rho_0 g_{tr} C_P v_0 \xi \tag{3.26}$$

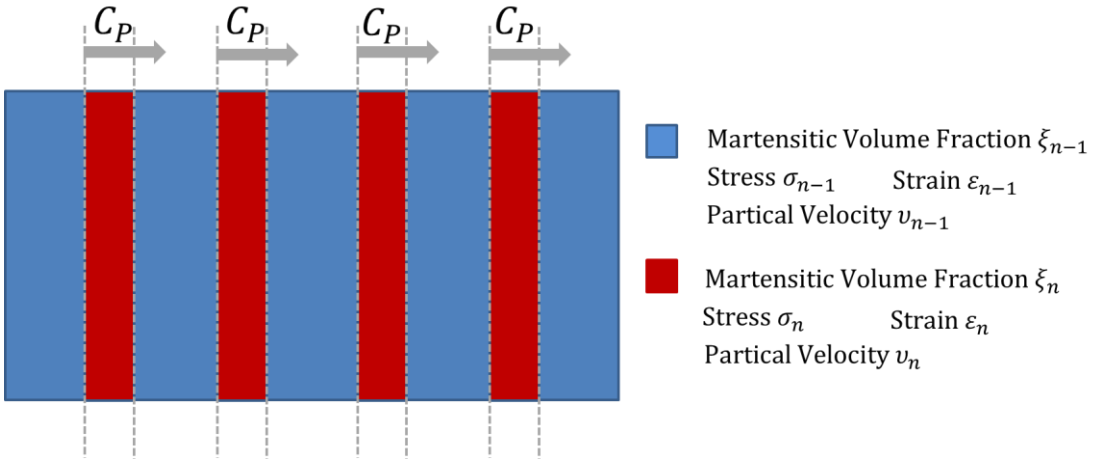

Fig.3.3 Schematic of phase transformation in representative volume element (RVE)

In order to derivate the resistance $f_D(\xi)$, the thermodynamic relationship is established in a small representative volume element (RVE) with a cross sectional area of A_0. According to thermodynamic law, work done by flow stress leads to a change of internal energy and kinetic energy of the material. The relationship in equation (3.15) is rewritten as:

$$\sigma v + \rho_0 C_P U + C_P \phi_k = 0 \tag{3.27}$$

Internal energy U, Gibbs free energy G, and entropy S of the system are related by the first law of thermodynamics as:

$$U = G + TS - \frac{1}{\rho_0}\sigma\varepsilon \tag{3.28}$$

Dissipation of the system is given by the second law of thermodynamics in the form of Clausius-Planck inequality as:

$$\rho_0 \frac{\partial S}{\partial t} \geq 0 \tag{3.29}$$

Combining equations (3.2), (3.27)-(3.29), we find the following equations:

$$\rho_0\left(S+\frac{\partial G}{\partial T}\right)\dot{T}+\left[g_{tr}\sigma+\frac{1}{2}\Delta\mathbb{S}\sigma^2+\Delta\alpha\sigma(T-T_0)-\rho_0\Delta C\left[(T-T_0)-TIn\left(\frac{T}{T_0}\right)\right]+\right.$$

$$\left.\rho_0\Delta S\xi(T-T_0)-\frac{1}{4}\rho_0C_P^2g_{tr}^2\xi+\frac{1}{2}\rho_0g_{tr}C_Pv_0-f(\xi)\right]\dot{\xi}\geq 0 \qquad (3.30)$$

Equation (3.30) is a required condition for all temperatures and martensitic volume fractions to be satisfied. The term $\rho_0\left(S+\frac{\partial G}{\partial T}\right)\dot{T}$ stands for entropy dissipation and the term $\left[g_{tr}\sigma+\frac{1}{2}\Delta\mathbb{S}\sigma^2+\Delta\alpha\sigma(T-T_0)-\rho_0\Delta C\left[(T-T_0)-TIn\left(\frac{T}{T_0}\right)\right]+\rho_0\Delta S\xi(T-T_0)-\right.$ $\left.\frac{1}{4}\rho_0C_P^2g_{tr}^2\xi+\frac{1}{2}\rho_0g_{tr}C_Pv_0-f(\xi)\right]\dot{\xi}$stands for phase transformation. Therefore, the driving force for phase transformation π_{tr} can be written as:

$$\pi_{tr}=\frac{1}{2}g_{tr}\sigma+\frac{1}{2}\Delta\mathbb{S}\sigma^2+\Delta\alpha\sigma(T-T_0)-\rho_0\Delta C\left[(T-T_0)-TIn\left(\frac{T}{T_0}\right)\right]+\rho_0\Delta S\xi(T-T_0)-$$

$$\frac{1}{4}\rho_0C_P^2g_{tr}^2\xi-f(\xi) \qquad (3.31)$$

According to equation (3.13) and (3.31), $\Lambda=\frac{1}{2}g_{tr}$ and transformation resistance due to dynamic loading $f_D(\xi)$ is expressed as:

$$f_D(\xi)=K\xi=\frac{1}{4}\rho_0C_P^2g_{tr}^2\xi \qquad (3.32)$$

The speed of phase boundary is related to the deformation rate in the work of Niemczura and Ravi-Chandar [20] as $\dot{s}(\gamma^--\gamma^+)=\dot{\delta}$, where $\dot{s}$ is the speed of the phase boundary, $\dot{\delta}$ is the extension rate at the end of the bar, and γ^- and γ^+ are the strain behind and ahead of the moving phase boundary, respectively. We assume the value $\gamma^--\gamma^+$ is constant during high strain rate deformation. The relationship between strain rate and the speed of the phase boundary is

$$C_P=\kappa\dot{\varepsilon} \qquad (3.33)$$

The material parameter κ describes the influence of strain rate to phase boundary velocity, which is to be determined experimentally by iteration. According to equation (3.32) and (3.33), *K* is related to κ as:

$$K = \frac{1}{4}\rho_0 \kappa^2 g_{tr}^2 (\dot{\varepsilon})^2 \tag{3.34}$$

As we mentioned before, parameter K describe the effect of dislocation on phase transformation at high strain rate deformation. K is related to strain rate $\dot{\varepsilon}$ by power law equation in equation (3.34). According to the assumption we made at the beginning of this section, K is unrelated to the material properties and is constant when strain rate is given. Therefore, κ is constant for all the austenitic SMAs in our model.

The relationship between the martensitic volume fraction rate and the transformation function is proposed by Qidwai et al. [52] for three-dimensional models. The relationship is therefore rewritten in one-dimensional form for the present model as:

$$\dot{\xi} = \frac{\Phi}{\pm \mathbb{S}\left(\frac{\partial \Phi}{\partial \sigma}\right)^2 - \frac{\partial \Phi}{\partial \xi}} \tag{3.35}$$

When the form of Φ is taken into equation (3.35), the martensitic volume fraction rate during forward transformation is solved as:

$$\dot{\xi} = \frac{\frac{1}{2}g_{tr}\sigma + \frac{1}{2}\Delta\mathbb{S}\sigma^2 + \Delta\alpha\sigma(T-T_0) - \rho_0\Delta C\left[(T-T_0) - TIn\left(\frac{T}{T_0}\right)\right] + \rho_0\Delta S\xi(T-T_0) - \frac{1}{4}\rho_0 C_P^2 g_{tr}^2 \xi - \frac{1}{2}a_1(1+\xi^{n_1} - (1-\xi)^{n_2}) - \frac{\rho_0\Delta S\left(M_S - A_f\right)}{2}}{\mathbb{S}\left[\Delta\mathbb{S}\sigma + \Delta\alpha(T-T_0) + \frac{1}{2}g_{tr}\right]^2 - \rho_0\Delta S(T-T_0) + \frac{1}{4}\rho_0 C_P^2 g_{tr}^2 + \frac{1}{2}a_1(n_1\xi^{n_1-1} + n_2(1-\xi)^{n_2-1})} \tag{3.36}$$

3.4.2 Temperature Increase during High Strain Rate Deformation

Temperature increase by heat transfer is discussed in this section. The heat transfer equation for SMA could be written as [50]:

$$\rho_0 C\frac{\partial T}{\partial t} = P + hA(T - T_0) + \rho_0 \Delta Q\frac{\partial \xi}{\partial t} \tag{3.37}$$

where P, h, A are the dissipated power, heat convection coefficient, the area of the sample, respectively. ParameterΔQ is the latent heat generated during transformation. Our work focus

on the one dimensional model of SMAs deformed at strain rate higher than 100/s. The process is adiabatic and the term related to heat conduction equals zero. Therefore, *h*=0. According to energy conservation,

$$\rho_0 \frac{\partial U}{\partial t} + \frac{1}{2}\rho_0 \frac{\partial v^2}{\partial t} = -\sigma \frac{\partial \varepsilon}{\partial t} \tag{3.38}$$

From the definition of Gibbs free energy in the rate-dependent model, *G* is related to the stress, strain, temperature, and volume fraction of the martensitic phase:

$$\rho_0 \frac{\partial U}{\partial t} = \rho_0 \frac{\partial G}{\partial \varepsilon}\frac{\partial \varepsilon}{\partial t} + \rho_0 \frac{\partial G}{\partial \sigma}\frac{\partial \sigma}{\partial t} + \rho_0 \frac{\partial G}{\partial \xi}\frac{\partial \xi}{\partial t} + \rho_0 \frac{\partial G}{\partial T}\frac{\partial T}{\partial t} + \rho_0 T \frac{\partial S}{\partial t} + \rho_0 S \frac{\partial T}{\partial t} - \varepsilon \frac{\partial \sigma}{\partial t} - \sigma \frac{\partial \varepsilon}{\partial t} \tag{3.39}$$

and

$$S = -\frac{\partial G}{\partial T} = \frac{1}{\rho_0}\alpha(\xi)(T - T_0) + C(\xi) In\left(\frac{T}{T_0}\right) + S(\xi),\ \ \varepsilon = \rho_0 \frac{\partial G}{\partial \sigma},\ \ \sigma = \rho_0 \frac{\partial G}{\partial \varepsilon} \tag{3.40}$$

Substituting equation (3.40) into (3.39), the equation can be simplified to:

$$\rho_0 T \frac{\partial S}{\partial t} = \pi_{tr} \frac{\partial \xi}{\partial t} \tag{3.41}$$

Thus, equation (3.41) has the same form as that in the rate-independent model [46]. The only difference is the definition of π_{tr}. In the rate-independent model, π_{tr} is determined by the applied stress, temperature, and volume fraction of the martensitic phase. The strain rate effect is not shown in these models. We incorporate the formula of entropy in equation (3.40) into equation (3.41). Since the specific heat for the austenitic and martensitic phases are the same, $C(\xi) = C$ and equation (41) can be rewritten as:

$$\rho_0 C \frac{\partial T}{\partial t} = (\pi_{tr} - \rho_0 T \Delta S)\frac{\partial \xi}{\partial t} - T \frac{\partial \alpha(\xi)\sigma}{\partial t} \tag{3.42}$$

The heat transfer equation is concluded in equation (3.42). The latent heat generated during transformation equals $\pi_{tr} - \rho_0 T \Delta S$ and the dissipated power equals $T \frac{\partial \alpha(\xi)\sigma}{\partial t}$.

According to experimental results [53] and [54], we find that $\pi_{tr} \ll \rho_0 T \Delta S$ for NiTi SMAs. Equation (3.42) can be simplified to:

$$\rho_0 C \frac{\partial T}{\partial t} = -T \frac{\partial}{\partial t}(\rho_0 \Delta S \xi + \alpha(\xi)\sigma) \tag{3.43}$$

and equation (3.43) can be solved as:

$$T = T_0 \exp[-\frac{1}{\rho_0 C}(\rho_0 \Delta S \xi + \alpha(\xi)\sigma)] \tag{3.44}$$

The temperature solved in equation (3.44) has the same form as that in the rate-independent model [46]. For both the rate-independent and rate-dependent models, the basic assumption is the same: heat transfer is neglected in both models. The change in temperature caused by the deformation work then has the same form. According to equation (3.44), the temperature increase is related to thermal expansion and the change in entropy of the material. By replacing the T in the driving force π_{tr} with equation (3.44), we can obtain a model for the high strain rate deformation in the adiabatic case.

3.5 Comparison of the Model with Experimental Results

3.5.1 Parameters for the Model

This paper presents a new model by adding a kinetic relation to the traditional thermodynamic model to simulate the deformation of SMAs at high strain rate. The driving force for phase transformation is related to the speed of the phase boundary C_P;. when that speed is 0, the present model will be the same as the traditional models for quasi-static deformation discussed in section 3.4.1. Both models are compared in Table 3.1. To solve the proposed model established in the previous section requires several parameters. According to equation (3.6), the following terms (Young's moduli of austenitic and martensitic phases E_A and E_M, respectively, thermal expansion of austenitic and martensitic phases α_A and α_M, respectively, and martensitic volume fraction ξ) are needed to relate strain to stress. The

martensitic volume fraction ξ is related to the driving force π_{tr} in equation (3.28). According to equations (3.9,31,32), driving force π_{tr} is related to density ρ_0, specific heat of austenitic and martensitic phases C_A and C_M, respectively; speed of phase boundary C_P, maximum recoverable strain H; and the start and finish temperatures for austenitic and martensitic phase transformation A_s, A_f, M_s, and M_f, respectively. The maximum recoverable strain H is experimentally determined as 7%. The phase transformation temperatures are also experimentally determined to be $A_s = 288K$, $A_f = 302K$, $M_s = 277K$, and $M_f = 252K$ for a NiTi SMA with a composition of 50.8 at.%Ni-49.2 at.%Ti, commonly referred to as SE508,. The strain rate sensitivity parameter κ is selected by iteration to be 0.73, based on experimental results. The other material properties selected are the same as that in Hartl et al. [32]. Material parameters are listed in Table 3.2. The Young's modulus of austenitic phase and martensitic phase are selected as 32 GPa and 57 GPa, respectively. Although the Young's modulus for the austenitic phase is 70 GPa, the inaccuracy for the experiment in small strain in the Kolsky compression bar will lead to a Young's modulus of around 40 GPa for most experiments [12]. For high strain rate deformation on Kolsky compression bar, one dimensional equilibrium is assumed during deformation. The effect of the dispersion in the cross section and the torsional wave is ignored. The Young's modulus is underestimated in the experiment on Kolsky bar. In our one dimensional phenomenological model, the influence of the dispersion in the cross section and the torsional wave on the transformation strain is calibrated by the selection of κ in our model

Table 3.1 Comparison of new model and traditional model

Model	New Model	Traditional Model
Driving force	$\pi_{tr} = \frac{1}{2} g_{tr}\sigma + \frac{1}{2}\Delta\mathbb{S}\sigma^2 + \Delta\alpha\sigma(T - T_0) - \rho_0\Delta C\left[(T - T_0) - TIn\left(\frac{T}{T_0}\right)\right] + \rho_0\Delta S\xi(T - T_0) - \frac{1}{4}\rho_0 C_P^2 g_{tr}^2\xi - f(\xi)$	$\pi_{tr} = g_{tr}\sigma + \frac{1}{2}\Delta\mathbb{S}\sigma^2 + \Delta\alpha\sigma(T - T_0) - \rho_0\Delta C\left[(T - T_0) - TIn\left(\frac{T}{T_0}\right)\right] + \rho_0\Delta S\xi(T - T_0) - f(\xi)$
Evolution equation	$g_{tr} = \begin{cases} H\frac{\sigma}{\lvert\sigma\rvert}; & \dot{\xi} > 0 \\ H\frac{\varepsilon_{tr}}{\lvert\varepsilon_{tr}\rvert}; & \dot{\xi} < 0 \end{cases}$	$g_{tr} = \begin{cases} H\frac{\sigma}{\lvert\sigma\rvert}; & \dot{\xi} > 0 \\ H\frac{\varepsilon_{tr}}{\lvert\varepsilon_{tr}\rvert}; & \dot{\xi} < 0 \end{cases}$
Hardening energy	$f_D(\xi) + f_M(\xi)$	$f_M(\xi)$
Temperature increase	$T = T_0\exp[-\frac{1}{\rho_0 C}(\rho_0\Delta S\xi + \alpha(\xi)\sigma)]$	Preassumed 50K for high strain rate deformation [45]
Mechanism for large stress increase during phase transformation	Microscopic stress jump across the phase boundary and dynamic hardening	Global stress jump [45]

Table 3.2 Parameters for current model

Elastic modulus of austenite E_A	*32 GPa*	Austenitic finish temperature A_f	*302 K*
Elastic modulus of martensite E_M	*57 GPa*	Density ρ_0	*6450.0 kg/m^3*
Thermal expansion coefficient for austenite α_A	*2.8 ×10^{-5} K^{-1}*	Specific heat *C*	*329 J/kg ℃*
Thermal expansion coefficient for martensite α_M	*2.8 ×10^{-5} K^{-1}*	Strain rate sensitive parameter K	*0.73*
Martensitic start temperature M_S	*252 K*	Stress influence coefficient $\rho_0\Delta S$	*-0.35 MPaK^{-1}*
Martensitic finish temperature M_f	*277 K*	n_1,n_2,n_3,n_4	*0.30, 0.10, 0.20, 0.25*
Austenitic start temperature A_S	*288 K*	Reference temperature T_0	*300 K*

Experimental work performed by Guo et al. [56] is used for calibration. In Guo et al. [56], experimental data from dynamic deformation using Kolsky compression bar of an austenitic NiTi SMAs with 50.8 at.% Ni from Nitinol Devices and Components (NDC) is presented. A pulse shaper is used to achieve constant strain rate during high strain rate deformation. The stress strain curve for deformation at 2500/s is selected for calibration and

is shown as the light blue curve in Fig. 3.4. Stress strain curves modeled by current and traditional models are shown in red and blue dashed lines, respectively.

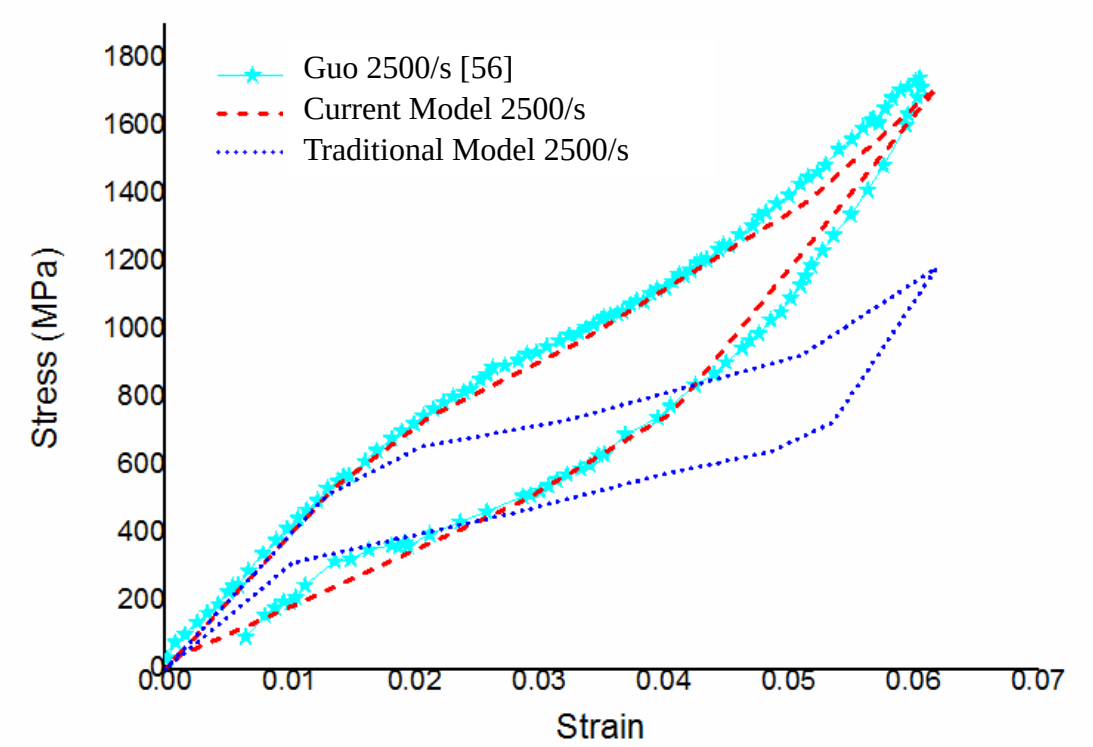

Fig.3.4 Comparison of the experimental result [56], with current model and traditional model at strain rate 2500/s

According to Fig. 3.4, the stress strain curve simulated by the current model matches well with the experimental result. The starting stress for phase transformation occurs at about 600 MPa experimentally and is also observed in the current and traditional models. The maximim stress occurs at a strain of ~6%, and the value is about 1700 MPa experimentally and in current models. The maximun stress in the traditional model is only 1100 MPa. During the unloading process, elastic recovery of the martensitic phase is observed until the stress value is about 700 MPa, which is the same experimentally and in the two models. Reverse transformation is activated when the stress is lower than 700 MPa. The error can be calculated by $e\% = \left|\frac{\sigma_{mod}-\sigma_{exp}}{\sigma_{exp}}\right|$. The stress at a strain of 3% is taken into consideration. The experimental stress is about 920 MPa, while the predicted values for the current model and

traditional model are 900 MPa and 700 MPa, respectively. The error associated with the current model and the traditional model is 0.02 and 0.22, respectively. Therefore, the current model better predicts stree value as compared to the traditional model.

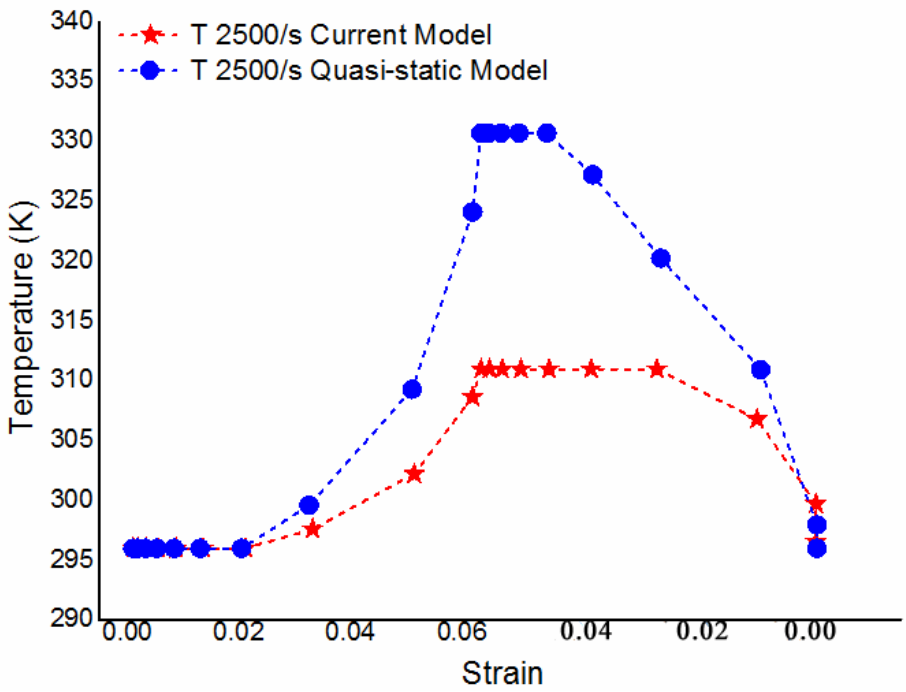

Fig.3.5 Prediction of temperature in current model and traditional model

In the experiment, the sample is deformed at 296 K; the same ambient temperature is assumed in the model. Change of temperature during deformation is shown in Fig. 3.5. Predictively, the temperature remains the same as the ambient temperature during elastic deformation of the material. When phase transformation is activated at strains larger than 2%, the temperature gradually increases with strain. The maximum temperature occurs at a strain of 6%, and the temperature value is 310 K in the current model and 331 K in the traditional model. The maximum temperature is maintained until unloading to a strain of 3% for the current model and 4% for the traditional model. The temperature decreases rapidly as the strain approaches zero. After the strain is fully recovered, the temperature returns to the ambient temperature of 296 K. The maximum increase of temperature is 35 K in the

traditonal model, while it is only 15 K in the current model. The prediction of temperature increase matches well with the experimental data during high strain rate deformation [19, 55]. Therefore, the current model is predictive of deformation behavior at high strain rate.

3.5.2 Stress Strain Relationship at Different Strain Rates

Dynamic deformation of austenitic NiTi SMAs at various high strain rates have been studied experimentally by Guo et al [56]. Stress strain curves from experimental data and from the current model are compared in Fig. 3.6. Simulated results match well with the experimental data.

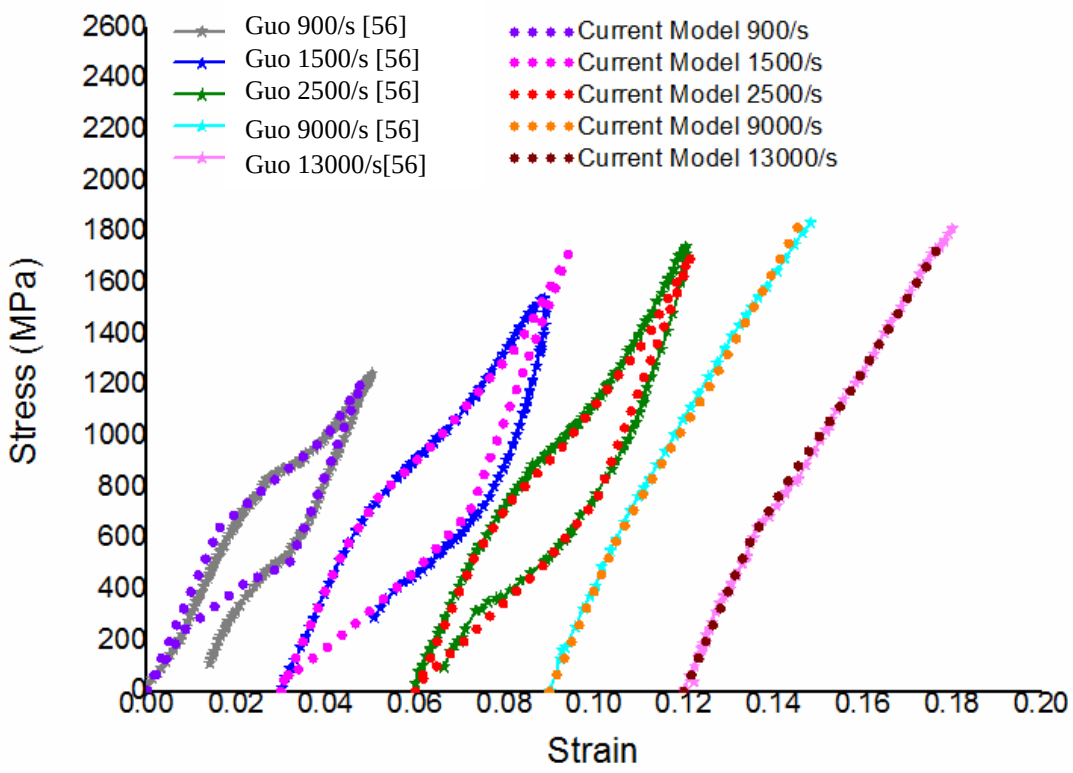

Fig.3.6 Stress strain curves at different strain rates

According to Fig. 3.6, the starting stress for forward phase transformation increases with strain rate. Similar to the forward transformation, the starting stress for reverse transformation also increases with strain rate. Note that a nearly linear stress strain relationship occurs at

strain rates higher than 9000/s. This phenomenon is observed experimentally and is simulated in the current model. The influence of strain rate on the hardening effect during phase transformation is also shown in Fig. 3.6. The hardening effect is determined as $d\sigma/d\varepsilon$ during phase transformation. From the experiment and the model, $d\sigma/d\varepsilon$ increases from 10 GPa to 20 GPa when strain rate increases from 900/s to 2500/s. At strain rates higher than 9000/s, $d\sigma/d\varepsilon$ approaches the elastic modulus of the material.

The previous section compares simulated results from the current model with experiment results of Guo et al. [56] The current model can also be applied to the deformation of other austenitic SMAs. Nemat-Nasser et al. [14] experimentally studied the high strain rate behavior of austenitic SMAs with composition 50.4 at.% Ni-49.6 at.% Ti at strain rate ranges from 330/s to 1080/s. To simulate the high strain rate behavior of the material requires phase transformation temperatures A_s, A_f, M_s, and M_f, which are not listed. In the present model, the hardening energy $f_M(\xi)$ is related to phase transformation temperatures, and we define hardening energy as $mf_M(\xi)$ and $nf_M(\xi)$ for forward and reverse transformation, respectively. *m* in the equation is calibrated by the stress strain curve during forward transformation and *n* is calibrated by the stress strain curve in reverse transformation. In the present model, the parameters *m* and *n* are calibrated by the stress strain curve for strain rate 1080/s, and *m=2* and *n=1.5* are calibrated for the experiment. Calibration of the model to the experimental data is shown in Fig. 3.7. The parameters *m* and *n* are then taken into the model to illustrate stress strain behavior under different strain rates. Young's moduli of the austenitic and martensitic phases are experimentally determined to be 35 GPa and 30 GPa, respectively, for the material in Nemat-Nasser et al. [14]. The strain rate

sensitivity parameter κ is constant for all the austenitic SMAs as 0.73. Current model results are compared with the experimental data in Fig. 3.8.

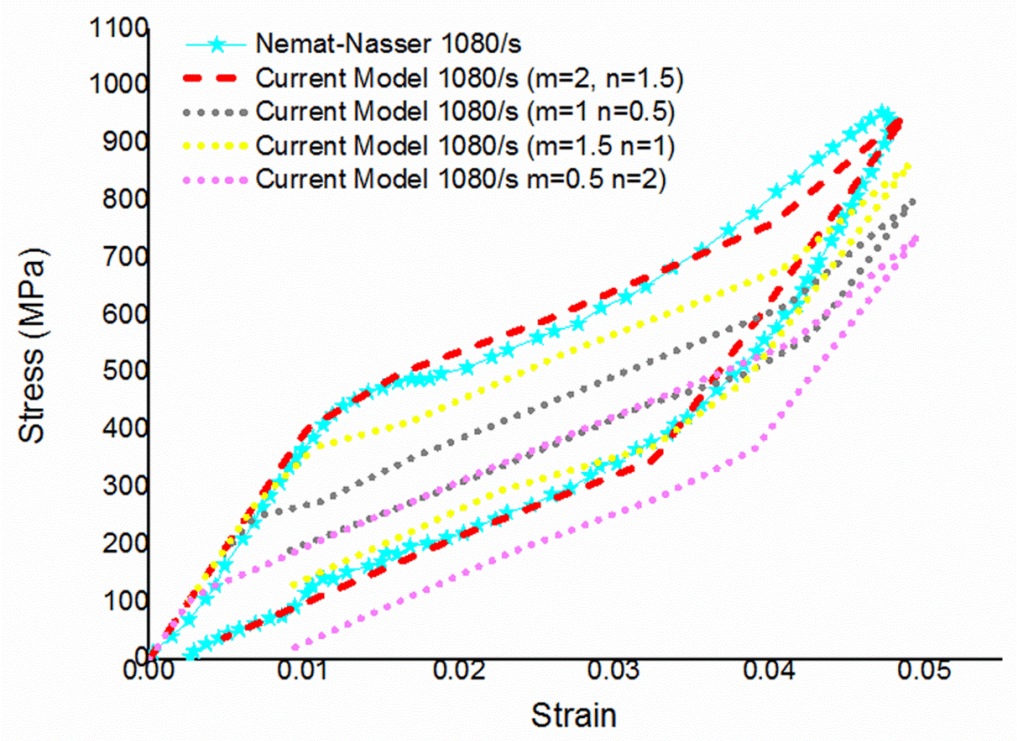

Fig.3.7 Calibration of the model with experimental data [14]

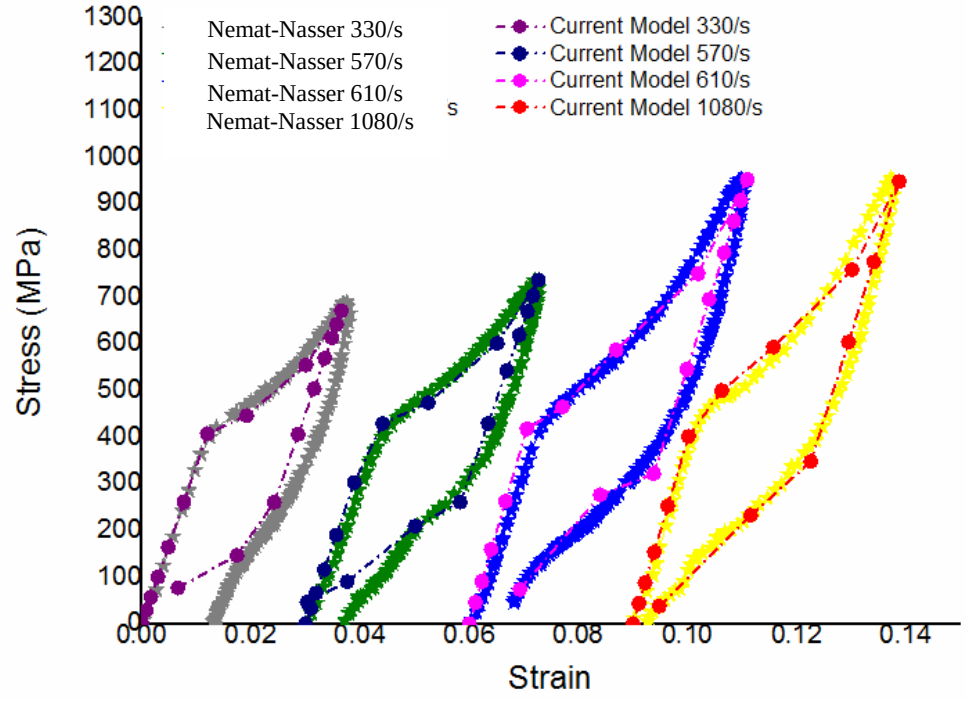

Fig.3.8 Comparison of the model with experimental data [14]

3.5.3 Deformation at Different Loading and Unloading Strain Rates

In the previous sections, strain rates during loading and unloading conditions were assumed to be equivalent. During actual deformation, strain rates for loading and unloading conditions are not necessarily equivalent. Nemat-Nasser and Guo [55] experimentally studied the effect of different strain rates in loading and unloading conditions at room temperature (296K). The material selected in the experiment is the same as that in the previous experiment. Therefore, the parameters for modeling are the same as those for the previous experiment. The experimental and simulated results are shown in Fig. 3.9. Loading strain rates range from 440/s to 2100/s and unloading strain rates range from 330/s to 400/s. According to Fig. 3.8, the change of slope $d\sigma/d\varepsilon$ with strain rate during the loading process follows the same trend as that discussed in section 3.5.2. The slope $d\sigma/d\varepsilon$ is almost the same during unloading. By comparing the stress strain curve at strain rate 1500/s in Figs. 3.6 and 3.9, we find that the hysteresis area increases with the decrease of unloading strain rate. We can also conclude that the change of parameters in model to account for different strain rates in unloading does not change the prediction for the loading part. Therefore, loading and unloading deformation at high strain rate can be seen as independent processes.

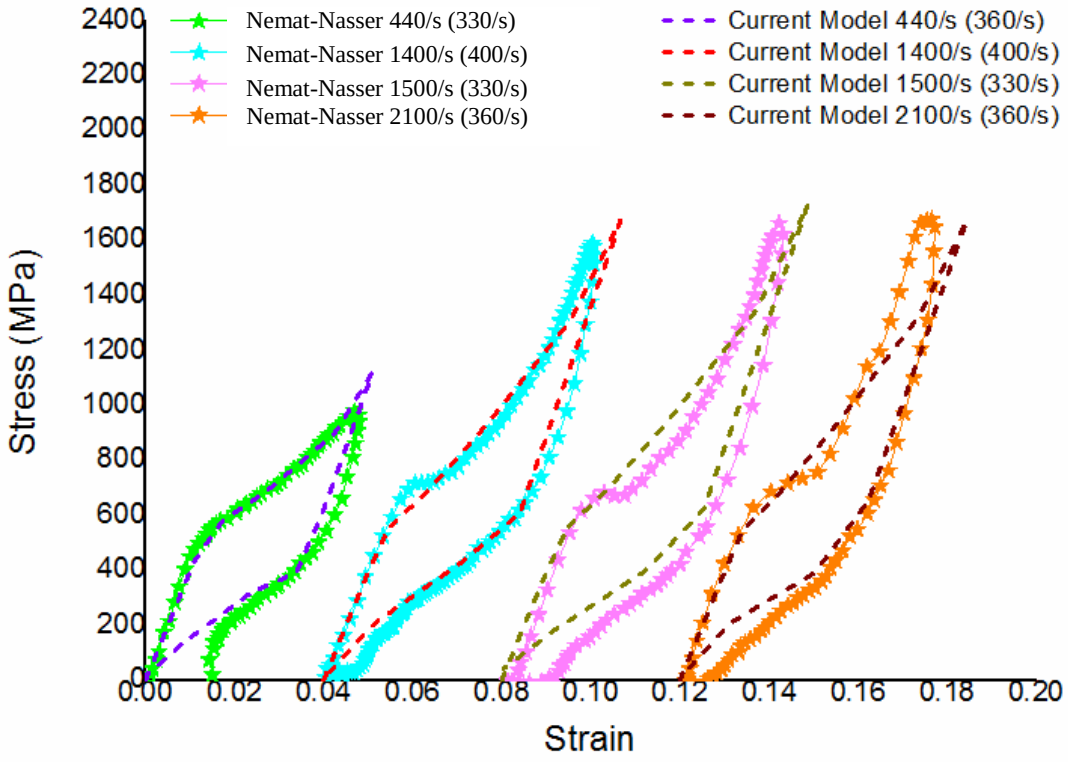

Fig.3.9 Comparison of the model with experimental data [55] for deformation under different loading and unloading rates

3.5.4 Influence of Strain Rate on Temperature Increase

The stress strain curve under different hign strain rate deformation is predicted in Fig. 3.10. The material is assumed to be the same as that of Nemat-Nasser et al. [14], As predicted in Fig. 3.10, only a little change in the stress strain curve is observed under strain rate 2000/s. When the strain rate is higher than 2000/s, the stress strain curve changes apparently with strain rate. Nemat-Nasser et al [14] argued that the mechanism for transformation varies when the strain rate is higher than a critical value. According to our current model, the constitutive relation of SMA is influenced by the transformation resistance $f_D(\xi)$, which plays a dominant role at extremely high strain rate.

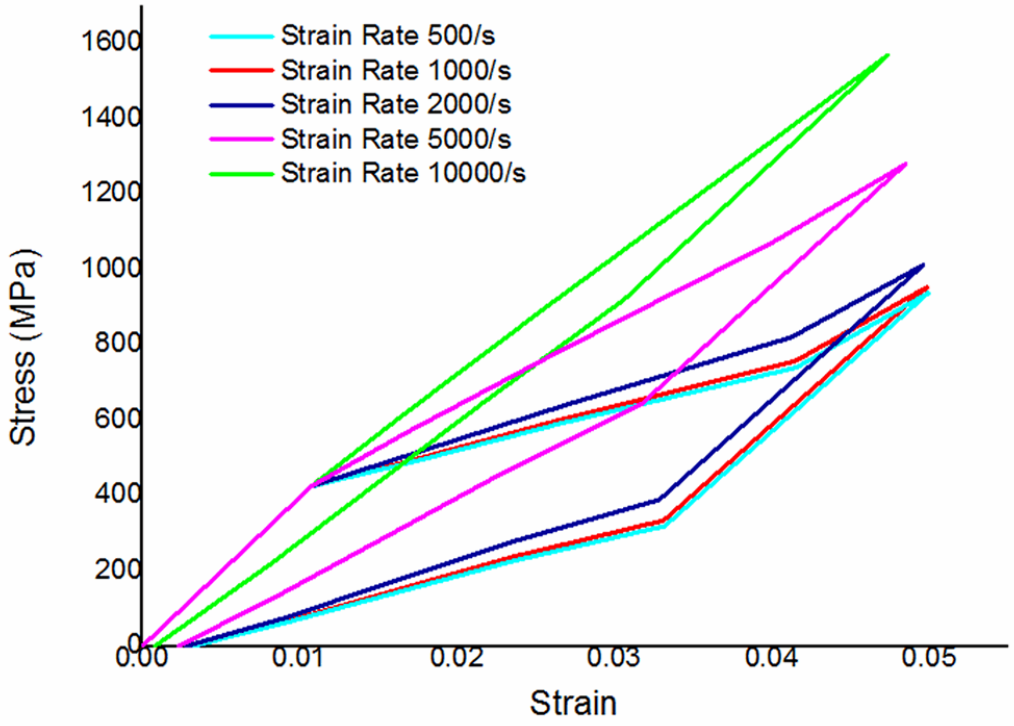

Fig.3.10 Prediction of strain rate effect on stress strain curve at dynamic loading

The temperature increase at different high strain rate is shown in Fig. 3.11. According to the figure, the temperature increase is about 20 ℃ when the strain rate is lower than 2000/s. The maximum temperature decreases when the strain rate increases. At the strain rate of 10000/s, the temperature increase is only about 5 ℃. The trend is different from that at quasi-static deformation when strain rate is lower than 10/s. At quasi-static deformation, the heat conduction is important to the stress strain curve of the material. The heat conduction will be inhibited when the strain rate increases and therefore, the temperature increases with increasing strain rate at quasi-static deformation. The deformation is adiabatic at high strain rate deformation. The temperature increase is related to the latent heat generated during transformation. According to our model, the transformation resistance will increase with increasing strain rate, which decrease the martensitic transformation. Therefore, the temperature decreases with strain rate at high strain rate deformation.

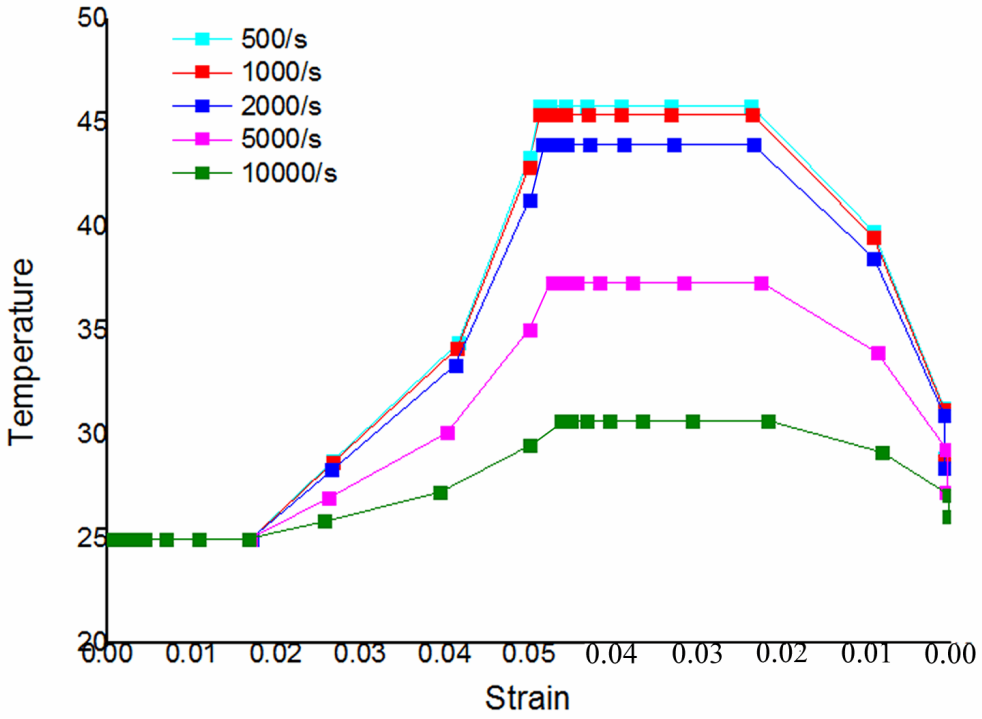

Fig.3.11 Prediction of strain rate effect on temperature at dynamic loading

3.6 Summary and Conclusions

This paper presents a new model for high strain rate deformation of SMAs. Compared to traditional models for quasi-static deformation, the new model is rate-dependent and takes into account the difference in particle velocities during phase transformation. A phenomenological model is established by combining thermodynamic and field equations. According to the model, particle velocity increases with increasing stress. Compared to the traditional models, the new model presented here considers the additional energy needed for kinetic energy change during phase transformation as an attribute to the large increase of stress during phase transformation. Strain rate effect and deformation at different loading/unloading rates are discussed. The increase of strain rate is shown to increase the initial plateau stress for phase transformation. The slope $d\sigma/d\varepsilon$ increases with the increase of strain rate. The value $d\sigma/d\varepsilon$ is close to the elastic modulus of the material at extremely

high strain rate.

3.7 References

[1] Morgan N. Materials Science and Engineering: A 2004;378:16.

[2] Gollerthan S, Young ML, Baruj A, Frenzel J, Schmahl WW, Eggeler G. Acta Materialia 2009;57:1015.

[3] Van Humbeeck J. Materials Science and Engineering: A 1999;273:134.

[4] Otsuka K, Ren X. Intermetallics 1999;7:511.

[5] Ma J, Karaman I, Noebe RD. International Materials Reviews 2010;55:257.

[6] Chen WW, Wu Q, Kang JH, Winfree NA. International Journal of Solids and Structures 2001;38:8989.

[7] Kockar B, Karaman I, Kim JI, Chumlyakov YI, Sharp J, Yu CJ. Acta Materialia 2008;56:3630.

[8] Benafan O, Brown J, Calkins FT, Kumar P, Stebner AP, Turner TL, Vaidyanathan R, Webster J, Young ML. International Journal of Mechanics and Materials in Design 2013;10:1.

[9] Shaw JA, Kyriakides S. Journal of the Mechanics and Physics of Solids 1995;43:1243.

[10] Nemat-Nasser S, Choi JY. Acta Materialia 2005;53:449.

[11] Saletti D, Pattofatto S, Zhao H. Mechanics of Materials 2013;65:1.

[12] Elibol C, Wagner MFX. Materials Science and Engineering: A 2015;643:194.

[13] Nemat-Nasser S, Choi J-Y, Guo W-G, Isaacs JB. Mechanics of Materials 2005;37:287.

[14] Nemat-Nasser S, Yong Choi J, Guo W-G, Isaacs JB, Taya M. Journal of Engineering Materials and Technology 2005;127:83.

[15] Qiu Y, Young ML, Nie X. Metallurgical and Materials Transactions A 2015;46:4661.

[16] Qiu Y, Young ML, Nie X. Shape Memory and Superelasticity 2015;1:310.

[17] Ahadi A, Sun Q. Acta Materialia 2014;76:186.

[18] Yin H, He Y, Sun Q. Journal of the Mechanics and Physics of Solids 2014;67:100.

[19] Chen W, Song B. Journal of Mechanics of Materials and Structures 2006;1:339.

[20] Niemczura J, Ravi-Chandar K. Journal of the Mechanics and Physics of Solids 2006;54:2136.

[21] Abeyaratne R, Knowles JK. Acta materialia 1997;45:1671.

[22] Abeyaratne R, Knowles JK. Archive for rational mechanics and analysis 1991;114:119.

[23] Yu C, Kang G, Kan Q. International Journal of Plasticity 2014;54:132.

[24] Paranjape HM, Manchiraju S, Anderson PM. International Journal of Plasticity 2015.

[25] Chowdhury P, Patriarca L, Ren G, Sehitoglu H. International Journal of Plasticity 2016;81:152.

[26] Thamburaja P. International Journal of Plasticity 2010;26:1195.

[27] Thamburaja P, Pan H, Chau FS. International Journal of Plasticity 2009;25:2141.

[28] Tanaka K. Journal of Pressure Vessel Technology(Transactions of the ASME) 1990;112:158.

[29] Bo Z, Lagoudas D. International Journal of Engineering Sciences 1999;37:1089.

[30] Lagoudas DC, Entchev PB. Mechanics of Materials 2004;36:865.

[31] Lagoudas D, Hartl D, Chemisky Y, Machado L, Popov P. International Journal of Plasticity 2012;32-33:155.

[32] Hartl DJ, Chatzigeorgiou G, Lagoudas DC. International Journal of Plasticity

2010;26:1485.

[33] Zaki W. Smart Materials and Structures 2010;19:025009.

[34] Zaki W. International Journal of Plasticity 2012;37:72.

[35] Zaki W. International Journal of Solids and Structures 2012;49:2951.

[36] Zaki W, Moumni Z. Journal of the Mechanics and Physics of Solids 2007;55:2455.

[37] Zaki W, Moumni Z. Journal of the Mechanics and Physics of Solids 2007;55:2427.

[38] Morin C, Moumni Z, Zaki W. International Journal of Plasticity 2011;27:1959.

[39] Morin C, Moumni Z, Zaki W. International Journal of Plasticity 2011;27:748.

[40] Auricchio F, Boatti E, Reali A, Stefanelli U. Computer Methods in Applied Mechanics and Engineering 2016;299:440.

[41] Auricchio F, Reali A, Stefanelli U. International Journal of Plasticity 2007;23:207.

[42] Ahmadian H, Hatefi Ardakani S, Mohammadi S. International Journal of Solids and Structures 2015;63:167.

[43] Cisse C, Zaki W, Ben Zineb T. International Journal of Plasticity 2016;76:244.

[44] Bekker A, Jimenez-Victory JC, Popov P, Lagoudas DC. International Journal of Plasticity 2002;18:1447.

[45] Chen Y-C, Lagoudas D. Journal of the Mechanics and Physics of Solids 2000;48:275.

[46] Lagoudas DC, Ravi-Chandar K, Sarh K, Popov P. Mechanics of Materials 2003;35:689.

[47] Bekker A, Brinson L. Journal of the Mechanics and Physics of Solids 1997;45:949.

[48] Nakayama H, Zhao Y, Taya M, Chen WW, Urushiyama Y, Suzuki S. Smart Structures and Materials 2005;5761:355.

[49] Ferdinando A, Davide F, Reginald D. Smart Materials and Structures 2007;16:S39.

[50] Masood Taheri A, Mohammad E. Smart Materials and Structures 2014;23:015012.

[51] Făciu C, Molinari A. Acta Mechanica 2013;224:1917.

[52] Qidwai MA, Lagoudas DC. International Journal of Plasticity 2000;16:1309.

[53] Cory J, McNichols Jr J. Journal of Applied Physics 1985;58:3282.

[54] McNichols Jr J, Cory J. Journal of Applied Physics 1987;61:972.

[55] Nemat-Nasser S, Guo W-G. Mechanics of Materials 2006;38:463.

[56] Guo WG, Su J, Su Y, Chu SY. Journal of Alloys and Compounds 2010;501:70.

[57] Yu C, Kang G, Kan Q. Mechanics of Materials 2014;78:1.

CHAPTER 4

THREE-DIMENSIONAL MODELING OF HIGH STRAIN RATE DEFORMATION OF AUSTENITIC SHAPE MEMORY ALLOYS

4.1 Abstract

A three-dimensional model for phase transformation of shape memory alloys during high strain rate deformation is developed and is then calibrated based on experimental results from an austenitic NiTi shape memory alloy (SMA). Stress, strain, and martensitic volume fraction distribution during high strain rate deformation are simulated using finite element analysis software ABAQUS/standard. For the first time, this paper presents a theoretical study of the microscopic band structure during high strain rate compressive deformation. The microscopic transformation band is generated by the phase front and leads to minor fluctuations in sample deformation. The strain rate effect on phase transformation is studied using the model. Both the starting stress for transformation and the slope of the stress-strain curve during phase transformation increase with increasing strain rate.

4.2 Introduction

Shape memory alloys (SMAs) are an important group of "smart" materials capable of large recoverable deformation due either to pseudoelasticity or to the shape memory effect [1]. The mechanism for this unique behavior is due to a diffusionless and reversible martensitic

This chapter is presented in its entirety from H. Yu and M.L. Young: "Three-dimensional modeling of high strain rate deformation of austenitic shape memory alloys", in press in Smart Materials and Structures, November (2017) with permission from IOP publishing

phase transformation activated by loading/unloading or heating/cooling [1]. The most widely used commercial SMAs include NiTi-based, Fe-based, and Cu-based alloys [2]. Due to the large recoverable strain, high damping properties and good biocompatibility, NiTi-based SMAs show the most promise as structural materials for aerospace and biomedical applications [2-6]. While research on mechanical properties of NiTi SMAs deformed at quasi-static strain rates has been abundant, relatively few studies have focused on NiTi SMAs deformed at high strain rates [7-15]. Compared to quasi-static deformation, austenitic NiTi SMAs deformed at high strain rate show three distinct differences [12-15]: (1) The starting stress for phase transformation increases with increasing strain rate. (2) The slope of stress-strain curve during phase transformation increases with increasing strain rate. (3) Latent heat generated during rapid deformation results in an increase in sample temperature. While Nemat-Nasser et al. [8] and Ahadi et al. [7] present representative experimental work of this behavior, various theoretical models have been developed to understand the physical mechanism of martensitic phase transformation and to improve the design of SMA devices [16-20]. Generally speaking, the models can be divided into three groups: a) microscopic thermodynamic, b) micro-macro, and c) macroscopic.

Microscopic models are generally based on SMA's microstructural features such as phase boundaries, grain boundaries, and twinning. [18, 21-29]. The system's energy and stress-strain curves are modeled by Ginzburg-Landau theory or molecular dynamics. The earliest models for SMAs using Landau theory were developed by Falk [21] and later extended by Ball and James [22], Levitas et al. [23], Wang et al. [24], Cho et al. [25], and Zhong and Zhu [26]. Basic energy distribution is related to temperature and strain in these

models. Equilibrium occurs at the energy minima of the system. The system's energy is accounted for at the atomic scale. Lennard-Jones (LJ) [27] or embedded-atom-method (EAM) [28] potentials are the two main potentials for atomic energy among Ni-Ti, Ni-Ni, and Ti-Ti atoms.

Compared to microscopic models that concentrate on the microstructure of SMAs, micro-macro models focus on meso-scale properties based on the mechanical behavior of the phase transformation that occurs in SMAs [30-39]. The macroscopic behavior of SMAs can be modeled from the vector sum of the behavior of single grains, for example, by Mori-Tanaka [30], or Sach and Taylor methods [31]. The transformation strain of each transformation system is assumed to be related to the transformation plane normal vector and direction vector. The total transformation strain is the volume product of the transformation strain of each martensitic variant. Representative work is reported by Stupkiewicz and Gorzynska-Lengiewicz [32], Anand and Gurtin [33], Yu et al. [34-36], Thamburaja et al. [37, 38], and Ostwald [39].

To save computing time, macroscopic models were developed based on experimental data [16, 17, 20, 40-54]. The phenomenological model was first substantiated by Tanaka and Nagaki [40] and later extended [20, 41-45]. Compared to microscopic and micro-macro models, only macroscopic parameters are considered in phenomenological models. Total energy of the system is composed of the Gibbs free energy of the austenitic phase, martensitic phase, and free energy of the mixture. Free energy of the sample is related to temperature, stress, strain, and martensitic volume fraction. Typical macroscopic models are presented in Lagoudas et al. [16, 46-48], Lexcellent et al. [49], Auricchio et al. [17, 50, 51], and Zaki et al.

[41, 44, 52-54].

Compared to models on quasi-static deformation of austenitic and martensitic SMAs, models for high strain rate deformation of SMAs have not been fully developed [55-61]. By considering jump conditions and wave functions, Chen and Lagoudas [55] established a one-dimensional model for stress wave propagation of SMAs under dynamic loading. The thermomechanical law for the material follows the work of Lagoudas et al. [48]. Bekker et al. [56] later established a similar work to model the propagation of the phase transformation front under different impact loading conditions. Acoustic velocity and phase front velocity were modeled under isothermal and adiabatic cases. Niemczura and Ravi-Chandar [57] applied a simple tri-linear stress-strain relationship to model high strain rate deformation of SMAs. Dispersion of the phase front was considered when modeling the velocity of the phase front during impact loading. According to the models discussed above, phase front propagation will lead to the localized phase transformation phenomenon in SMAs under high strain rate deformation; however, experimental observation of the phase front propagation and localized phase transformation is difficult because of the extremely short duration of deformation. Elibol and Wagner [13] studied the localization of martensitic transformation under tension and compression at various strain rates. Lüders-like macroscopic bands are observed in the tensile deformation of NiTi SMAs, while homogeneous deformation occurs at high strain rate compressive loading. Although no macroscopic band structure is observed at compressive loading, minor strain fluctuation is detected in the work of Elibol and Wagner [13].

Experimental difficulty heretofore has precluded comprehensive study of stress, strain,

and martensitic volume fraction distribution during high strain rate deformation. However, for the first time, in the present work, stress, strain, and martensitic volume fraction distribution during high strain rate deformation are studied theoretically and computer simulated. The one-dimensional model for high strain rate deformation of austenitic SMAs was established in the authors' previous paper [62]. A new three-dimensional model is put forth by developing the one-dimensional model [62] through several assumptions. Details of the three-dimensional model are presented in section 4.3. For the first time, the microscopic band structure during high strain rate compressive deformation is studied theoretically and computer simulated by finite element analysis software ABAQUS/standard. The stress strain distribution and evolution of microscopic band structure during high strain rate deformation is discussed in section 4.4. The results of the paper are concluded in section 4.5.

4.3 Development of the Constitutive Model

The three-dimensional model for martensitic phase transformation under high strain rate deformation is established here. The one-dimensional model for high strain rate deformation was reported previously [62]. Several assumptions offered in this section extend the one-dimensional model to three-dimensional deformation and are discussed in section 4.3.1. Compared to quasi-static deformation, the effect of kinetic energy on phase transformation must be considered during high strain rate deformation. Kinetic energy is related to particle velocity and to the speed of the phase front. The three-dimensional form of kinetic energy is discussed in section 4.3.2. Based on thermodynamic equations and dissipative laws, the constitutive relationship for high strain rate deformation of SMAs is presented in section

4.3.3.

4.3.1 Background

Experimental investigation on high strain rate deformation of austenitic NiTi SMAs was performed using a modified Kolsky compression bar, as described previously [9-11]. The SMA rod sample is sandwiched between the incident bar and the transmitted bar. The current paper focuses on a theoretical study of the deformation of a NiTi SMA rod using a Kolsky compression bar. We define the longitudinal direction, i.e., parallel to the drawing direction of the rod, as *x;* and correspondingly, the other two directions are defined as *y* and *z*. The normal stresses in *x, y,* and *z* directions are defined as σ_1, σ_2,and σ_3, respectively. The shear stresses in *x-y, x-z,* and *y-z* planes are defined as τ_{12}, τ_{13} and τ_{23}, respectively. During high strain rate deformation using a Kolsky compression bar, stress in the longitudinal direction is much larger than stress in the other directions. Therefore, deformation in the Euclidean space **W** can be treated as unidirectional compression. Therefore, $\sigma_1 \neq 0, \sigma_2 = \sigma_3 = \tau_{12} = \tau_{13} = \tau_{23} = 0$. According to traditional continuum mechanics, the stress-strain relationship during elastic deformation can be written as:

$$\begin{cases} \varepsilon_1 = \dfrac{\partial u_x}{\partial x} = \dfrac{\sigma_1}{E} \\ \varepsilon_2 = \dfrac{\partial u_y}{\partial y} = -\dfrac{\nu}{E}\sigma_1 = -\nu\varepsilon_1 \\ \varepsilon_3 = \dfrac{\partial u_z}{\partial z} = -\dfrac{\nu}{E}\sigma_1 = -\nu\varepsilon_1 \end{cases} \tag{4.1}$$

where u_x, u_y, u_z are displacement in *x, y, z* directions, respectively; ε_1, ε_2, ε_3 are strain in *x, y, z* directions, respectively; *E* is elastic modulus of the material; and ν is Poisson's ratio of the material. Based on these assumptions, wave function can be generated by momentum conservation in the longitudinal direction. During deformation, change of the cross-sectional

area cannot be ignored. Therefore, in the longitudinal direction, the total force equals $A_0\sigma_1 + \frac{\partial A_0\sigma_1}{\partial x}dx$. A_0 is the cross-sectional area of the sample. The first term is static force, and the second term is inertial force, which leads to energy increase in the longitudinal direction. The relationship can be written as:

$$\frac{\partial A_0\sigma_1}{\partial x}dx \cdot v_1 = \frac{\partial}{\partial t}\left(\frac{1}{2}\rho_0 A_0 dx \cdot {v_1}^2\right) \tag{4.2}$$

The application of equation (4.2) is not limited to elastic deformation; it can be applied during phase transformation. The solution to equation (4.2) is:

$$\rho_0 \frac{\partial v_1}{\partial t} = \frac{\partial \sigma_1}{\partial x} \tag{4.3}$$

From equation (4.1), we can conclude that

$$\frac{\partial \varepsilon_1}{\partial t} = \frac{\partial^2 u_x}{\partial x \partial t} = \frac{\partial v_1}{\partial x} \tag{4.4}$$

Equations (4.3) and (4.4) have forms similar to typical relationships in one-dimensional wave propagation. The Euclidean space **W** has orthogonal basis. Therefore, high strain rate deformation in Kolsky compression bar can be treated as one-dimensional stress propagation in *x* direction and dispersion in *y* and *z* directions. Dispersion per unit volume is related to strain in the cross-sectional plane and takes the form of:

$$\Phi_d = \frac{1}{A_0 dx}\int_{A_0}\frac{1}{2}\rho_0({v_2}^2 + {v_3}^2)dxdydz = \frac{1}{2}\rho_0 v^2 {r_g}^2\left(\frac{\partial \varepsilon_1}{\partial t}\right)^2 \tag{4.5}$$

where Φ_d is dispersion energy and r_g=$\frac{1}{A_0}\int_{A_0}\frac{1}{2}(y^2 + z^2)dydz = a/\sqrt{2}$ for the rod sample with radius *a*. The traditional three-dimensional model for quasi-static deformation of shape memory alloys relates phase transformation to deviatoric stresses in the system [42]. To extend the quasi-static model for shape memory alloys [42] to high strain rate deformation, a nominal inertial force *I* is assumed, and it has the same value in *y* and *z* directions. Therefore, the work done by the inertial force equals half of the dispersion energy:

$$I\dot{\varepsilon}_2 = \frac{1}{2}\frac{\partial}{\partial t}\left(+\frac{1}{4}\rho_0 a^2 \dot{\varepsilon}_2^2\right) \tag{4.6}$$

Equation (4.6) can be solved as:

$$I = \frac{1}{4}\rho_0 a^2 \frac{\delta^2 \boldsymbol{\varepsilon_2}}{\delta t^2} = \frac{1}{4}\rho_0 a^2 \frac{\delta^2 v_2}{\delta y \delta t} \tag{4.7}$$

The nominal inertial force is a fictitious force that leads to cross-sectional dispersion in elastic deformation and martensitic evolution during phase transformation. Jump discontinuities are observed across the phase front during high strain rate deformation [57]. Therefore, inertial stress is assumed to jump to a value equal to deviatoric stress in *y* and *z* directions when phase transformation is activated. In the present case of unidirectional compression, the deviatoric stress in *y* and *z* axes is assumed to trigger martensitic phase transformation in these two directions. During phase transformation, one-dimensional wave theory is assumed to be verified in *y* and *z* directions, respectively. Fig. 4.1 shows deformation and transformation in the *x*-*y* plane. Deformation in the other plane is similar to that in the *x*-*y* plane. Deformation in the sample can be seen as the sum of deformation in different planes. Therefore, deformation in the *x*-*y* plane is representative. When phase transformation is activated, the phase front is formed when speeds of phase front and acoustic wave are different (the maroon region in Fig. 4.1). The phase front is formed in both *x* and *y* directions in *x*-*y* plane. The phase transformation zone is adjacent to the phase front (light blue in Fig. 4.1). As mentioned before, deformation in the system can be seen as the sum of the deformation in all directions. The phase transformation band is therefore depicted as the dark blue region in Fig. 4.1. C_P is the speed of phase front and is related to material properties. C_P is assumed to be the same in all three directions when the material is isotropic.

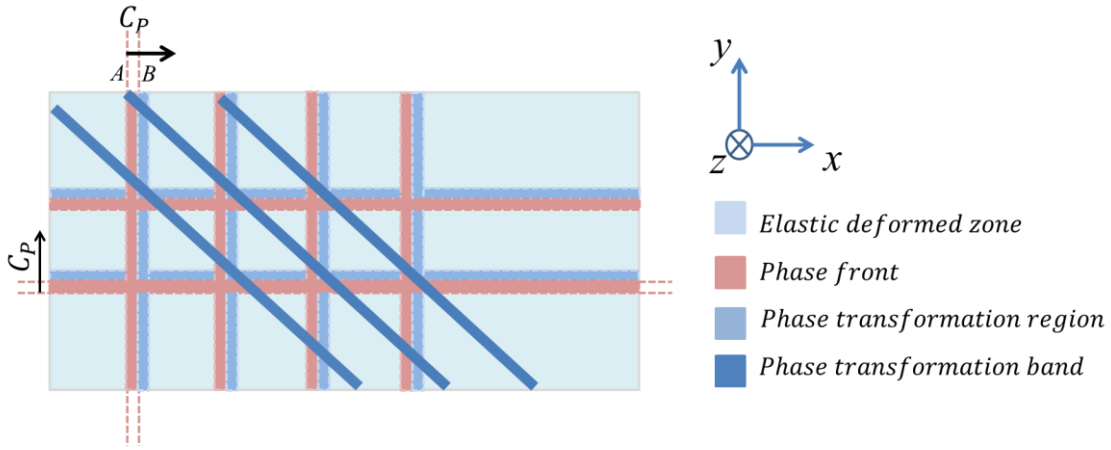

Fig.4.1 Schematic of phase transformation in the *x*-*y* plane during high strain rate deformation

4.3.2 Kinetic Energy during Phase Transformation

In our previous paper [62], the kinetic energy for one dimensional case is:

$$\phi_k = \frac{1}{2}\rho_0 v^2 = \frac{1}{2}\rho_0 v_0^2 + \frac{1}{8}\rho_0 \Lambda_x^2 C_P^2 \xi^2 - \frac{1}{2}\rho_0 \Lambda_x C_P v_0 \xi \tag{4.8}$$

where speed of the phase front in the one-dimensional case is related to global strain rate as:

$$C_P = \kappa \dot{\varepsilon} \tag{4.9}$$

The material parameter κ describes the influence of strain rate to phase boundary velocity, which in our previous paper [62] was determined as 0.73. The directions of stress, strain and particle velocity are assumed not to change at the phase front and therefore the speed of phase front, C_P, can be treated as a scalar value rather than a tensor for simplicity. According to the assumptions made in section 4.3.1, stress, strain and velocity in the *y* and *z* directions during phase transformation can be solved using the same methods discussed above in *x* direction. Therefore:

$$\begin{cases} \boldsymbol{v_0} = -C_P \boldsymbol{\varepsilon_0} \\ \boldsymbol{\sigma} = -\rho_0 C_P \boldsymbol{v_0} \end{cases} \tag{4.10}$$

Kinetic energy in three-dimensional deformation can be written as:

$$\boldsymbol{\phi_k} = \frac{1}{2}\rho_0 \boldsymbol{v}:\boldsymbol{v} = \frac{1}{2}\rho_0 \boldsymbol{v_0}:\boldsymbol{v_0} + \frac{1}{8}\rho_0 \boldsymbol{\Lambda}:\boldsymbol{\Lambda} C_P^2 \xi^2 - \frac{1}{2}\rho_0 C_P \boldsymbol{\Lambda}:\boldsymbol{v_0}\xi \tag{4.11}$$

4.3.3 Constitutive Relationship during High Strain Rate Deformation

The stress-strain relationship during phase transformation at high strain rate deformation is established by energy conservation in the phase transformation band (dark blue in Fig. 4.1). System work then leads to increased internal and kinetic energy. The relationship can be written as:

$$\boldsymbol{\sigma}:\boldsymbol{\varepsilon} + \rho_0 \boldsymbol{U} + \boldsymbol{\phi_k} = 0 \tag{4.12}$$

In this equation, internal energy $\boldsymbol{U}$ is related to the Gibbs free energy of system $\boldsymbol{G}$, entropy of system $\boldsymbol{S}$, and strain energy of system $\boldsymbol{\sigma}:\boldsymbol{\varepsilon}$, which is

$$\boldsymbol{U} = \boldsymbol{G} + T\boldsymbol{S} - \frac{1}{\rho_0}\boldsymbol{\sigma}:\boldsymbol{\varepsilon} \tag{4.13}$$

Gibbs free energy $\boldsymbol{G}$ in equation (4.13) is composed of Gibbs free energy of austenitic phase $\boldsymbol{G_A}$, martensitic phase $\boldsymbol{G_M}$, and energy for phase transformation $\boldsymbol{G_{tr}}$. The form of energy for each phase is written as [42]:

$$\begin{cases} \boldsymbol{G_P} = -\frac{1}{2\rho_0}\boldsymbol{\sigma}:\mathbb{C}_P:\boldsymbol{\sigma} - \frac{1}{\rho_0}\boldsymbol{\sigma}:\boldsymbol{\alpha}_P(T - T_0) + c\left[\left((T - T_0) - TIn\left(\frac{T}{T_0}\right)\right)\right] - T\boldsymbol{S}_P \\ \boldsymbol{G_{tr}} = -\frac{1}{\rho_0}\boldsymbol{\sigma}:\boldsymbol{\varepsilon_{tr}} + \boldsymbol{F}(\xi) \end{cases} \tag{4.14}$$

where $P = A$ *or* M for austenitic or martensitic phase. $\mathbb{C}_P$ is the fourth-order compliance tensor. $\boldsymbol{F}(\xi)$ is transformation hardening energy. $\boldsymbol{\varepsilon_{tr}}$ is transformation strain tensor. In the paper, it is assumed to be related to the martensitic volume fraction $\dot{\xi}$, and this rate alone. Transformation strain $\boldsymbol{\varepsilon_{tr}}$ can be written in three-dimensional form as

$$\dot{\boldsymbol{\varepsilon}}_{tr} = \boldsymbol{\Lambda}\dot{\xi} \tag{4.15}$$

Transformation strain has the same formula as that in the quasi-static deformation model.

Therefore, following the same definition as that in quasi-static deformation, transformation tensor $\boldsymbol{\Lambda}$ is assumed to be related to deviatoric stress $\boldsymbol{\sigma}_{de}$ during forward transformation and transformation strain $\boldsymbol{\varepsilon}_{tr}^{r}$ at transformation reversal. The formation is written as

$$\boldsymbol{\Lambda} = \begin{cases} \frac{3}{2} H \frac{\boldsymbol{\sigma}_{de}}{\|\boldsymbol{\sigma}\|} & \text{for} \quad \dot{\xi} > 0 \\ H \frac{\boldsymbol{\varepsilon}_{tr}^{r}}{\|\boldsymbol{\varepsilon}\|} & \text{for} \quad \dot{\xi} < 0 \end{cases} \tag{4.16}$$

where H is maximum uniaxial transformation strain. $\|\boldsymbol{\sigma}\|$ is the Mises equivalent stress and $\|\boldsymbol{\sigma}\| = \sqrt{\frac{3}{2}\boldsymbol{\sigma}_{de} : \boldsymbol{\sigma}_{de}}$. $\|\boldsymbol{\varepsilon}\|$ is the equivalent strain and $\|\boldsymbol{\varepsilon}\| = \sqrt{\frac{2}{3}\boldsymbol{\varepsilon}_{tr}^{r} : \boldsymbol{\varepsilon}_{tr}^{r}}$. $\boldsymbol{\sigma}_{de}$ is the deviatoric stress and $\boldsymbol{\sigma}_{de} = \boldsymbol{\sigma} - \frac{1}{3}\mathrm{tr}(\boldsymbol{\sigma})\mathbf{I}$.

The total Gibbs free energy $\boldsymbol{G}$ is given as

$$\boldsymbol{G} = (1-\xi)\boldsymbol{G}_A + \xi \boldsymbol{G}_M + \boldsymbol{G}_{tr} = -\frac{1}{2\rho_0}\boldsymbol{\sigma} : \mathbb{C}(\xi) : \boldsymbol{\sigma} - \frac{1}{\rho_0}\boldsymbol{\sigma} : \boldsymbol{\alpha}(\xi)(T - T_0) + c(\xi)\left[(T - T_0) - TIn\left(\frac{T}{T_0}\right)\right] - \boldsymbol{S}(\xi)(T - T_0) - \frac{1}{\rho_0}\boldsymbol{\sigma} : \boldsymbol{\varepsilon_{tr}} + \boldsymbol{F}(\xi) \tag{4.17}$$

where $\mathbb{C}(\xi) := \mathbb{C}_A + \xi(\mathbb{C}_M - \mathbb{C}_A)$, $\boldsymbol{\alpha}(\xi) := \boldsymbol{\alpha}_A + \xi(\boldsymbol{\alpha}_M - \boldsymbol{\alpha}_A)$, $c(\xi) = c_A + \xi(c_M - c_A)$, and $\boldsymbol{S}(\xi) = \boldsymbol{S}_A + \xi(\boldsymbol{S}_M - \boldsymbol{S}_A)$.

The second law of thermodynamics in the form of Clausius-Planck inequality is:

$$\rho_0 \frac{\partial \boldsymbol{S}}{\partial t} \geq 0 \tag{4.18}$$

Combining equations (4.12-18) leads to the conclusion that:

$$\left(\boldsymbol{\varepsilon} + \rho_0 \frac{\partial G}{\partial \boldsymbol{\sigma}}\right)\dot{\boldsymbol{\sigma}} - \rho_0\left(S + \frac{\partial G}{\partial T}\right)\dot{T} + \left[\boldsymbol{\Lambda} : \boldsymbol{\sigma} + \frac{1}{2}\boldsymbol{\sigma} : \Delta\mathbb{C} : \boldsymbol{\sigma} + \Delta\boldsymbol{\alpha} : \boldsymbol{\sigma}(T - T_0) - \rho_0 \Delta c\left((T - T_0) - TIn\left(\frac{T}{T_0}\right)\right) + \rho_0 \Delta S \xi (T - T_0) - \frac{1}{4}\rho_0 C_P^2 \boldsymbol{\Lambda} : \boldsymbol{\Lambda}\xi + \frac{1}{2}\rho_0 C_P \boldsymbol{\Lambda} : \boldsymbol{v_0} - f(\xi)\right]\dot{\xi} \geq 0 \tag{4.19}$$

Following the same treatment as Truesdell and Noll, strain and entropy can be solved as:

$$\boldsymbol{\varepsilon} = -\rho_0 \frac{\partial G}{\partial \boldsymbol{\sigma}} = \mathbb{C} : \boldsymbol{\sigma} + \boldsymbol{\alpha}(T - T_0) + \boldsymbol{\varepsilon_{tr}} \tag{4.20}$$

which can be rewritten in terms of stress by introducing $\mathbb{S} = \mathbb{C}^{-1}$. Equation (4.20) is then written in the common form of Hooke's law:

$$\boldsymbol{\sigma} = \mathbb{S} : [\boldsymbol{\varepsilon} - \boldsymbol{\alpha}(T - T_0) - \boldsymbol{\varepsilon_{tr}}] = \mathbb{S} : [\boldsymbol{\varepsilon} - \boldsymbol{\varepsilon_{th}} - \boldsymbol{\varepsilon_{tr}}] \tag{4.21}$$

In the equation, $\boldsymbol{\varepsilon_{th}}$ is thermal strain. According to equation (4.19), entropy of the system can be solved as

$$\boldsymbol{S} = -\frac{\partial G}{\partial T} = \frac{1}{\rho_0}\boldsymbol{\alpha}(\xi)(T - T_0) + c(\xi)In\left(\frac{T}{T_0}\right) + \boldsymbol{S}(\xi) \tag{4.22}$$

According to equation (4.22), the latent heat generated during deformation can be calculated and is referred to in the authors' previous paper [62]. The driving force for phase transformation is defined as π_{tr} and is related to the term:

$$\boldsymbol{\Lambda}: \boldsymbol{\sigma} + \frac{1}{2}\boldsymbol{\sigma}: \Delta\mathbb{C}: \boldsymbol{\sigma} + \Delta\boldsymbol{\alpha}: \boldsymbol{\sigma}(T - T_0) - \rho_0 \Delta c\left((T - T_0) - TIn\left(\frac{T}{T_0}\right)\right) + \rho_0 \Delta S\xi(T - T_0) -$$

$\frac{1}{4}\rho_0 C_P^2 \boldsymbol{\Lambda}: \boldsymbol{\Lambda}\xi + \frac{1}{2}\rho_0 C_P \boldsymbol{\Lambda}: \boldsymbol{v_0} - f(\xi)$. When equation (4.10) is incorporated into (4.19), the driving force π_{tr} can be written as:

$$\pi_{tr} = \frac{1}{2}\boldsymbol{\Lambda}: \boldsymbol{\sigma} + \frac{1}{2}\boldsymbol{\sigma}: \Delta\mathbb{C}: \boldsymbol{\sigma} + \Delta\boldsymbol{\alpha}: \boldsymbol{\sigma}(T - T_0) - \rho_0 \Delta c\left((T - T_0) - TIn\left(\frac{T}{T_0}\right)\right) + \rho_0 \Delta S\xi(T -$$

$$T_0) - \frac{1}{4}\rho_0 C_P^2 \boldsymbol{\Lambda}: \boldsymbol{\Lambda}\xi - f(\xi) \tag{4.23}$$

The transformation hardening function can be written as [63]

$$f(\xi) = \begin{cases} \frac{1}{2}\rho_0 \Delta S(M_s - M_f) ln(1 - \xi) + \mu_1 & \text{for} \quad \dot{\xi} > 0 \\ \frac{1}{2}\rho_0 \Delta S(A_s - A_f) ln(\xi) + \mu_2 & \text{for} \quad \dot{\xi} < 0 \end{cases} \tag{4.24}$$

where M_s, M_f, A_s, and A_f are starting temperature, finishing temperature for martensitic and austenitic phase transformation, respectively. μ_1 and μ_2 are material constants. According to the formulation (4.19), $\pi_{tr} > 0$, when $\dot{\xi} > 0$ and $\pi_{tr} < 0$, when $\dot{\xi} < 0$. Therefore, the transformation function Φ is defined as:

$$\Phi = \begin{cases} \pi_{tr} - Y & \text{for } \dot{\xi} > 0 \\ -\pi_{tr} - Y & \text{for } \dot{\xi} < 0 \end{cases} \tag{4.25}$$

where Y is internal dissipation during phase transformation. $\Phi \leq 0$ is satisfied during forward ($\dot{\xi} > 0$) and reverse ($\dot{\xi} < 0$) transformations.

4.3.4 Numerical Implementation

The present model is evaluated by computer simulation using finite element analysis software ABAQUS by user material subroutine (UMAT). After each calculation cycle, stress, transformation strain, and total strain are updated by equations (4.15)-(4.24). The new values are then set into equation (4.25) to determine whether phase transformation is activated. When the criteria in equation (4.25) is unsatisfied, which means $\Phi > 0$, stress, transformation strain, and total strain must be updated to satisfy the formulation $\Phi \leq 0$. Several methods have been established for this purpose. The present work selected the cutting plane return mapping algorithm. The details referred to Qidwai and Lagoudas's work [64] and are discussed briefly in the following section. We first assume that at time $t = t_n$, stress, transformation strain, and martensitic volume fractions are calculated as $\boldsymbol{\sigma}_n$, $\boldsymbol{\varepsilon}_{tr_n}$, ξ_n. The condition $\Phi \leq 0$ is satisfied at $t = t_n$. At time $t = t_{n+1}$, a small deformation is applied to the sample. Strain is updated as $\boldsymbol{\varepsilon}_{n+1}$. Stress, transformation strain, and martensitic volume fractions are unknown in the new iteration. In the *k*th iteration, the values calculated before are applied directly and, therefore, $\boldsymbol{\varepsilon}_{tr}{}^{k}_{n+1} = \boldsymbol{\varepsilon}_{tr_n}$, $\xi^k_{n+1} = \xi_n$. $\mathbb{S}$ and $\boldsymbol{\alpha}$ can be calculated when ξ is known. Stress is calculated as

$$\boldsymbol{\sigma}^k_{n+1} = \mathbb{S} : \left[\boldsymbol{\varepsilon}_{n+1} - \boldsymbol{\alpha}(T - T_0) - \boldsymbol{\varepsilon}_{tr}{}^{k}_{n+1}\right] \tag{4.26}$$

The updated stress $\boldsymbol{\sigma}^k_{n+1}$ is then folded into π_{tr} to determine the direction of

transformation. Φ is then calculated to determine whether $\boldsymbol{\sigma}_{n+1}^{k}$ is the correct value for the solution. If $\Phi > 0$, transformation strain should be updated. The martensitic volume fraction is calculated in Qidwai and Lagoudas [65] as

$$\Delta\xi = \frac{\Phi}{\pm\frac{\partial\Phi}{\partial\boldsymbol{\sigma}}:\mathbb{S}:\frac{\partial\Phi}{\partial\boldsymbol{\sigma}}-\frac{\partial\Phi}{\partial\xi}} \tag{4.27}$$

In this equation, "+" stands for forward transformation and "-" stands for reverse transformation. According to equation (4.15), $\Delta\boldsymbol{\varepsilon}_{tr} = \boldsymbol{\Lambda}\Delta\xi$; therefore

$$\xi_{n+1}^{k+1} = \xi_{n+1}^{k} + \Delta\xi \tag{4.28}$$

$$\boldsymbol{\varepsilon}_{tr}{}_{n+1}^{k+1} = \boldsymbol{\varepsilon}_{tr}{}_{n+1}^{k} + \Delta\boldsymbol{\varepsilon}_{tr} \tag{4.29}$$

Equations (4.28) and (4.29) are incorporated into equation (4.26) to calculate $\boldsymbol{\sigma}_{n+1}^{k+1}$. The same procedure is repeated until $\Phi \leq 0$ is satisfied.

4.4 Finite Element Analysis

A schematic of the finite element model for high strain rate deformation on a Kolsky compression bar is shown in Fig. 4.2. Dimensions for the incident and transmitted bars are represented by L_B and D for their length and diameter, respectively; while the sample dimensions are represented by L_S and d for its length and diameter, respectively. Isotropic properties of the material are assumed. To ensure efficient calculation and maintain accuracy, our simulation featured three simplifications. First, lengths of the incident bar and transmitted bar were reduced from 6080 *mm* and 3040 *mm* in the experiment, respectively, to 1000 *mm* in the model. The diameter of the incident bar and transmitted bar is increased from 19 *mm* to 25 *mm*. Length and diameter of the sample are set as 22 *mm* and 18 *mm*, respectively. Second, since the striker in the experiment is used only to generate stress pulse at the impact end of

the incident bar, stress pulse is applied directly to the incident bar. Third, the single loading system in the experiment used to control strain is simplified as a non-deformable rod between the incident bar and the transmitted bar. Frictionless contact is assumed in the tangential direction of the contact between the sample and the bar. Hard contact is assumed as normal behavior of the interaction between the sample and the bar. The mesh of the model is shown in Fig. 4.2.

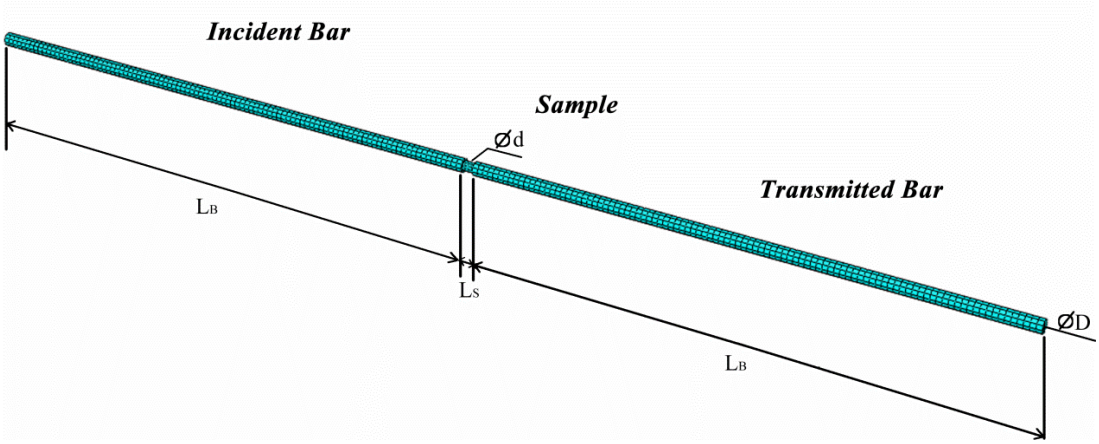

Fig.4.2 ABAQUS finite element mesh of the Kolsky compression bar system

The incident bar and the transmitted bar are made of stainless steel with a Young's modulus and Poisson's ratio of 200 GPa and 0.3, respectively. Bar density is 7.85×10^3 kg/m^3. According to the model established in section 4.3, parameters including Young's modulus, thermal expansion, density, and specific heat of austenitic and martensitic phases; speed of phase boundary C_P; maximum recoverable strain H; start and finish temperatures for austenitic and martensitic phase transformation A_s, A_f, M_s, and M_f, respectively, are needed to solve the constitutive relationship of the material. Material parameters μ_1 and μ_2 are determined by iteration as -4.2 MPa and -6.3 MPa, respectively, based on experimental results [8]. The other model parameters can be referred to in [62].

Stress pulse is applied at the impact end of the incident bar. Pulse duration is calculated

so that incident pulse and transmitted pulse will not overlap during deformation. Wave velocity is calculated as:

$$C_0 = \sqrt{\frac{E}{\rho}} = 5048\, m/s \tag{4.30}$$

where E is Young's modulus and ρ is steel density. To avoid overlap of the wave in the bar, the distance the wave propagated should be less than twice the length of the bar. Therefore, duration of the stress pulse is:

$$t < \frac{2L}{C_0} = 4 \times 10^{-4}\text{s} \tag{4.31}$$

A triangular-shaped pulse is used in the model. Pulse duration is 2.4×10^{-4}s. Peak value is at time 1.6×10^{-4}s. The pulse shape is shown in Fig. 4.3.

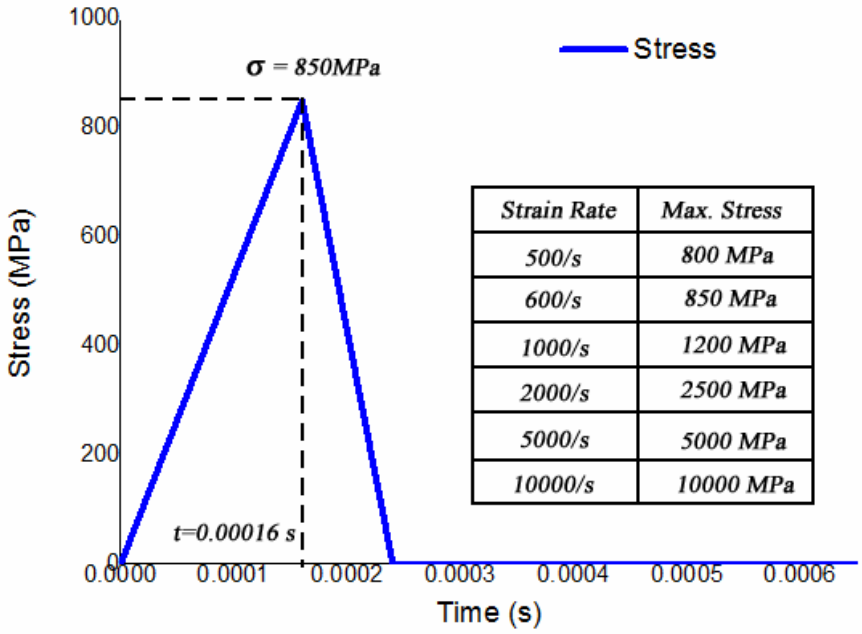

Strain Rate	Max. Stress
500/s	800 MPa
600/s	850 MPa
1000/s	1200 MPa
2000/s	2500 MPa
5000/s	5000 MPa
10000/s	10000 MPa

Fig.4.3 The incident wave pulse structure

4.5 Results and Discussion

4.5.1 Calibration of the Model

The current three-dimensional model is extended by the authors' previous

one-dimensional model, calibration of which can be referred to in [62]. A comparison of the stress-strain relationship simulated by the current three-dimensional model, one-dimensional model in previous paper [62], and directly studied by experiment [8], is shown in Fig. 4.4. The relationship between the von Mises equivalent stress and equivalent strain simulated by the current three-dimensional model is compared with the stress-strain curve by the one-dimensional model [62] and experiment [8]. Note that the simulated stress-strain curve by the current model matches well with the one-dimensional model and the experimental data. Phase transformation is activated at strain about 0.01, and activation stress for phase transformation is about 400 MPa; both are predicted in the model and are revealed in the experiment.

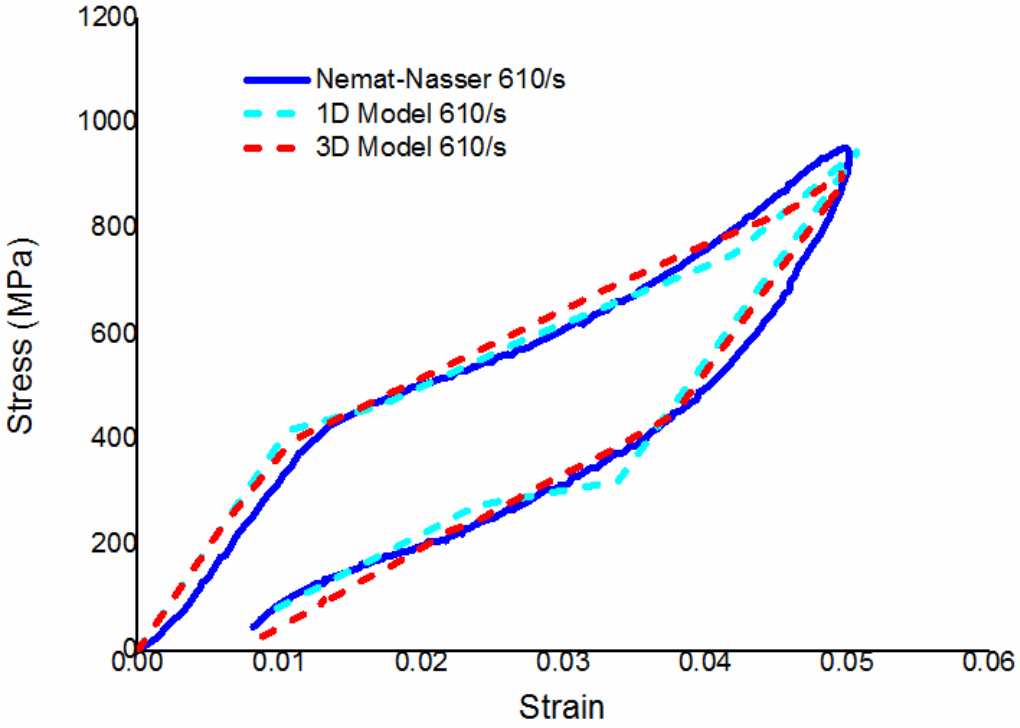

Fig.4.4 Comparison of the stress-strain relation at a strain rate of 610/s by the current 3D model, 1D model [62], and the experimental data [8]

The proposed model can also be used to simulate experimental data [8] at the other strain rates (i.e., 330/s, 570/s, and 1080/s, respectively). The simulated stress-strain responses

of NiTi SMAs by the proposed model at a strain rate of 330/s, 570/s, and 1080/s (Fig. 4.5) reveal that the simulations agree well with the experiment [8]. Slight changes in stress-strain curve are observed both in models and experiment when strain rate increases from 330/s to 1080/s.

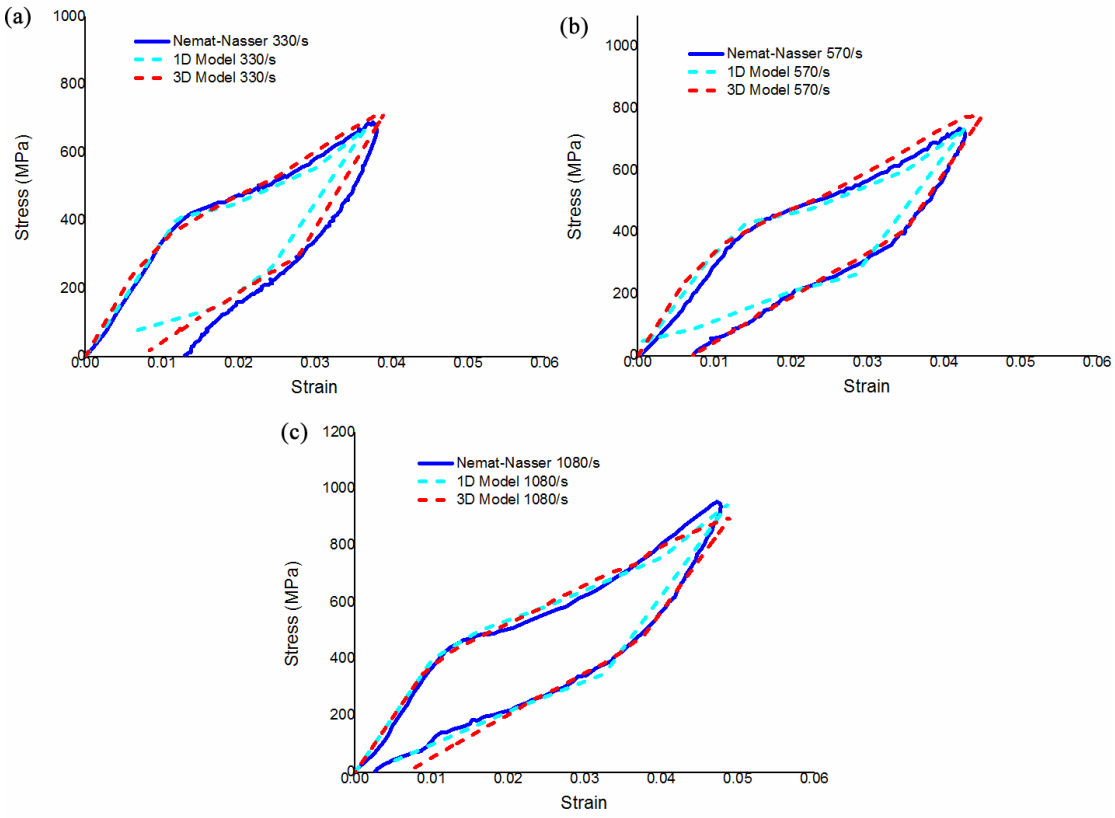

Fig.4.5 Comparison of the stress-strain relation at a strain rate of 330/s, 570/s and 1080/s by current 3D model, 1D model [62], and experiment [8], respectively.

According to the experiments of Elibol and Wagner [13], no macroscopic band structure is observed during high strain rate compression of NiTi SMAs. The experimental result is confirmed in this section by the current model. The macroscopic map of stress distribution in NiTi SMA rod during high strain rate deformation is shown in Fig. 4.6. Generally speaking, stress distributed homogenously during impact deformation indicates one-dimensional equilibrium deformation in the sample. Stress in the middle of the sample is a little lower than at the exterior. When strain is about 1%, stress is about 400 MPa, which is the same as

that shown in the stress-strain curve in Fig. 4.4. The sample is elastically deformed at this strain. According to Fig. 4.6, stress in the sample is lower than that in the bar during elastic deformation of the rod. When strain is about 3%, stress is about 680 MPa. Stress in the sample is higher than that in the bar. The maximum stress is about 900 MPa when sample deformation is about 5%. The sample is also homogenously deformed during the unloading procedure. Stress is lower during the unloading process as compared to the loading process when the sample is deformed to the same strain. Residual strain exists when stress is about 0 MPa.

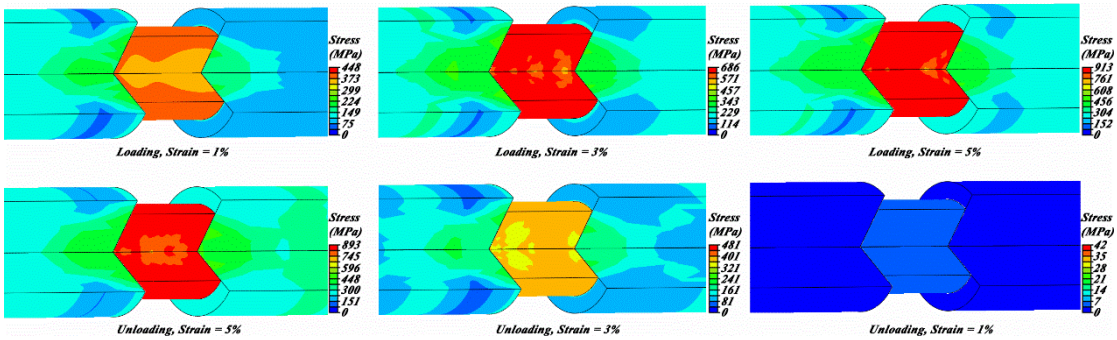

Fig.4.6 Macroscopic maps of stress distribution during high strain rate deformation

Distribution of strain rate and martensitic volume fraction during impact deformation is shown in Fig. 4.7. The moment when the sample is deformed is defined as t=0.00 ms. Strain rate increases quickly at the initial stage of deformation. A constant strain rate of 610/s is observed during the forward transformation at time t=0.06 ms to t=0.14 ms, and the reverse transformation at time t=0.24 ms to t=0.32 ms. A huge change of strain rate is observed during elastic recovery of the sample at time t=0.14 ms to t=0.24 ms. As elastic deformation of the sample is insensitive to strain rate, the huge change of strain rate during elastic deformation of the sample does not affect model accuracy.

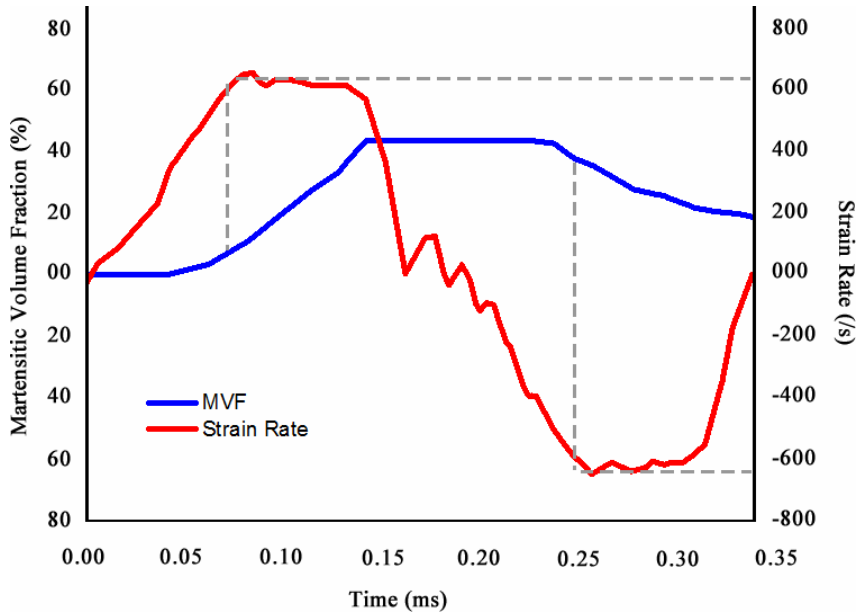

Fig.4.7 Distribution of strain rate and martensitic volume fraction during high strain rate deformation of a NiTi SMA rod

4.5.2 Strain, Stress, and Martensitic Volume Fraction Distribution during Impact Deformation

Elibol and Wagner [13] observe minor strain fluctuations during high strain rate deformation of NiTi SMAs. While not examined thoroughly experimentally, these fluctuations can be modeled as a microscopic band structure Martensitic volume fraction, strain, and stress distribution of NiTi SMAs during impact deformation at a strain rate of 610/s are simulated by the current model (Figs. 4.8, 9, and 10, respectively). Elastic wave structure is presented at strain less than 1% (Fig. 4.9 (a) and 4.10 (a)). No phase transformation is observed when strain is less than 1% (Fig. 4.8 (a)). During elastic deformation, strain and stress of the sample are linearly related to each other by Hook's law, which is indicated by the strain and stress distribution maps (Figs. 4.9 (a) and 4.10 (a)). According to Fig. 4.9 (a), surface region strain is a little higher than in the interior of the sample. When average strain is about 1% (Fig. 4.9 (b)), strain of the exterior of the sample is

about 1.092%. Martensitic phase transformation starts at the exterior of the sample (Fig. 4.8 (b)). According to Figs. 4.8 (b), 4.9 (b), and 4.10 (b), martensitic phase transformation is activated when strain is higher than 1% (Fig. 4.9 (b)). The start stress for phase transformation is about 400 MPa (Fig. 4.10 (b)). When the whole sample is under martensitic phase transformation, microscopic band structure appears (Figs. 4.8 (c) and 4.9 (c)). The mechanism for the formation of the microscopic band structure as discussed in section 4.3.1 pointed out that the phase front will divide the sample between pre-deformed zones and phase transformation bands. A larger volume fraction of martensite exists in the phase transformation band than in the pre-deformed region. Distribution of the strain and martensitic volume fraction in the sample when microscopic band structure is formed are shown in Figs. 4.8 (c) and 4.9 (c), respectively. When average strain is about 2.4%, strain in the phase transformation band of about 2.5% (Fig. 4.9 (c)) corresponds to the martensitic volume fraction of 16% (Fig. 4.8 (c)); while the strain in the pre-deformed zone has a strain of 2.2% (Fig. 4.9 (c)) and martensitic volume fraction of 14% (Fig. 4.8 (c)). Stress distribution at a strain of 2.4% is shown in Fig. 4.10 (c). According to the figure, phase transformation stress is nearly the same as that in the pre-deformed zone (about 560 MPa). The normal direction of the band at 45 ° to the longitudinal direction of the sample indicates that phase front speed is the same in the longitudinal direction and in the direction normal to the sample surface. When the sample is deformed to average strain of 4.1% (Fig. 4.9 (d)), strain in the phase transformation band is about 4.2%, and strain in the pre-deformed zone is about 4.0%. Martensitic volume fraction in the phase transformation band and the pre-deformed zone is about 35% and 33%, respectively (Fig. 4.8 (d)). Stress is about 780

MPa. Maximum martensitic volume fraction is about 44% (Fig. 4.8 (e)) when the sample is deformed to 5% (Fig. 4.9 (e)). Maximum stress in the sample is about 920 MPa (Fig. 4.10 (e)). According to Figs. 4.9 (e) and 4.10 (e), the interior of the sample has a little larger deformation than the exterior of the sample. The phase transformation band structure is clear during forward transformation (Fig. 4.8 (c-e), Fig. 4.9 (c-e)).

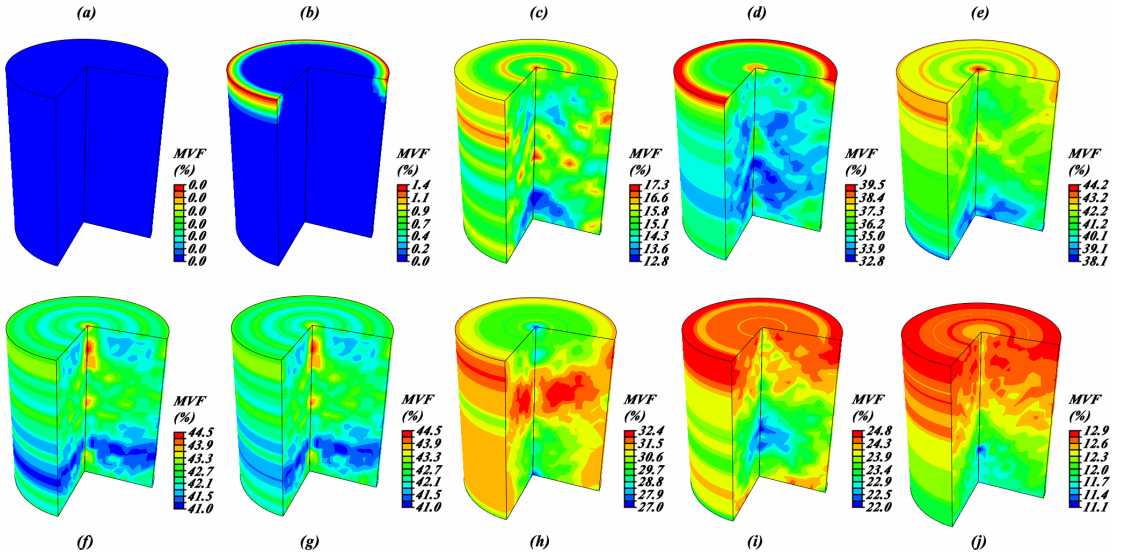

Fig.4.8 Martensitic volume fraction distribution of a NiTi SMA rod deformed at a strain rate of 610/s

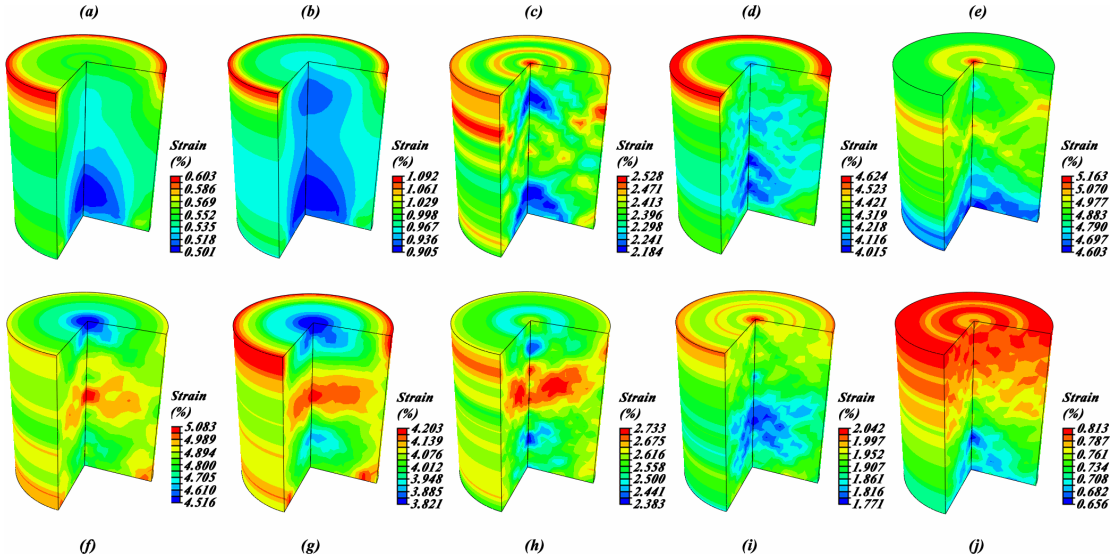

Fig.4.9 Strain distribution of a NiTi SMA rod deformed at a strain rate of 610/s

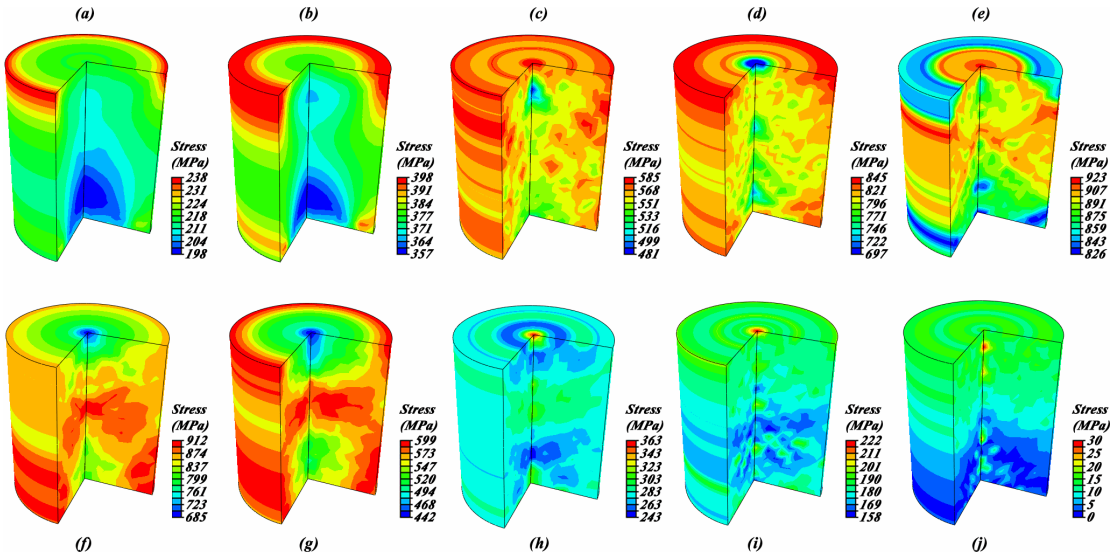

Fig.4.10 Stress distribution of a NiTi SMA rod deformed at a strain rate of 610/s

Sample unloading is shown in Figs. 4.8 (f-j), 4.9 (f-j) and 4.10 (f-j). According to Figs. 4.9 (f) and 4.10 (f), sample unloading appears first in the interior of the sample where strain is about 4.5% and stress is about 685 MPa. When global strain is about 5% (Fig. 4.9 (f)), the exterior of the sample is still under the loading process, while the interior of the sample is under the unloading process. According to Figs. 4.9 (g) and 4.10 (g), the whole sample is under the unloading process when strain is about 4%. Distribution of martensitic volume fraction when average strain is 5% and 4%, respectively, being essentially equivalent during the unloading process (Fig. 4.8 (f) and (g)) indicates that the sample is first elastically recovered during unloading. Reverse martensitic phase transformation is shown in Fig. 4.8 (h) and (i). The phase transformation band structure also appears during the unloading process. Stress is distributed homogenously during the reverse phase transformation (Fig. 4.10 (h) and (i)). When the sample is fully unloaded, average stress is about 0 MPa (Fig. 4.10 (j)). Residual strain is about 0.8% (Fig. 4.9 (j)) when the residual martensitic volume fraction is about 10% (Fig. 4.8 (j)). Figures 4.8, 4.9 and 4.10 also show that the phase transformation band structure is more apparent in the interior than at the exterior of the sample. Therefore, a

critical experimental technique is needed to detect the band structure during phase transformation.

4.5.3 Strain Rate Effect on the Deformation of the Sample

Strain rate effect on the stress strain curve is simulated by the current model; the result confirms that the start stress for phase transformation increases slightly with increased strain rate (Fig. 4.11). When strain rate is lower than 1000/s, the start stress for phase transformation is about 400 MPa, and increases to about 450 MPa when strain rate is 5000/s. The start stress for phase transformation is about 500 MPa when strain rate is 10000/s. A larger slope in the stress strain curve during forward phase transformation is observed with increased strain rate. The slope $d\sigma/d\varepsilon$ equals 13000 MPa when strain rate is less than 1000/s and increases to 205000 MPa when strain rate is 5000/s. The slope $d\sigma/d\varepsilon$ equals 300000 MPa when strain rate is 10000/s. Similar to the forward transformation, the strain stress slope also increases with strain rate during reverse transformation. Fig. 4.11 also verifies that the stress strain curve changes only slightly when strain rate is lower than 1000/s. An apparent change of the stress strain curve is observed at strain rate higher than 2000/s. A nearly linear loading and unloading curve is observed at strain rate 10000/s. The hysteresis area decreases with increased strain rate. A similar trend is also observed in the experiment of Nemat-Nassse et al. [8], who suggested different mechanisms for SMAs deformed at moderately high and very high strain rates. Their observations are confirmed by the current paper and are discussed in detail in the following section.

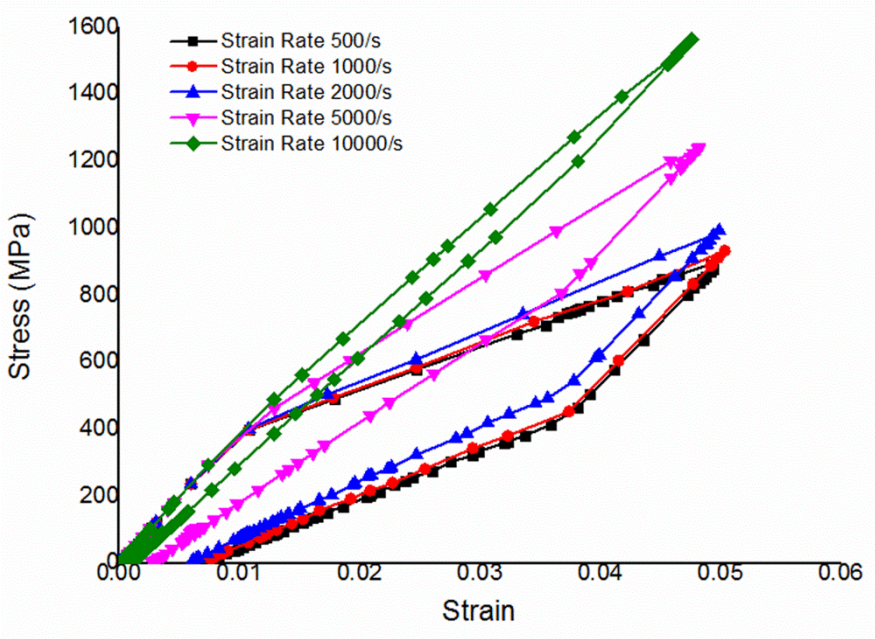

Fig.4.11 Strain rate effect on the stress-strain curve

The effects of strain rate on martensite and strain distribution during loading are shown in Figs. 4.12 and 4.13, respectively. When global strain is less than 1%, the sample is elastically deformed. Martensitic distribution and strain flow are similar for all strain rates. Martensitic phase transformation starts at strain of 1% no matter the strain rates. When global strain is 2%–5%, phase transformation is activated. A distinct difference is observed for strain rates lower and higher than 2000/s. The microscopic band is formed at strain rates lower than 2000/s. The band structure becomes vague with increased strain rate. When strain rate is higher than 2000/s, the band structure disappears, and the material behaves like traditional metals. This phenomenon can be explained by the change of resistance during high strain rate deformation with strain rate. According to the current model, resistance for transformation increases with strain rate. Therefore, stress needed for phase transformation increases. The slope of the stress-strain curve then increases. According to the current model, phase front speed is related to the slope of the stress-strain curve during phase transformation.

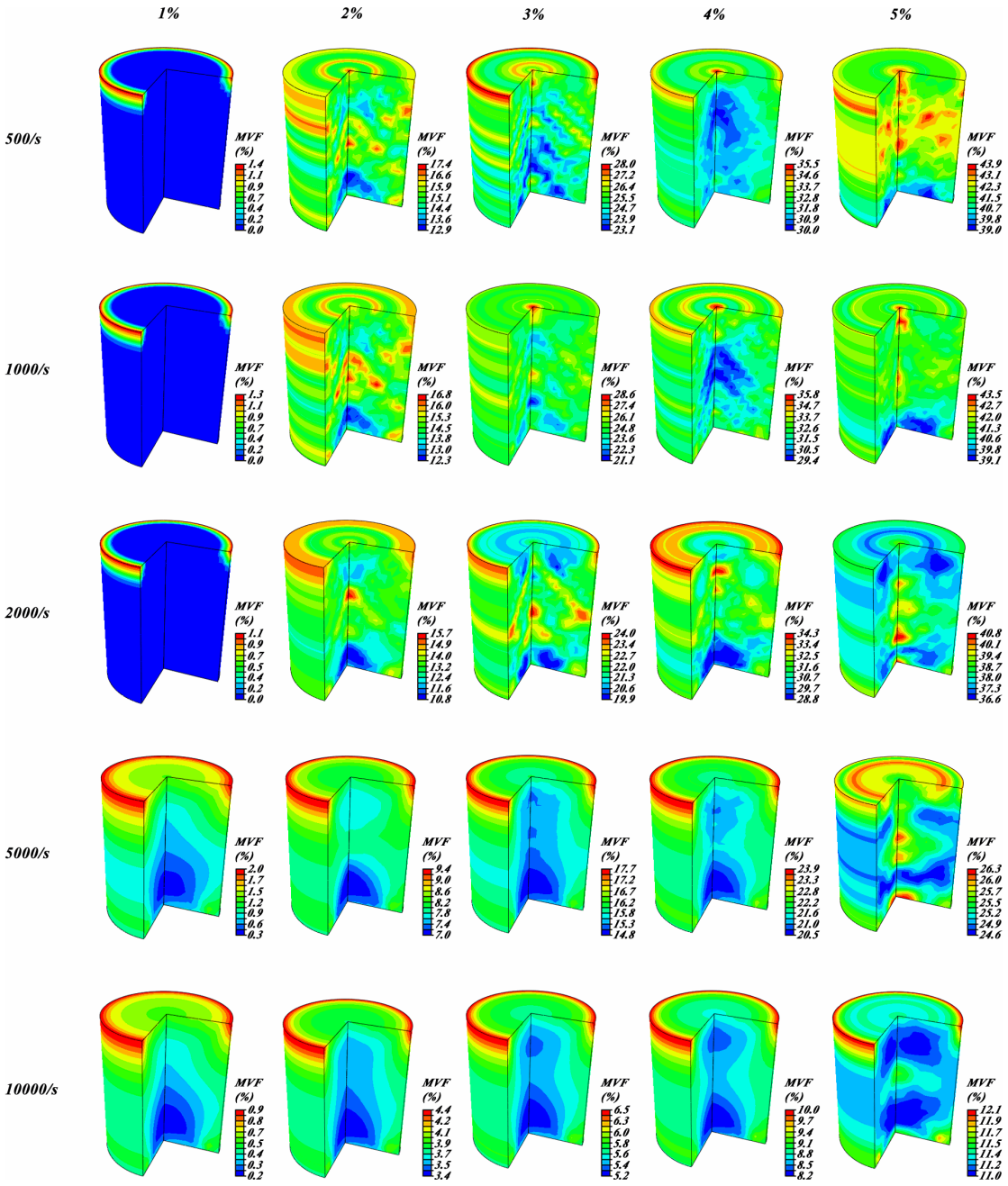

Fig.4.12 Strain rate effect on the distribution of martensitic volume fraction during high strain rate deformation

When the strain rate is high enough, the slope of the stress-strain curve during phase transformation is close to the elastic modulus of the material. Phase front speed is then close to elastic wave velocity. According to the current model, the microscopic band is formed due to the difference between phase front speed and elastic wave velocity. The microscopic band is inhibited at high strain rate, and the sample then behaves like traditional metals.

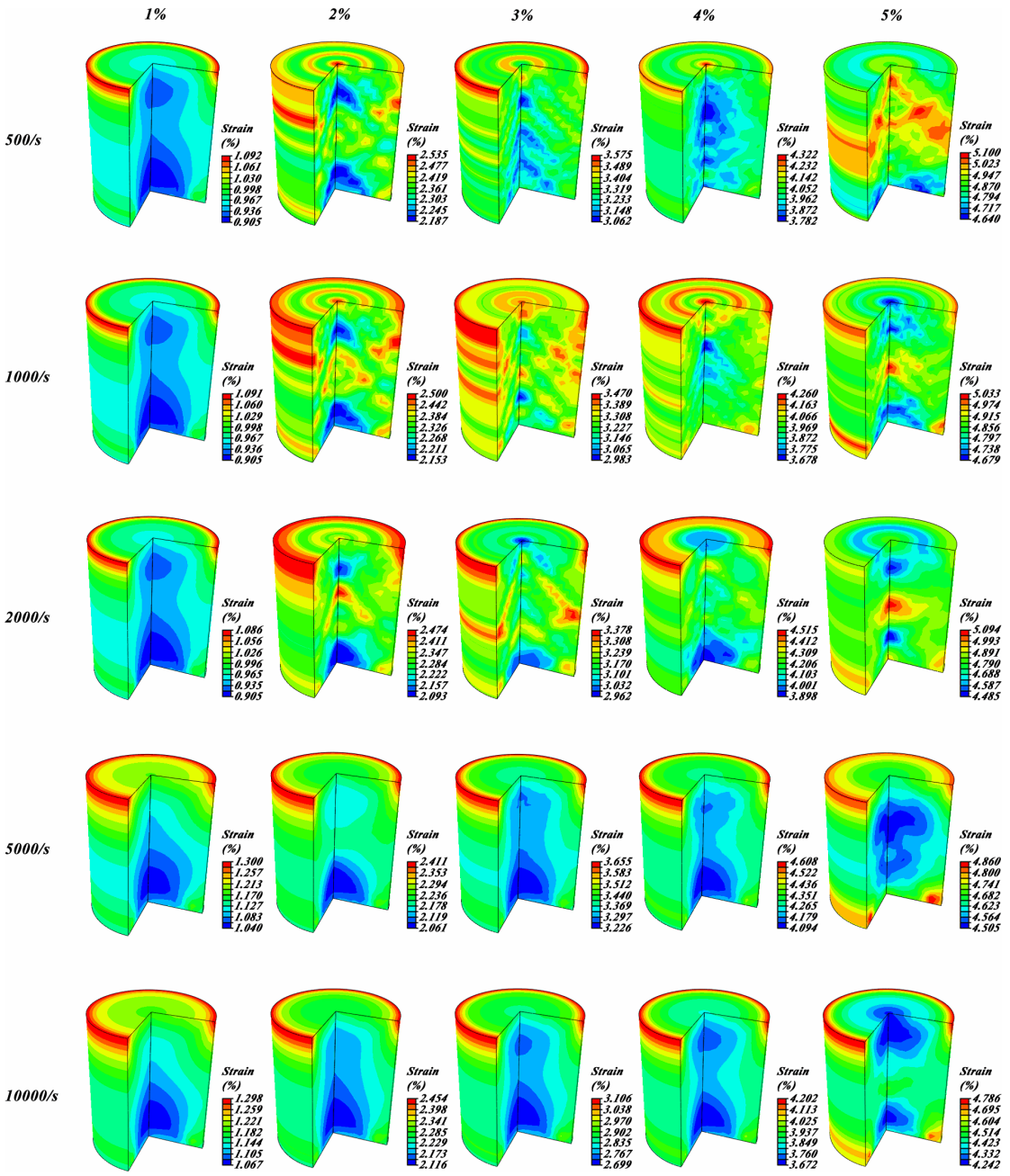

Fig.4.13 Strain rate effect on strain distribution during deformation

Therefore, the martensite appears everywhere in the sample during phase transformation without microscopic band formation and propagation when strain rate is higher than 2000/s. Fig. 4.11 also confirms that the maximum volume fraction of martensite decreases with strain rate. When strain rate is less than 1000/s, maximum martensitic volume fraction is about 44% at a strain of 5%. The maximum martensitic volume fraction decreases to 26% when strain

rate is 5000/s. The value is only about 12% when strain rate is 10000/s.

4.6 Conclusions

A three-dimensional model for high strain rate deformation is compared with experimental data from an austenitic NiTi SMA rod sample under unidirectional compression during high strain rate deformation using a Kolsky bar. One-dimensional equilibrium is satisfied during deformation, and macroscopic stress is distributed homogenously. The model shows that microscopic band structure during phase transformation divides the sample into pre-phase-transformed and phase-transformed regions. The microscopic band structure disappears when the strain rate is higher than 2000/s. Increasing strain rate causes an increase of the start stress for phase transformation and the slope of the stress-strain curve. The model shows that the sample is less sensitive to strain rate when strain rate is less than 2000/s. A linear stress-strain relationship is observed at extremely high strain rate.

4.7 References

[1] Shaw JA, Kyriakides S. Journal of the Mechanics and Physics of Solids 1995;43:1243.

[2] Otsuka K, Ren X. Intermetallics 1999;7:511.

[3] Gollerthan S, Young ML, Baruj A, Frenzel J, Schmahl WW, Eggeler G. Acta Materialia 2009;57:1015.

[4] Morgan N. Materials Science and Engineering: A 2004;378:16.

[5] Van Humbeeck J. Materials Science and Engineering: A 1999;273:134.

[6] Ma J, Karaman I, Noebe RD. International Materials Reviews 2010;55:257.

[7] Ahadi A, Sun Q. Acta Materialia 2014;76:186.

[8] Nemat-Nasser S, Yong Choi J, Guo W-G, Isaacs JB, Taya M. Journal of Engineering Materials and Technology 2005;127:83.

[9] Qiu Y, Young ML, Nie X. Metallurgical and Materials Transactions A 2015;46:4661.

[10] Qiu Y, Young ML, Nie X. Metallurgical and Materials Transactions A 2016:1.

[11] Qiu Y, Young ML, Nie X. Shape Memory and Superelasticity 2015;1:310.

[12] Chen W, Song B. Journal of Mechanics of Materials and Structures 2006;1:339.

[13] Elibol C, Wagner MFX. Materials Science and Engineering: A 2015;643:194.

[14] Nemat-Nasser S, Guo W-G. Mechanics of Materials 2006;38:463.

[15] Nemat-Nasser S, Choi JY. Acta Materialia 2005;53:449.

[16] Lagoudas D, Hartl D, Chemisky Y, Machado L, Popov P. International Journal of Plasticity 2012;32-33:155.

[17] Auricchio F, Boatti E, Reali A, Stefanelli U. Computer Methods in Applied Mechanics and Engineering 2016;299:440.

[18] Chowdhury P, Patriarca L, Ren G, Sehitoglu H. International Journal of Plasticity 2016;81:152.

[19] Chatziathanasiou D, Chemisky Y, Chatzigeorgiou G, Meraghni F. International Journal of Plasticity 2016;82:192.

[20] Cisse C, Zaki W, Ben Zineb T. International Journal of Plasticity 2016;76:244.

[21] Falk F. Zeitschrift für Physik B Condensed Matter 1983;51:177.

[22] Ball JM, James RD. Fine Phase Mixtures as Minimizers of Energy. Analysis and Continuum Mechanics: A Collection of Papers Dedicated to J. Serrin on His Sixtieth Birthday.

Berlin, Heidelberg: Springer Berlin Heidelberg, 1989. p.647.

[23] Levitas VI, Preston DL, Lee D-W. Physical Review B 2003;68:134201.

[24] Wang Y, Khachaturyan AG. Acta Materialia 1997;45:759.

[25] Cho J-Y, Idesman A, Levitas V, Park T. International Journal of Solids and Structures 2012;49:1973.

[26] Zhong Y, Zhu T. Acta Materialia 2014;75:337.

[27] Suzuki T, Shimono M. A simple model for martensitic transformation. Journal de Physique IV (Proceedings), vol. 112: EDP sciences, 2003. p.129.

[28] Sato T, Saitoh K, Shinke N. Materials Science and Engineering: A 2008;481:250.

[29] Uehara T, Asai C, Ohno N. Modelling and Simulation in Materials Science and Engineering 2009;17:035011.

[30] Mori T, Tanaka K. Acta metallurgica 1973;21:571.

[31] Šittner P, Novák V. International Journal of Plasticity 2000;16:1243.

[32] Stupkiewicz S, Górzyńska-Lengiewicz A. Continuum Mechanics and Thermodynamics 2012;24:149.

[33] Anand L, Gurtin ME. Journal of the Mechanics and Physics of Solids 2003;51:1015.

[34] Yu C, Kang G, Kan Q. Journal of the Mechanics and Physics of Solids 2015;82:97.

[35] Yu C, Kang G, Kan Q. Mechanics of Materials 2014;78:1.

[36] Yu C, Kang G, Kan Q. International Journal of Plasticity 2014;54:132.

[37] Thamburaja P, Pan H, Chau FS. International Journal of Plasticity 2009;25:2141.

[38] Thamburaja P, Anand L. Acta Materialia 2003;51:325.

[39] Ostwald R. Modelling and simulation of phase transformations in elasto-plastic

polycrystals. 2015.

[40] Tanaka K, Nagaki S. Ingenieur-Archiv 1982;51:287.

[41] Zaki W. Smart Materials and Structures 2010;19:025009.

[42] Hartl DJ, Chatzigeorgiou G, Lagoudas DC. International Journal of Plasticity 2010;26:1485.

[43] Boyd JG, Lagoudas DC. International Journal of Plasticity 1996;12:805.

[44] Zaki W, Moumni Z. Journal of the Mechanics and Physics of Solids 2007;55:2455.

[45] Bo Z, Lagoudas D. International Journal of Engineering Sciences 1999;37:1089.

[46] Lagoudas DC, Entchev PB. Mechanics of Materials 2004;36:865.

[47] Lagoudas DC, Ravi-Chandar K, Sarh K, Popov P. Mechanics of Materials 2003;35:689.

[48] Lagoudas D, Bo Z. International Journal of Engineering Sciences 1999;37:1141.

[49] Lexcellent C, Blanc P, Creton N. Materials Science and Engineering: A 2008;481:334.

[50] Auricchio F, Reali A, Stefanelli U. International Journal of Plasticity 2007;23:207.

[51] Auricchio F, Taylor RL, Lubliner J. Computer Methods in Applied Mechanics and Engineering 1997;146:281.

[52] Zaki W. International Journal of Plasticity 2012;37:72.

[53] Zaki W. International Journal of Solids and Structures 2012;49:2951.

[54] Zaki W, Moumni Z. Journal of the Mechanics and Physics of Solids 2007;55:2427.

[55] Chen Y-C, Lagoudas D. Journal of the Mechanics and Physics of Solids 2000;48:275.

[56] Bekker A, Jimenez-Victory JC, Popov P, Lagoudas DC. International Journal of Plasticity 2002;18:1447.

[57] Niemczura J, Ravi-Chandar K. Journal of the Mechanics and Physics of Solids

2006;54:2136.

[58] Niknami A, Shariyat M. Thin-Walled Structures 2016;106:166.

[59] Shariyat M, Niknami A. Composite Structures 2016;153:692.

[60] Shariyat M, Niknami A. Composite Structures 2016;136:191.

[61] Ziętek G, Mróz Z. The International Journal of Structural Changes in Solids 2011;3:21.

[62] Yu H, Young ML. Journal of Alloys and Compounds 2017;710:858.

[63] Tanaka K. Res. Mechanica: International Journal of Structural Mechanics and Materials Science 1986;18:251.

[64] Qidwai M, Lagoudas D. International Journal for Numerical Methods in Engineering 2000;47:1123.

[65] Qidwai MA, Lagoudas DC. International Journal of Plasticity 2000;16:1309.

CHAPTER 5

TEMPERATURE EFFECT ON MATERIAL FLOW BEHAVIOR AT HIGH STRAIN RATE DEFORMATION OF AUSTENITIC SHAPE MEMORY ALLOYS BY PHENOMENOLOGICAL MODELING

5.1 Abstract

High strain rate compressive behavior of austenitic shape memory alloys (SMAs) is investigated by finite element analysis at temperatures ranging from the martensitic start temperature (Ms) to the temperature (Md) above which stress-induced martensite no longer forms. It is found that the start stress for phase transformation increases with increasing temperature. The maximum martensitic volume fraction during phase transformation decreases with increasing temperature. When the ambient temperature is higher than Md, phase transformation is no longer observed and the SMA deforms like a pure elastic material according to the model. At temperatures below Md and above Ms, the microscopic band structure is observed during phase transformation. The critical strain for initiation of the band structure increases with increasing temperature. The band structure disappears at temperatures approaching or above Md. The same influence of temperature on the compressive behavior is observed for different high strain rates. In the model, the temperature Md is assumed to be ~100 ℃ higher than the austenitic finish temperature (Af) and is independent of strain rate.

5.2 Introduction

Shape memory alloys (SMAs) are a group of unique alloys capable of enduring large recoverable deformation which results from reversible martensitic phase transformation induced by stress, temperature, or a magnetic field [1, 2]. The start and finish temperature for the forward transformation is defined as the austenitic start temperature (A_s) and austenitic finish temperature (A_f), respectively. Similarly, the start and finish temperature for the reverse transformation is defined as the martensitic start (M_s) and martensitic finish temperature (M_f), respectively. When an SMA is deformed at temperatures higher than A_f and below M_d, some inelastic strain will be recovered after unloading. This phenomenon is known as pseudoelasticity [1].

It is known that the martensitic phase transformation is sensitive to the strain rate and temperature [3-8]. The strain rate effect on the mechanical properties has been studied on the deformation of austenitic [9, 10] and martensitic [11-13] SMAs. Ahadi and Sun [14] reported that the start stress for the transformation and work hardening rate increases with increasing strain rate when samples are deformed at strain rate ranging from 4×10^{-5}/s to 1×10^{-1}/s. Similar behavior is also observed at various high strain rates [6-10, 15]. Nemat-Nasser et al. [6] studied the high strain rate deformation from 330/s to 1080/s of 50.4Ni-49.6Ti (at.%) at room temperature. In their study, the observed transition stress increases with increasing strain rate. The work hardening rate in phase transformation regime increases steadily and then rapidly with increasing strain rate. A similar result is concluded in the high strain rate deformation of austenitic SMAs with same and different compositions at room temperature and high temperatures [7-10, 15]. The increase in temperature by deformation work and latent

heat generated during phase transformation was used to explain the work hardening observed with increasing strain rate, while a maximum temperature increment is observed at strain rates higher than 1.2×10^{-1}/s [3]. Niemczura and Ravi-Chandar [16] related the driving force for the transformation to the phase front velocity at quasi-dynamic deformation of austenitic NiTi SMAs. The relationship between the phase front velocity and strain rates on the deformation of NiTi SMA wires is studied by Shaw and Kyriakides [2] . The increase of strain rate leads to an increase in the phase front velocity, which increases the critical driving force for phase transformation. A few studies have focused on the influence of temperature on the stress strain behavior at quasi-static and high strain rate deformation of austenitic and martensitic SMAs [4, 5, 11]. Benafan et al. [4] reported that the start stress for phase transformation increases when $Ni_{49.9}Ti_{50.1}$(at.%) is isothermally deformed at temperatures between 165 ℃ and 290 ℃ and decreases when the SMA is isothermally deformed at a temperature above M_d. No stress-induced martensite is observed when the SMA is deformed above M_d. The high strain rate compressive behavior of martensitic NiTi SMAs at different temperatures has been studied by Qiu et al. [11]. It is found that the critical stress for the transformation increases first and then decreases with increasing temperatures. The phenomenon is attributed to the competing strain hardening and thermal softening effects. Chen and Bo [5] studied the effect of temperature from 0 ℃ to 50 ℃ on the stress strain curve of NiTi SMAs deformed at 430/s. The work hardening behavior is observed with increasing temperature.

Although some research has been performed on the mechanical properties of high strain rate deformation of SMAs at various temperatures [4, 5, 11], research on the microstructural

evolution during high strain rate deformation of SMAs at various temperatures is limited, likely due to the fact that the deformation occurs over an extremely short amount of times, thus, making it difficult to observe the microstructural evolution. Accurate modeling techniques potentially not only save experimental time but also provide a substitutive method for studying the microstructural changes which occur during high strain rate deformation. The models can be generally divided into microscopic thermodynamic models [17, 18], micro-macro models [19-22], and macroscopic models [23-28] according to the scales the models are focused on. Microscopic thermodynamic models and micro-macro models focus on the relationship between the macroscopic mechanical properties and microscopic material properties such as grain boundaries, slip systems, etc... Due to the efficiency of computer calculation, macroscopic phenomenological models are already established. The phase transformation is related to the change of martensitic phase fraction with macroscopic scalars such as transformation strain, irrecoverable deformation, stress, and temperature. A phenomenological model for the high strain rate deformation of austenitic SMAs has been presented in our previous paper [29]. In this paper, the previous model is summarized and the effect of temperature on the mechanical properties of the material under various strain rates is added to the previous model.

5.3 Framework of the Model

The macroscopic model for high strain rate deformation of austenitic NiTi SMAs has been established in our previous research [29] to describe the strain rate effect on the mechanical properties of the material at room temperature. The model is summarized and

extended here to account for the effect of temperature on the high strain rate deformation of SMAs. During high strain rate deformation of SMAs at various temperatures, the total strain includes the elastic strain $\boldsymbol{\varepsilon_e}$, thermal strain $\boldsymbol{\varepsilon_{th}}$, and transformation strain $\boldsymbol{\varepsilon_{tr}}$ as follows:

$$\boldsymbol{\varepsilon} = \boldsymbol{\varepsilon_e} + \boldsymbol{\varepsilon_{th}} + \boldsymbol{\varepsilon_{tr}} \tag{5.1}$$

In this equation, elastic strain can be written as:

$$\boldsymbol{\varepsilon_e} = \mathbb{C}:\boldsymbol{\sigma} \tag{5.2}$$

Where $\mathbb{C}$ is the effective compliance tensor and is related to the elastic tensor of austenitic phase $\mathbb{C}_A$, martensitic phase $\mathbb{C}_M$, and the martensitic volume fraction ξ as follows:

$$\mathbb{C}(\xi) := \mathbb{C}_A + \xi(\mathbb{C}_M - \mathbb{C}_A) \tag{5.3}$$

The thermal strain $\boldsymbol{\varepsilon_{th}}$ is related to the ambient temperature T, initial temperature T_0, and thermal expansion parameter $\boldsymbol{\alpha}$ according to:

$$\boldsymbol{\varepsilon_{th}} = \boldsymbol{\alpha}(T - T_0) \tag{5.4}$$

The transformation strain in equation (5.1) is related to the martensitic volume fraction ξ and transformation tensor $\boldsymbol{\Lambda}$ as follows:

$$\boldsymbol{\varepsilon_{tr}} = \boldsymbol{\Lambda}\xi \tag{5.5}$$

In equation (5.5), the transformation tensor $\boldsymbol{\Lambda}$ is written as:

$$\boldsymbol{\Lambda} = \begin{cases} \frac{3}{2} H \frac{\boldsymbol{\sigma}_{de}}{\|\boldsymbol{\sigma}\|} & \text{for} \quad \dot{\xi} > 0 \\ H \frac{\boldsymbol{\varepsilon}^r_{tr}}{\|\boldsymbol{\varepsilon}\|} & \text{for} \quad \dot{\xi} < 0 \end{cases} \tag{5.6}$$

In equation (5.6), H is the maximum uniaxial transformation strain. $\|\boldsymbol{\sigma}\|$ is the von Mises equivalent stress and $\|\boldsymbol{\sigma}\| = \sqrt{\frac{3}{2}\boldsymbol{\sigma}_{de}:\boldsymbol{\sigma}_{de}}$. $\|\boldsymbol{\varepsilon}\|$ is the equivalent strain and $\|\boldsymbol{\varepsilon}\| = \sqrt{\frac{2}{3}\boldsymbol{\varepsilon}^r_{tr}:\boldsymbol{\varepsilon}^r_{tr}}$. $\boldsymbol{\sigma}_{de}$ is the deviatoric stress where $\boldsymbol{\sigma}_{de} = \boldsymbol{\sigma} - \frac{1}{3}\mathrm{tr}(\boldsymbol{\sigma})\mathbf{I}$.

The martensitic volume fraction ξ is related to the driving force π_{tr}. According to the

second thermodynamics law, π_{tr} is solved as:

$$\pi_{tr} = \frac{1}{2}\boldsymbol{\Lambda}:\boldsymbol{\sigma} + \frac{1}{2}\boldsymbol{\sigma}:\Delta\mathbb{C}:\boldsymbol{\sigma} + \Delta\boldsymbol{\alpha}:\boldsymbol{\sigma}(T - T_0) - \rho_0\Delta c\left((T - T_0) - TIn\left(\frac{T}{T_0}\right)\right) + \rho_0\Delta ST -$$

$$f_D(\xi) - f_M(\xi) \tag{5.7}$$

where $f_D(\xi)$ is the dynamic hardening energy and is written as:

$$f_D(\xi) = \frac{1}{4}\rho_0 C_P^2\boldsymbol{\Lambda}:\boldsymbol{\Lambda}\xi \tag{5.8}$$

$f_M(\xi)$ is the transformation hardening energy related to the material properties and is written as follows:

$$f_M(\xi) = \begin{cases} \frac{1}{2}\rho_0\Delta S(M_s - M_f)ln(1-\xi) + \mu_1 & \text{for} \quad \dot{\xi} > 0 \\ \frac{1}{2}\rho_0\Delta S(A_s - A_f)ln(\xi) + \mu_2 & \text{for} \quad \dot{\xi} < 0 \end{cases} \tag{5.9}$$

where M_s, M_f, A_s, and A_f is the starting temperature, finishing temperature for martensitic and austenitic phase transformation, respectively. μ_1 and μ_2 are material constant. During the phase transformation, the driving force $\pi_{tr} > 0$, when $\dot{\xi} > 0$ and $\pi_{tr} < 0$, when $\dot{\xi} < 0$. Therefore, the transformation function Φ is defined as:

$$\Phi = \begin{cases} \pi_{tr} - Y \text{ for } \dot{\xi} > 0 \\ -\pi_{tr} - Y \text{ for } \dot{\xi} < 0 \end{cases} \tag{5.10}$$

where *Y* is the internal dissipation during the phase transformation. $\Phi \leq 0$ is satisfied during the forward ($\dot{\xi} > 0$) and reverse ($\dot{\xi} > 0$) transformation. The martensitic volume fraction ξ is related to the transformation function as

$$\dot{\xi} = \frac{\Phi}{\pm\frac{\partial\Phi}{\partial\boldsymbol{\sigma}}:\mathbb{S}:\frac{\partial\Phi}{\partial\boldsymbol{\sigma}} - \frac{\partial\Phi}{\partial\xi}} \tag{5.11}$$

In this equation, "+" stand for the forward transformation and "-" stand for the reverse transformation. During the high strain rate deformation, heat is generated with the phase transformation. The heat flow is related to the driving force for the transformation π_{tr}, the entropy of the material *S*, and the martensitic volume fraction ξ as follows:

$$\rho_0 C \frac{\partial T}{\partial t} = (\pi_{tr} - \rho_0 T \Delta S) \frac{\partial \xi}{\partial t} - T \frac{\partial \alpha(\xi) \sigma}{\partial t} \quad (5.12)$$

The framework of the model is, thus, complete. For more details, please refer to our previous paper [29].

5.4 Results and Discussion

The thermomechanical model for the high strain rate deformation at various temperatures presented in the previous section was coded in user defined material mechanical behavior (UMAT) of finite element analysis software ABAQUS/Standard. Results from the model are discussed here and highlight the effect of temperature on the material flow behavior at high strain rate deformation. The details of the finite element model include the selection of the mesh, the type of the element, the boundary conditions, and the material parameters for the model can be referred to our previous paper [29].

5.4.1 Effect of Temperature on Material Flow Behavior at Selected Strain Rate

As illustrated in Fig. 5.1, simulations of the stress-strain curves of the austenitic NiTi SMAs at temperatures of 25 ℃, 40 ℃, 50 ℃, 75 ℃, 100 ℃, 110 ℃, and 125 ℃ are presented for deformation at a strain rate of 600/s. As the temperature increases, the start stress for the transformation increases and the stress-strain slope during the phase transformation remains nearly constant, indicating that the transition stress is more sensitive to the temperature as compared to the stress increment during the phase transformation. The start stress for the phase transformation at room temperature (25 ℃) is about 210 MPa. It increases to about 450 MPa at temperature 40 ℃, 600 MPa at temperature 50 ℃, 950 MPa at temperature 75 ℃, and

1200 MPa at temperature 100 ℃. The influence of the temperature on the start stress for the transformation is defined as $d\sigma_S/dT$ and equals 16 MPa/K in the present case. When the temperature equals 125 ℃, a linear stress-strain curve is observed, which indicates that no phase transformation is activated during the deformation. The temperature at which the phase transformation is fully inhibited is referred to as M_d. At a deformation strain rate of 600/s, M_d equals 125 ℃, which is about 100 ℃ higher than the austenitic finish temperature A_f. In the current model, the sample is assumed to be fully recovered within the strain of 0.04 and plastic deformation is not included. Therefore, the material behaves like a pure elastic material at M_d.

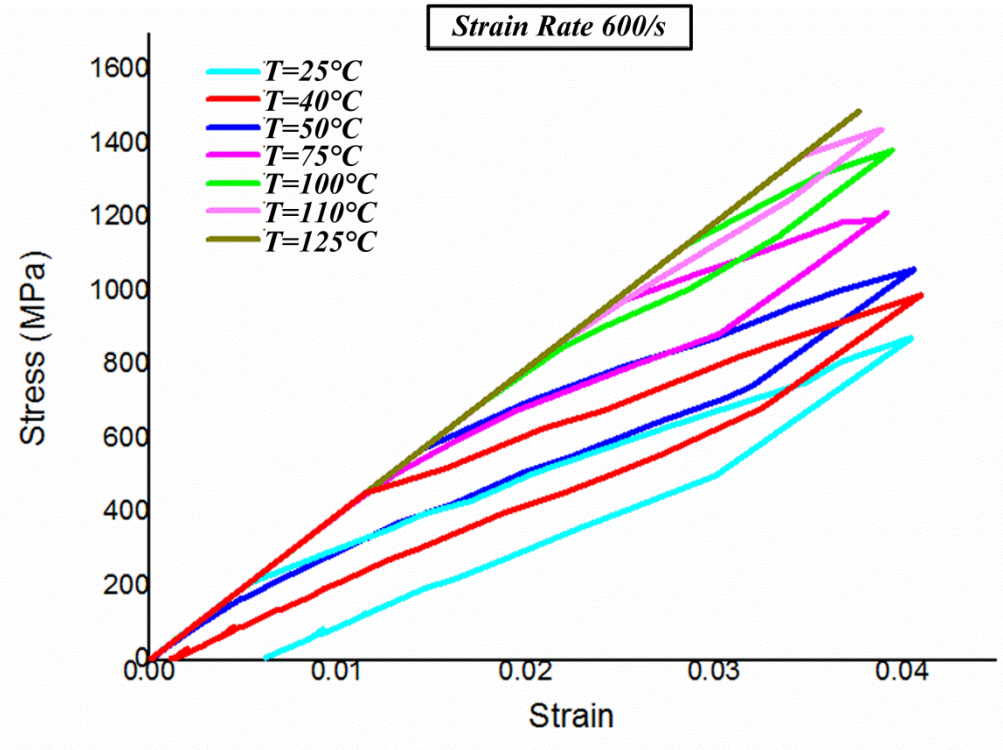

Fig.5.1 Stress-strain curve of austenitic NiTi SMAs at various temperatures (25 ℃, 40 ℃, 50 ℃, 75 ℃, 100 ℃, 110 ℃, 125 ℃) under high strain rate deformation (600/s)

The temperature change during the deformation is shown in Fig. 5.2. Note that the temperature increases when the phase transformation is activated. The maximum temperature is observed at the maximum deformation. The temperature starts to decrease when the sample

is unloaded to the strain of 0.03. The sample will be unloaded to its initial temperature when the strain is fully recovered. The maximum temperatures under the high strain rate deformation at different initial temperature are also shown in Fig. 5.2. When the sample is deformed at room temperature, the maximum temperature of the sample during deformation is 45.5 ℃ and the temperature increment is 20.5 ℃. The maximum temperature increases as the ambient temperature increases. The temperature increment decreases as the ambient temperature increases. When the sample is deformed at the temperature of 110 ℃, the temperature increment is only 3.2 ℃. No temperature increase is observed when the sample is deformed at M_d. The temperature results match well with the change of the hysteresis observed with changing ambient temperature as shown in Fig. 5.1. The hysteresis area decreases with increasing temperature. Therefore, the latent heat generated during the phase transformation decreases with increasing temperature and the temperature increment decreases with increasing temperature.

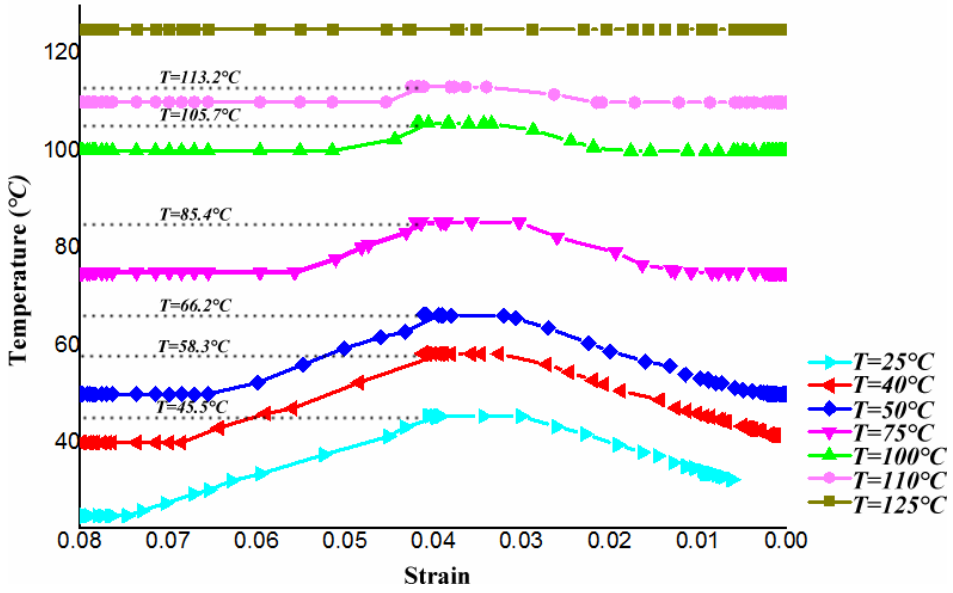

Fig.5.2 Temperature change of austenitic NiTi SMAs under high strain rate deformation

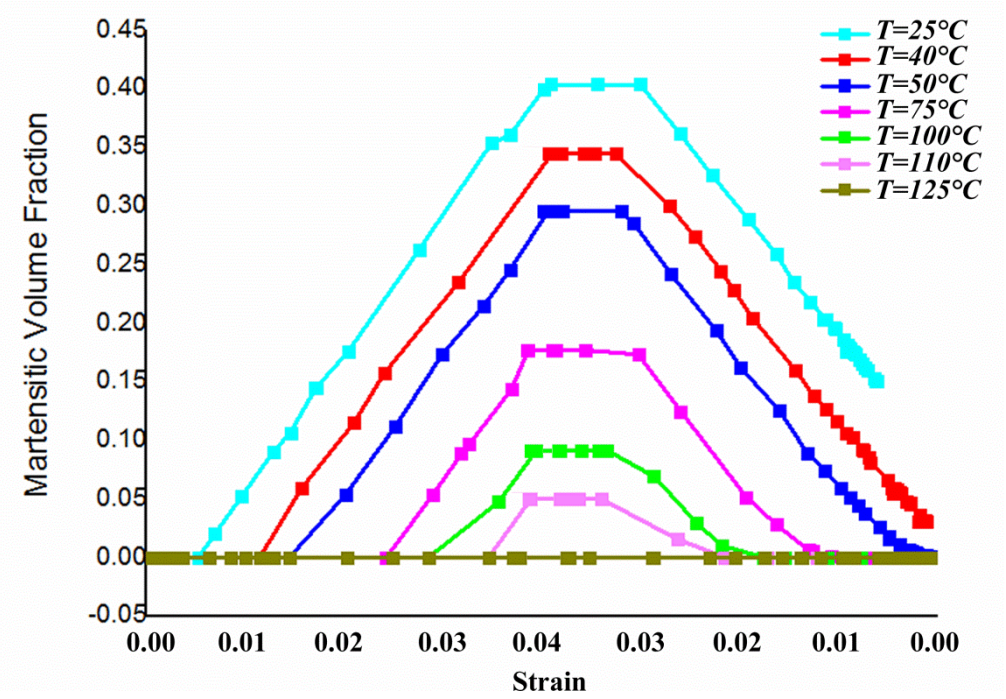

Fig.5.3 The change of martensitic volume fraction under high strain rate deformation (600/s) at various temperatures

The change of temperature is related to the evolution of the martensitic volume fraction in equation (12). The change of martensitic volume fraction with strain is shown in Fig. 5.3. The strain when the phase transformation starts increases with increasing temperature. The strain for full recovery from the reverse phase transformation also increases with increasing temperature. At the temperature of M_d, no phase transformation is observed and the martensitic volume fraction is zero during the deformation. According to Fig. 5.3, the strain for the maximum martensitic volume fraction related to the phase transformation appears to occur at a value of ~0.37 strain during loading, irrespective of temperature. The reverse phase transformation is activated when the sample is unloaded to the strain around 0.03. The little fluctuation of the strain to initiate reverse transformation is due to the competing of temperature softening and strain rate hardening. The residual martensitic volume fraction is about 0.15 when the sample is deformed at room temperature. It decreases to about 0.04

when the sample is deformed at 40 ℃. The martensitic transformation is fully recovered when the sample is deformed at a temperature higher than 50 ℃. The maximum martensitic volume fraction during the deformation is related to the temperature. It decreases from 0.42 at room temperature to 0.05 at the temperature of 110 ℃. Therefore, the maximum martensitic volume fraction decreases with increasing temperature up to M_d.

The distribution of martensite during high strain rate deformation at various temperatures is shown in Fig. 5.4. The phase transformation band structure is clearly observed during the loading and unloading process at temperatures lower than 50 ℃. At the temperature of 75 ℃, the transformation band structure is blurred and indistinct. The band structure disappears at temperatures above 75 ℃. More martensite is observed at the periphery of the sample. At M_d, no martensitic phase is observed. According to the change of martensitic volume fraction with strain at various temperatures shown in Fig. 5.3, the critical martensitic volume fraction to form a transformation band is 0.18. When the martensitic volume fraction is lower than the critical value, no phase transformation band structure is observed during deformation. The relationship between the start strain when the transformation is activated and temperature is also shown clearly in Fig. 5.4. According to Fig. 5.3, the strain at which the phase transformation starts increases with increasing temperature. The reverse phase transformation finishes earlier at high strain levels during the unloading process. According to Fig. 5.4, the microstructure at a strain of 0.04 changes little during the loading and unloading process. It can also be concluded from Fig. 5.4 that the martensitic volume fraction at each strain decreases with temperature, which means that increasing temperature hinders the martensitic transformation.

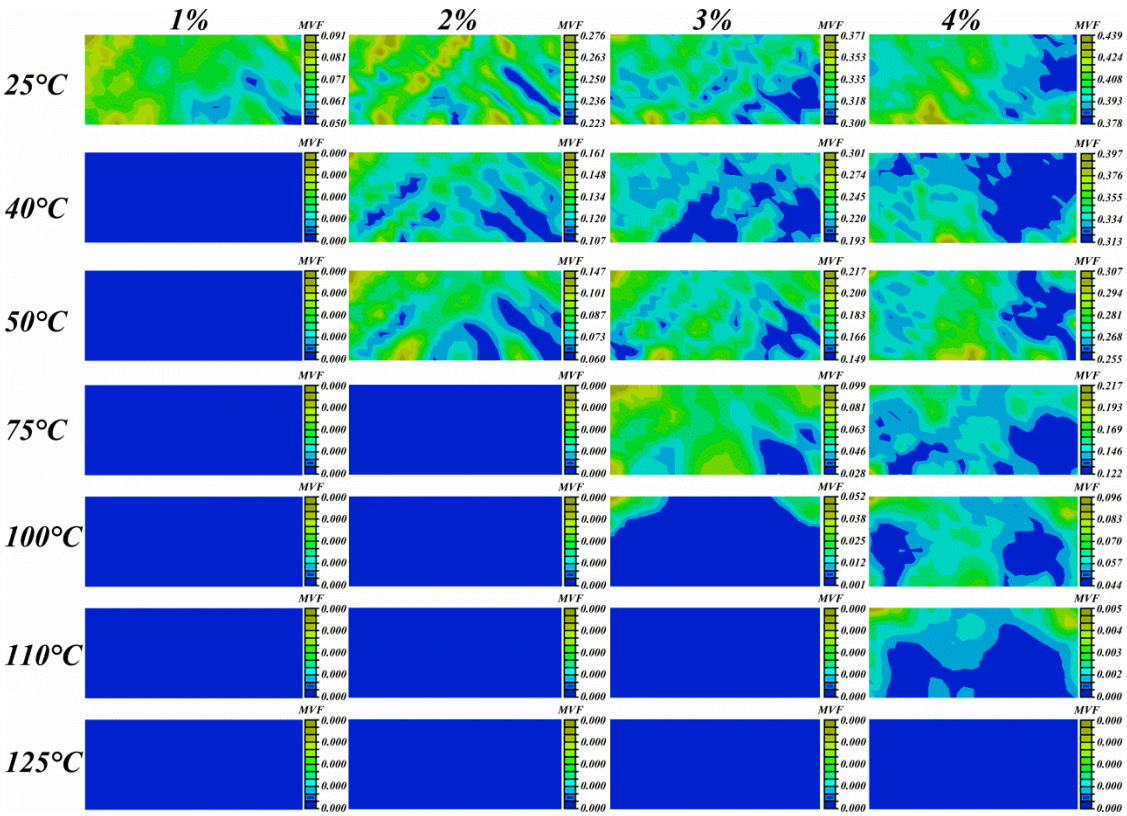

(a) Distribution of martensite during the loading process

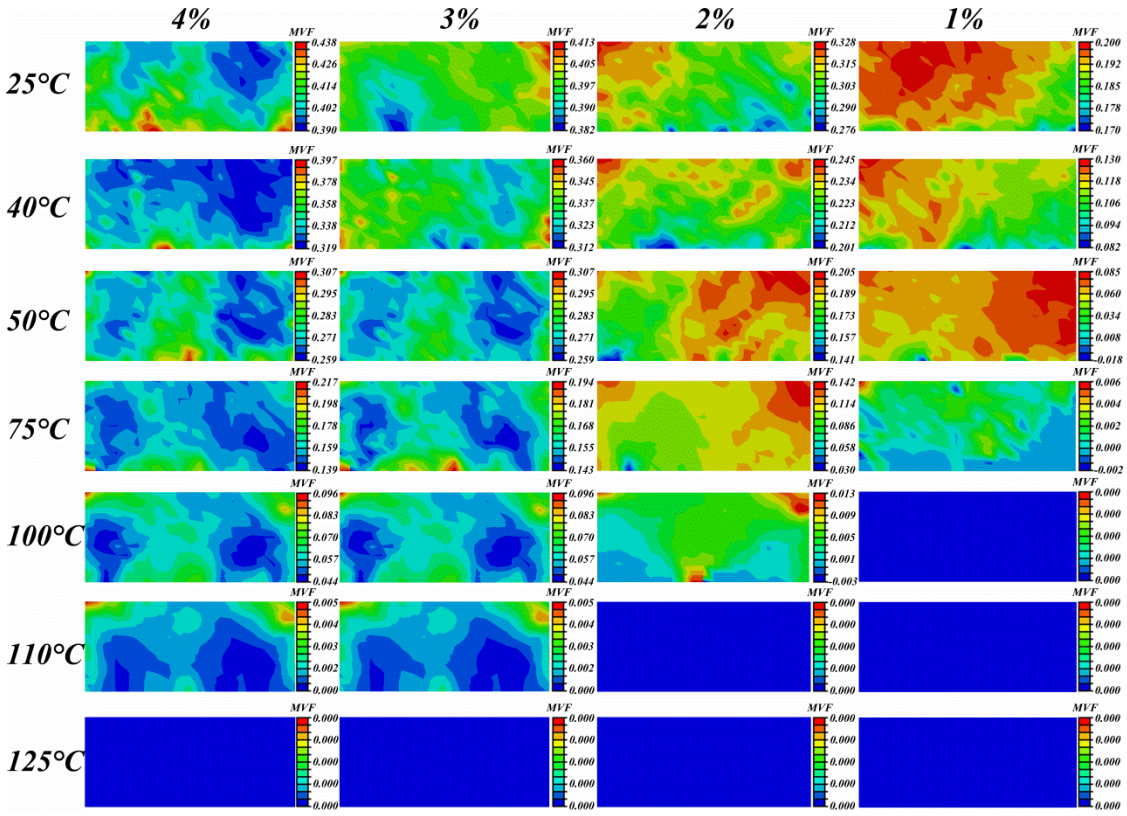

(b) Distribution of martensite during unloading process

Fig.5.4 Distribution of martensite under high strain rate deformation at various temperatures

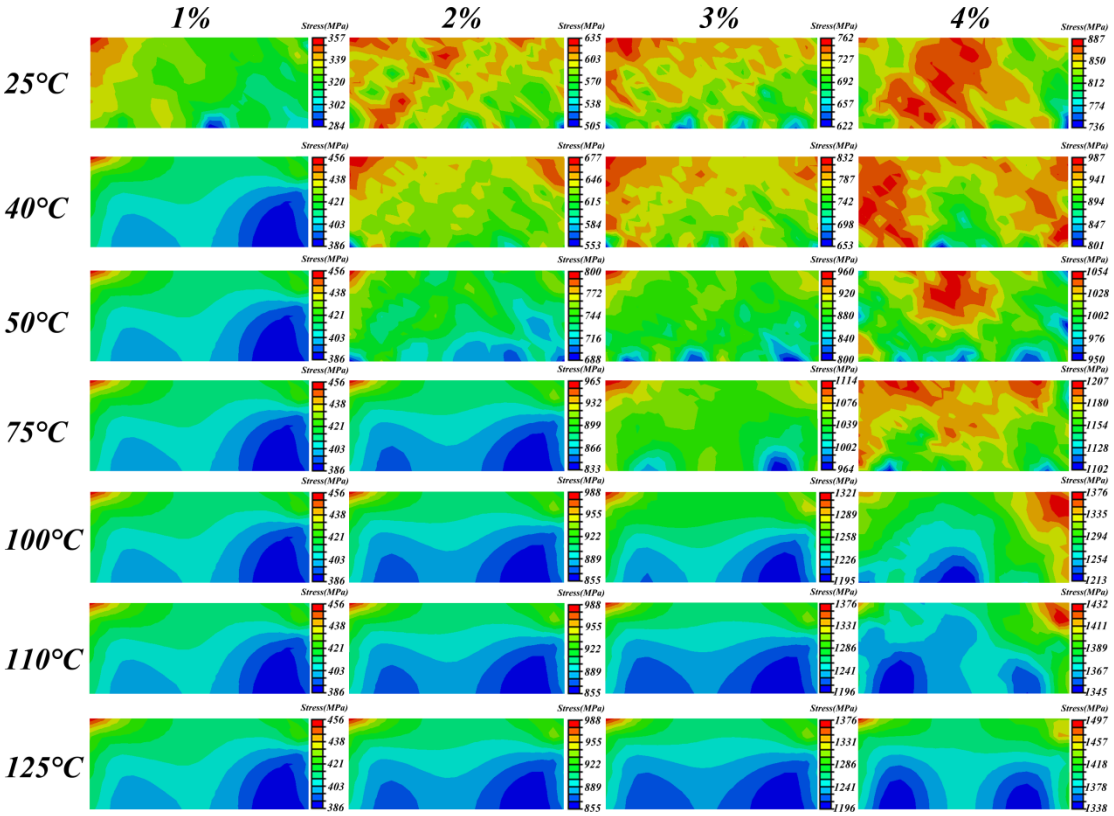

(a) Stress distribution during the loading process

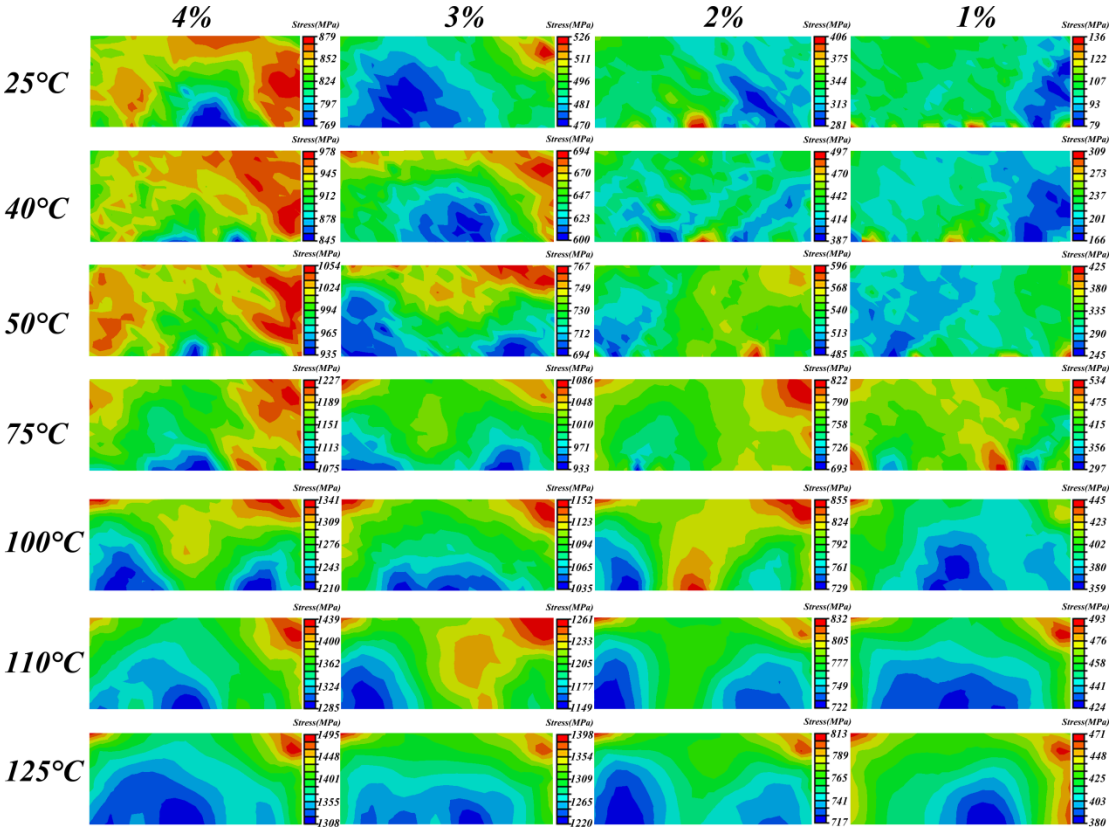

(b) Stress distribution during the unloading process

Fig.5.5 Distribution of stress under high strain rate deformation at various temperatures

The stress distribution during the loading and unloading process at various temperatures is shown in Fig. 5.5. Similar to the microstructure shown in Fig. 5.4, a distinct difference in the stress distribution between the elastic deformation and phase transformation is observed. Elastic deformation is the main mechanism for the high strain rate deformation at higher temperatures. At temperatures higher than 100 ℃, nearly no phase transformation is observed. The distribution of the stress is close to that of pure elastic deformation although the phase transformation is observed in Fig. 5.4. According to Fig. 5.4, martensite disperses within the sample without the formation of the transformation band structure at higher temperatures. Therefore, the contribution of the martensitic transformation to the stress distribution is limited at higher temperatures. According to Fig. 5.5, the average stress at a strain of 0.01 at room temperature is about 300 MPa. The maximum stress is 357 MPa and the minimum stress is 284 MPa. The average stress increases to about 400 MPa at temperature higher than room temperature. The maximum and minimum stress is 456 MPa and 386 MPa, respectively, for all the temperatures higher than 25 ℃, which indicates that the elastic deformation during the loading process is insensitive to temperature. The same phenomenon is observed at elastic deformation at higher strain levels. Unlike the loading process, the stress in the elastic unloading process at the same strain for different temperatures differs. Although a similar distribution of the stress is observed during the elastic unloading of the sample, the influence of the martensitic phase leads to the variation in stress.

5.4.2 Temperature Effect on the Deformation at Various High Strain Rates

The influence of temperature and strain rate to the stress-strain curve of SMAs is

compared in this section. The temperature effect on the deformation at various high strain rates is shown in Fig. 5.6. Similar to the result on the deformation at the strain rate of 600/s discussed in section 5.4.1, the increasing temperature leads to the increase of the start stress for the phase transformation at the strain rate of 1000/s, 2000/s and 5000/s. As we discussed before, the influence of the temperature on the stress strain curve can be represented by the term $d\sigma/dT|\varepsilon = \varepsilon_0$. At the strain of 0.03 during the loading process, phase transformation is fully activated for nearly all the temperatures at all three strain rates. Therefore, ε_0 is selected as 0.03 for the loading process. For the same reason, ε_0 is selected as 0.02 for the unloading process. $d\sigma/dT$ equals to 7.5 MPa/℃, 6.5 MPa/℃, 5.0 MPa/℃ for the strain rate of 1000/s, 2000/s, 5000/s, respectively, during the loading process and 6.6 MPa/℃, 6.4 MPa/℃, 4.1 MPa/℃ for the strain rate of 1000/s, 2000/s, 5000/s, respectively, during the unloading process. Therefore, the increasing temperature has less influence on the stress-strain cure when strain rate increases. According to Fig. 5.6a and b, the maximum stress during deformation at room temperature changes from 873 MPa to 904 MPa when the strain rate increases from 1000/s to 2000/s. According to Fig. 5.6a, the maximum stress during deformation at the strain rate of 1000/s increases from 873 MPa to 973 MPa when the temperature increases from 25℃ to 40℃. Therefore, the deformation is more sensitive to the temperature than the strain rate. The same result is concluded in the experimental research by Nemat-Nasser et al. [9] on the high strain rate deformation of austenitic NiTi SMAs at various temperatures. According to Fig. 5.6, the linear elastic deformation during the high strain rate deformation is observed at the temperature of 120℃ for all the strain rates. Therefore, the M_d temperature is insensitive to the strain rate and is about 100℃ higher than

the A_f temperature. The influence of temperature and strain rate on the hysteresis area is also shown in Fig. 5.6. Note that increasing of both temperature and strain rate will lead to the decrease of hysteresis area. The hysteresis area is more sensitive to the temperature than the strain rate.

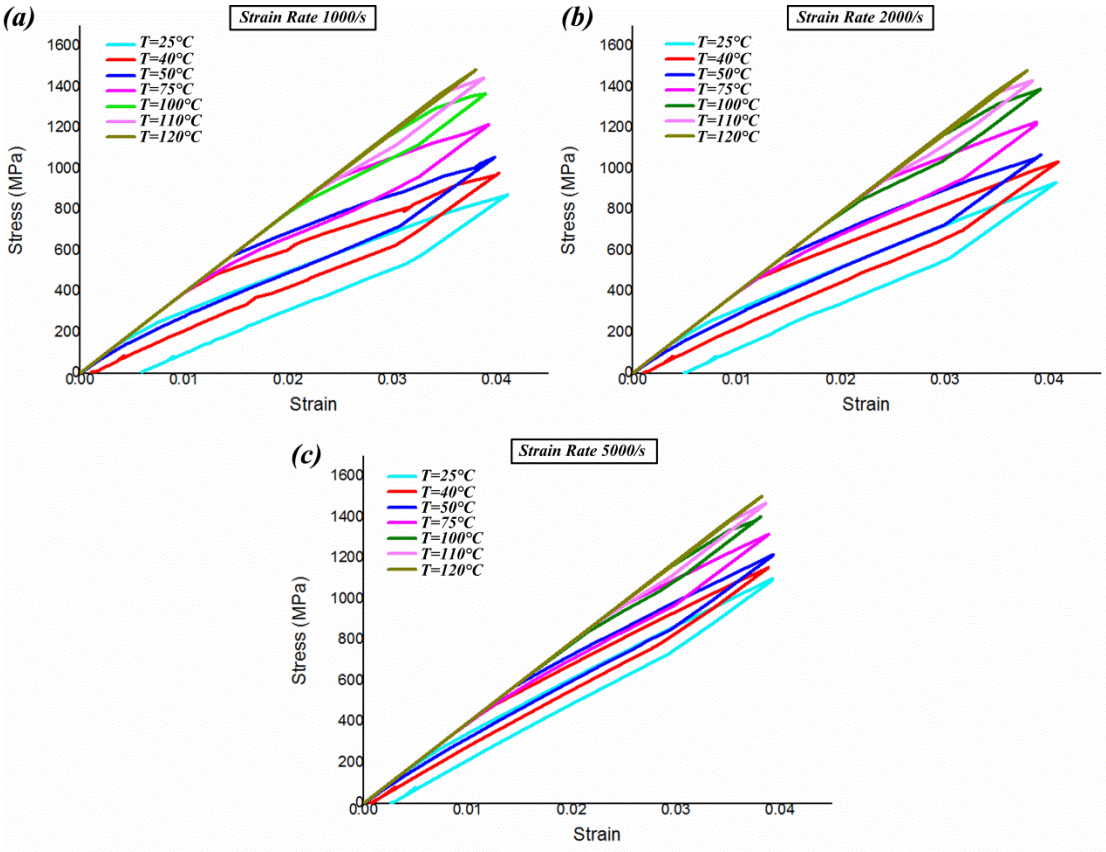

Fig.5.6 Temperature effect on the stress-strain curve at various strain rates

The change of temperature with strain during deformation at various temperatures and strain rates is shown in Fig. 5.7. Note that the temperature increases during the loading process and decreases during the unloading process for the deformation at all strain rates and temperatures below M_d. The temperature increment is 21.2 ℃ when the sample is deformed under the strain rate of 1000/s at room temperature. The temperature increment is 18.8 ℃ and 12.4 ℃ for the strain rate of 2000/s and 5000/s, respectively, at the same temperature. The temperature increment is 17.7 ℃ when the sample is deformed at 40 ℃ under strain rate of

1000/s. The temperature increment is 16.7 ℃ and 10.7 ℃ under the strain rate of 2000/s and 5000/s at temperature of 40 ℃. The temperature increment is 15.3 ℃, 14.1 ℃, and 9.8 ℃ for the strain rate of 1000/s, 2000/s and 5000/s, respectively, when sample is deformed at 50 ℃. Therefore, the temperature increment decreases with increasing strain rates and temperatures. When the sample is deformed at 110 ℃, the temperature increment is about 2-3 ℃ for all the strain rates. Therefore, the temperature increment is more and more insensitive to the strain rate when temperature increases.

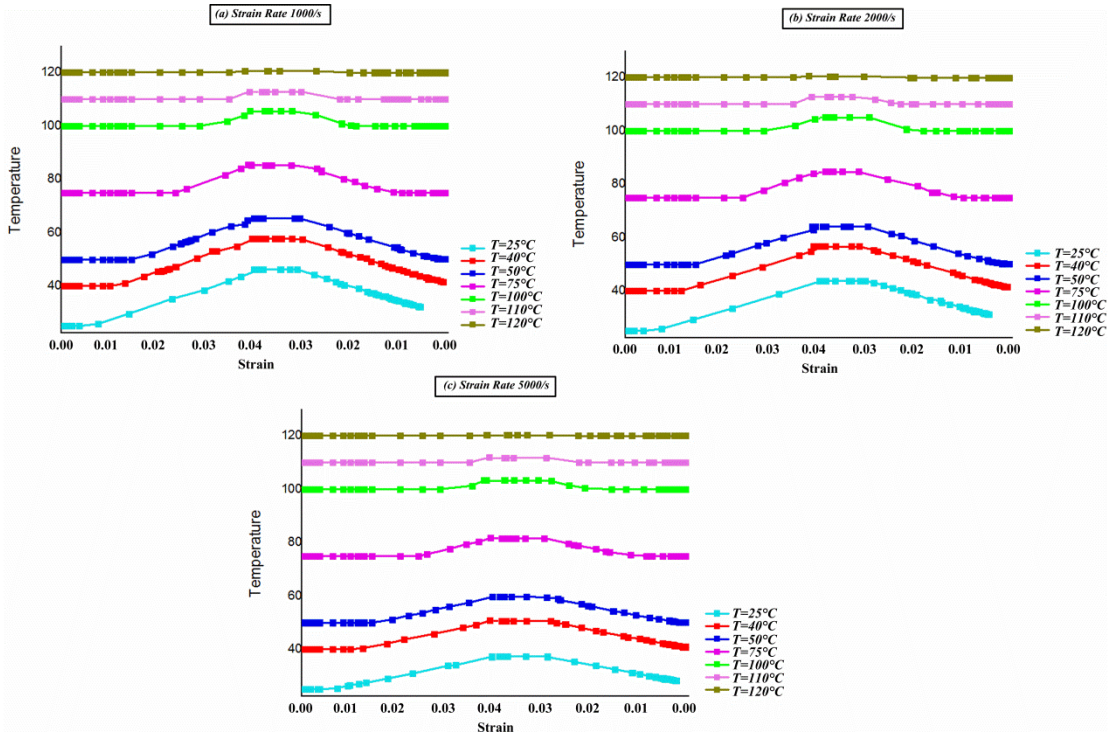

Fig.5.7 Temperature change of austenitic NiTi SMAs at various ambient temperatures under high strain rate deformation (a) 1000/s (b) 2000/s (c) 5000/s

The influence of the strain rate and temperature to the maximum temperature during the deformation is also shown in Fig. 5.7. The maximum temperature during the deformation increases with both increasing strain rate and temperature. When the sample is deformed at temperature higher than 100 ℃, the maximum temperature during deformation is nearly the same for different strain rates. Therefore, the maximum temperature is less sensitive to the

strain rate at high temperatures.

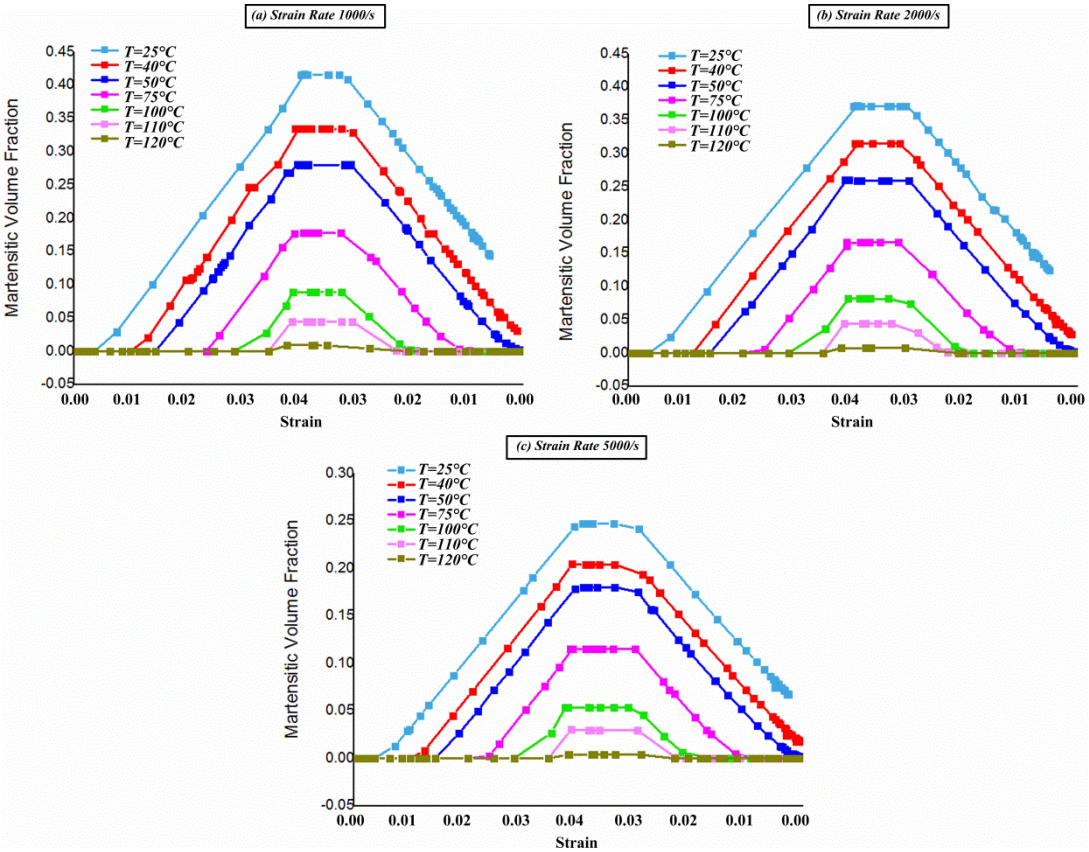

Fig.5.8 The change of martensitic volume fraction at various ambient temperatures under high strain rate deformation (a) 1000/s (b) 2000/s (c) 5000/s

The influence of temperature on the martensitic volume fraction during deformation at various strain rates is shown in Fig. 5.8. The peak value of martensitic volume fraction changes from 0.42 at strain rate of 1000/s to 0.37 and 0.25 at strain rate of 2000/s and 5000/s, respectively, when the sample is deformed at room temperature. The peak value of martensitic volume fraction changes from 0.33 at strain rate of 1000/s to 0.32 and 0.21 at strain rate of 2000/s and 5000/s, respectively, when the sample is deformed at 40 ℃. The maximum martensitic volume fraction when sample is deformed at 1000/s changes from 0.42 at 25 ℃ to 0.05 at 110 ℃. Therefore, the maximum volume fraction of martensite during deformation decreases with increasing temperature and strain rate.

While this new macroscopic thermomechanical finite element model captures the effect

of temperature during high strain rate deformation of austenitic NiTi SMAs, the model would benefit from experimental validation.

5.5 Conclusions

A macroscopic thermomechanical finite element model, which examines the effect of temperature on high strain rate deformation of austenitic NiTi SMAs, is presented in this paper. This model expands upon a previous model to include the effect of temperature. The following observations can be made based on simulations from this model:

- The start stress for the transformation increases with increasing temperature and the stress-strain slope during the phase transformation remains nearly constant at a constant high strain rate.
- Transformation bands form during deformation at temperatures lower than 75 ℃. The start strain for initiation of the transformation bands increases with increasing temperature.
- The maximum martensitic volume fraction decreases with increasing temperature up to M_d. Pure elastic deformation is observed when the sample is deformed at M_d. M_d is ~100 ℃ higher than A_f.
- Phase transformation is more sensitive to temperature than strain rate. M_d is insensitive to strain rate.

Experimental validation of the model is needed to determine the accuracy of the new model.

5.6 References

[1] Otsuka K, Ren X. Intermetallics 1999;7:511.

[2] Shaw JA, Kyriakides S. Journal of the Mechanics and Physics of Solids 1995;43:1243.

[3] Yin H, He Y, Sun Q. Journal of the Mechanics and Physics of Solids 2014;67:100.

[4] Benafan O, Noebe RD, Padula SA, Garg A, Clausen B, Vogel S, Vaidyanathan R. International Journal of Plasticity 2013;51:103.

[5] Chen W, Song B. Journal of Mechanics of Materials and Structures 2006;1:339.

[6] Nemat-Nasser S, Yong Choi J, Guo W-G, Isaacs JB, Taya M. Journal of Engineering Materials and Technology 2005;127:83.

[7] Nemat-Nasser S, Choi J-Y, Guo W-G, Isaacs JB. Mechanics of Materials 2005;37:287.

[8] Nemat-Nasser S, Choi JY. Acta Materialia 2005;53:449.

[9] Nemat-Nasser S, Guo W-G. Mechanics of Materials 2006;38:463.

[10] Elibol C, Wagner MFX. Materials Science and Engineering: A 2015;643:194.

[11] Qiu Y, Young ML, Nie X. Metallurgical and Materials Transactions A 2016:1.

[12] Qiu Y, Young ML, Nie X. Metallurgical and Materials Transactions A 2015;46:4661.

[13] Qiu Y, Young ML, Nie X. Shape Memory and Superelasticity 2015;1:310.

[14] Ahadi A, Sun Q. Acta Materialia 2014;76:186.

[15] Adharapurapu RR, Jiang F, Bingert JF, Vecchio KS. Materials Science and Engineering: A 2010;527:5255.

[16] Niemczura J, Ravi-Chandar K. Journal of the Mechanics and Physics of Solids 2006;54:2136.

[17] Chowdhury P, Patriarca L, Ren G, Sehitoglu H. International Journal of Plasticity

2016;81:152.

[18] Chatziathanasiou D, Chemisky Y, Chatzigeorgiou G, Meraghni F. International Journal of Plasticity 2016;82:192.

[19] Yu C, Kang G, Kan Q, Zhu Y. International Journal of Plasticity 2015;72:60.

[20] Yu C, Kang G, Kan Q. Journal of the Mechanics and Physics of Solids 2015;82:97.

[21] Yu C, Kang G, Kan Q. Mechanics of Materials 2014;78:1.

[22] Yu C, Kang G, Kan Q. International Journal of Plasticity 2014;54:132.

[23] Lagoudas D, Bo Z. International Journal of Engineering Sciences 1999;37:1141.

[24] Lagoudas D, Hartl D, Chemisky Y, Machado L, Popov P. International Journal of Plasticity 2012;32-33:155.

[25] Lagoudas DC. Shape memory alloys: modeling and engineering applications: Springer Science & Business Media, 2008.

[26] Lagoudas DC, Entchev PB. Mechanics of Materials 2004;36:865.

[27] Lagoudas DC, Ravi-Chandar K, Sarh K, Popov P. Mechanics of Materials 2003;35:689.

[28] Hartl DJ, Chatzigeorgiou G, Lagoudas DC. International Journal of Plasticity 2010;26:1485.

[29] Hao Yu, Marcus Yong, ‘Three-dimensional modeling of high strain rate deformation of austenitic shape memory alloys”, in press in Smart Materials and Structures, November (2017)

CHAPTER 6

CONCLUSIONS AND FUTURE WORK

6.1 Conclusions

A new phenomelogical model for high strain rate deformation of austenitic SMA derived in present study. The model is based on the second law of thermodynamics and is calibrated by experimental results.

A one-dimensional rate-dependent phenomelogical model is develped in the first part of this work. Compared to quasi-static deformation of SMA, high strain rate deformation of SMA leads to a high temperature increase in a short time. The impact deformation of SMA is therefore treated as adiabatic process. The driving force for martensitic phase transformation is related to latent heat generated during deformation and the interaction of dislocations. The new term ‘transformation resistance due to dynamic loading’ is presented to describe the influence of dislocation on phase transformation during dynamic deformation of SMA. Transformation resistance due to dynamic loading is related to wave front speed and martensitic volume fraction by the power law equation. The simulated stress strain relationship at various high strain rates matches well with the experiment [1].

Following J2 type flow rule, a three-dimensional model for high strain rate deformation of SMA on Kolsky compressive bar was developed in the second part of this work. Martensitic transformation is related to Von-Mises equivalent stress. The relationship between Von-Mises equivalent stress and strain is calibrated experimentally, and simulated results match well with experiment [1]. Finite element analysis software ABAQUS/Standard was applied to simulate the distribution of stress, strain and martensitic volume fraction

during high strain rate deformation. According to current work, microscopic phase transformation band is observed during deformation under critical high strain rate. The phase transformation band is sensitive to strain rates. At strain rate higher than 2000/s, the microscopic bands disappear and transformation happens everywhere within the sample.

Based on the model developed in Chapters 1 and 2, the effect of temperature on material flow behavior at high strain rate compression of austenitic SMA was studied in Chapter 3. Deformation is studied at temperatures ranging from the martensitic start temperature (M_s) to the temperature (M_d) above which stress-induced martensite no longer forms. Result shows that martensitic transformation is inhibited with increasing temperature. At temperature higher than M_d, no phase transformation was observed. The coupling of strain rate effect and temperature on phase transformation was also studied. Phase transformation is more sensitive to temperature than strain rate. *Md* is about 100℃ higher than A_f, which is insensitive to strain rate. Residual martensite observed after unloading of the sample leads to residual strain after high strain rate deformation.

6.2 Future Work

A new rate-dependent model was established to simulate high strain rate compression of austenitic SMAs. Planned follow-on work is described below.

1. Current work was limited to the pseudoelastic deformation of austenitic SMAs. When deformation of SMAs is larger than a critical value (usually about 6%~10%), plastic deformation occurs. Plastic deformation of SMAs is sensitive to strain rate and temperature, especially at high strain rate deformation. Thus, study of the coupling of phase transformation and plastic deformation at high strain rate deformation of SMA is warranted.

2. A model for high strain rate deformation of martensitic SMAs needs to be developed. Experimental study shows that deformation of martensitic SMAs is strain-rate sensitive. Hence, strain rate effect on the reorientation of martensitic variants needs to studied.

3. High strain rate tensile deformation on austenitic SMAs need to be studied. Since experimental results show Luder-like band structures form during high strain rate tension of austenitic SMAs the strain rate effect on Luder band needs to be studied.

6.3 References:

[1] Nemat-Nasser S, Yong Choi J, Guo W-G, Isaacs JB, Taya M. Journal of Engineering Materials and Technology 2005;127:83.

APPENDIX A

EXPERIMENTAL RESULTS

Experimental investigation on high strain rate deformation of austenitic NiTi SMAs was performed using a modified Kolsky compression bar. According to one-dimensional wave theory, stress, strain, and strain rate of the sample can be calculated in the form of transmitted and reflected pulse as:

$$\begin{cases} \dot{\varepsilon}_s(t) = -\frac{2C_0}{L_s}\varepsilon_R(t) \\ \varepsilon_s(t) = -\frac{2C_0}{L_s}\int_0^t \varepsilon_R(\tau)d\tau \\ \sigma(t) = \frac{A_0 E}{A_S}\varepsilon_T(t) \end{cases} \quad \text{(A1)}$$

where $\dot{\varepsilon}_s(t)$ is the strain rate history of the specimen, L_s is the length of the specimen, C_0 is the elastic wave velocity of the steel bars, $\varepsilon_R(t)$ is the strain history of the reflected pulse, $\varepsilon_S(t)$ is the strain history of the specimen, $\sigma(t)$ is the stress history of the specimen, A_0 is the cross-sectional area of the bar, and A_S is the initial cross-sectional area of the specimen.

Austenitic NiTi SMA (50.8 at.% Ni, named as SE508) rod samples with an aspect ratio of 1:1 were studied during high strain rate deformation. The rod length is 6.10 mm and the rod diameter is Φ 6.21 mm. Homogenization was performed at 800 ℃ for 5 h before deformation. After homogenization, the sample was heat treated at 550 ℃ for 1 h. A copper plate used as the pulse shaper, insured constant strain rate deformation on the sample. The sample was deformed to 4% strain. The incident, transmitted, and reflected waves are shown in Fig. A1; note that both incident and transmitted waves have a triangular pulse structure. Whereas the duration of the incident pulse is about 0.2 ms, and the duration of the transmitted wave is about 0.3 ms, the reflected wave has a plateau at the peak of the pulse, which represents constant strain rate deformation. Strain rate can be calculated from equation (A1), and the distribution of strain rate with time is shown in Fig. A1. Strain rate increases at the beginning of the deformation when elastic deformation of the material is activated and

remains constant at 600/s during the activation of phase transformation. Stress and strain can be calculated from equations (A1). The stress-strain relationship at high strain rate deformation is shown in Fig. A2. According to the experimental result, the elastic modulus is 35 GPa and 28 GPa for austenitic and martensitic phases, respectively. Stress to activate phase transformation is 300 MPa. Unlike the stress plateau often observed in quasi-static deformation, an apparent increase of stress during deformation is shown in the pseudoelastic region.

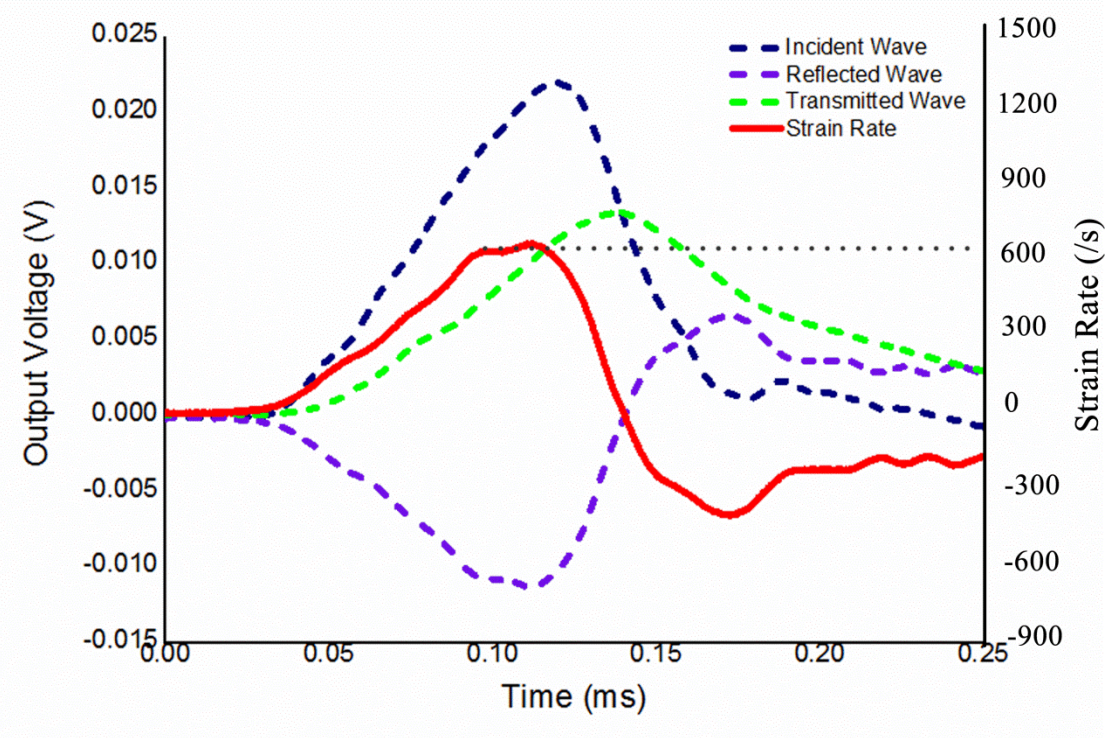

Fig.A1 Stress wave and strain rate distribution in the sample

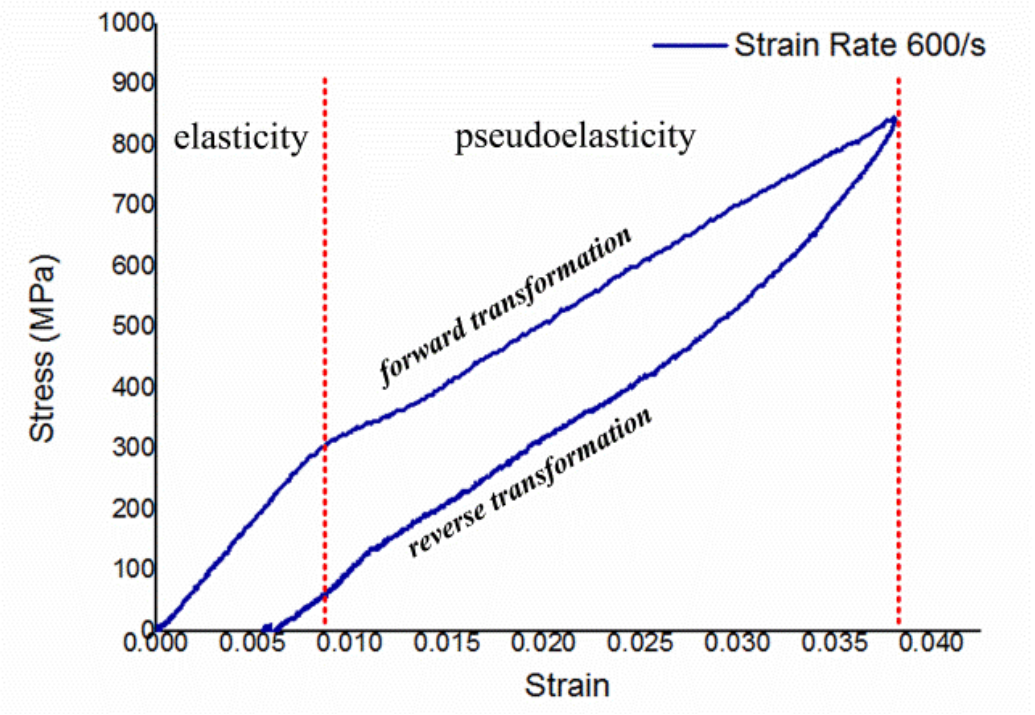

Fig.A2 Stress-strain curve of NiTi rod under deformation with strain rate 600/s

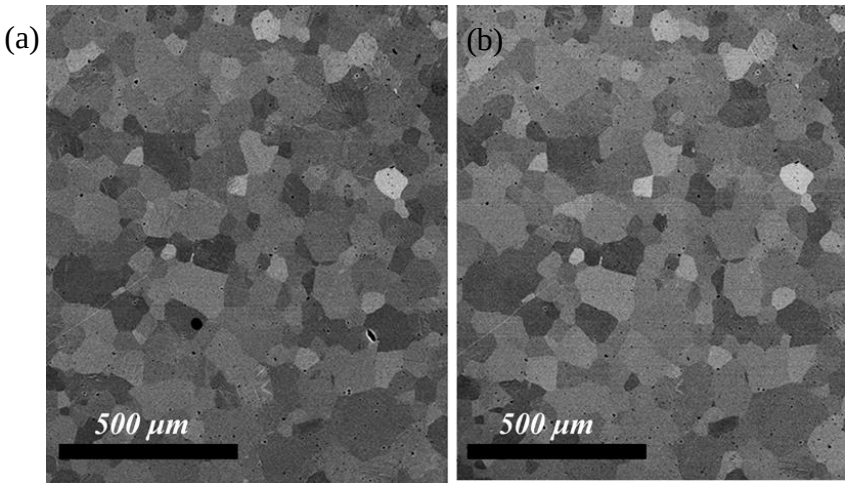

Fig.A3 SEM images from the cross-section of top surface of the austenitic NiTi SMA (a) before and (b) after deformation

Scanning electron microscopy (SEM) and electron backscattered diffraction (EBSD) were performed on FEI Nova 200 NanoLab instrument to detect microstructural changes before and after deformation (Fig. A3 and A4). The average grain size of the sample after heat treatment is 65.4 μm (Fig. A3). The grain structure is the same before and after high strain rate deformation. Microstructural evolution is indicated by the pole figures in Fig. A4. Note that crystal orientation is nearly the same before and after deformation; the only

difference is that a slight rotation of the grain is observed (for example, the (111) planes align more in RD and TD after deformation) and the texture strength increases from 9.1 to 10.4 after deformation. Also after deformation, the specimen is nearly fully recovered (only 0.5% unrecoverable strain), to 4% strain at strain rate 600/s.

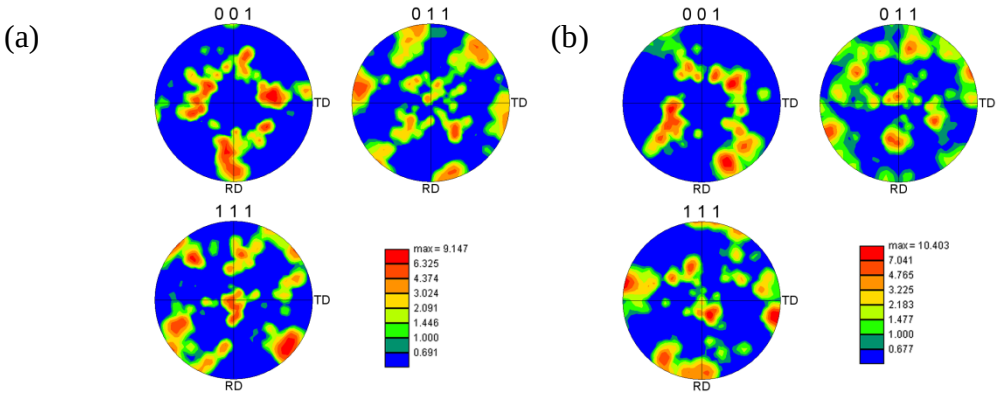

Fig.A4 Pole figures (a) before deformation (b) after deformation

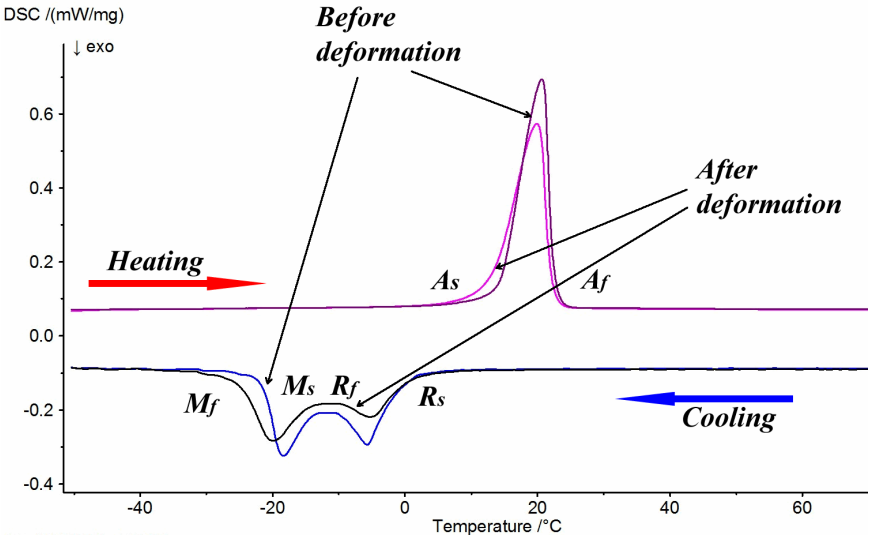

Fig.A5 DSC curve before and after deformation

Changes of phase transformation temperatures before and after deformation are detected by a Netzsch DSC 204 FI Phoenix differential scanning calorimeter (DSC). Start and finish temperatures for austenitic and martensitic phase transformation are A_s, A_f, M_s, and M_f, respectively. Phase transformation temperatures of the sample before deformation are

$M_s = 273K,\ M_f = 253K,\ A_s = 285K,\ A_f = 295K$ (Fig. A5). Figure A5 also shows that the martensitic transformation during cooling is a two-step process, which likely is the result of a B2 to R-phase transformation and R-phase to B19$^{'}$ phase transformation, respectively. Our model does not consider the two-step process and only takes into account the transformation as a whole, i.e. input parameters R_s, and M_f only. The DSC curves show that after deformation, the peak for both austenitic transformation and martensitic transformation are nominally unchanged, although a small amount of broadening has occurred which also appears as an overall decrease in peak intensity, which indicates a small microstructural change after deformation and is confirmed by the slight texturing observed in the pole figures in Fig A4 and in the macroscopic stress-strain curve (Fig A2) which exhibits about 0.5% unrecoverable strain. These changes are to be studied by computer simulation in the following sections.

APPENDIX B

DERIVATION OF INTERNAL ENERGY

The internal energy per mass of RVE is *U*, which is related to enthalpy *H* and work done on the RVE by

$$H = U + \frac{1}{\rho}\sigma\varepsilon \tag{B1}$$

where σ and ε are the macroscopic stress and strain. The Gibbs free energy *G* is related to enthalpy *H* and entropy *S* by

$$G = H\text{-}TS \tag{B2}$$

Therefore, the internal energy *U* can be written as:

$$U = G + TS - \frac{1}{\rho_0}\sigma\varepsilon \tag{B3}$$

APPENDIX C

WAVE VELOCITY DURING PHASE TRANSFORMATION

According to wave theory, the wave velocity C_P can be solved by the following equation:

$$C_P = \sqrt{\frac{1}{\rho_0}\frac{d\sigma}{d\varepsilon}} \quad \text{(C1)}$$

The stress-strain curve for NiTi SMA deformed at strain rate 2500/s is shown in Fig. 3.4. A linear stress-strain relationship is observed in the stress-strain curve. According to the current model, when strain equals 0.025, the stress is about 800 MPa. When strain equals 0.035, the stress is about 1000 MPa. In the current model, the density ρ_0 is selected as 6450 kg/m^3. Thus, the wave velocity C_P is solved as:

$$C_P = \sqrt{\frac{1}{\rho_0}\frac{d\sigma}{d\varepsilon}} = \sqrt{\frac{1}{6450}\frac{1000\times10^6-800\times10^6}{0.035-0.025}} = 1760\ \mathrm{m/s} \quad \text{(C2)}$$

A linear relationship between strain rate and wave velocity is assumed in the current model as follows:

$$C_P = 0.73\dot{\varepsilon} = 1825\ m/s \quad \text{(C3)}$$

The error can be calculated as:

$$e\% = \frac{1825-1760}{1760} = 0.037 \quad \text{(C4)}$$

which means the linear relationship between the wave velocity and strain rate provides a good prediction of the wave velocity in the current model.

APPENDIX D

RELATIONSHIP BETWEEN PLASTICITY AND MARTENSITE

Both the yielding of austenitic and martensitic materials and the existence of retained martensite can be attributed to plastic deformation of the material. Experimental results in Chapter 3 and 4 show no yielding of the austenitic and martensitic phase when NiTi SMA is deformed below 6% strain. Therefore, the unrecovered strain observed experimentally is asumed to be due to retained martensite. In the current model, a large resistance is assumed to present during the forward and reverse transformation, leading to a large stress to activate the phase transformation and retained martensite after unloading. The relationship between plastic deformation ε_P and retained martensite ξ_r is given by

$$\varepsilon_P = H\xi_r \tag{D1}$$

Where H is the maxmim strain during deformation. According to Fig. 4.7, $\xi_r = 20\%$ and the plastic strain is calculated as:

$$\varepsilon_P = H\xi_r = 0.05 \times 20\% = 0.01 \tag{D2}$$

which is the same as shown in the stress-strain curve in Fig. 4.4.

APPENDIX E

THERMODYNAMICS AT HIGH STRAIN RATE DEFORMATION

The deformation state in the model in a random plane is shown in Fig.E1. The stress-strain and particle velocity at the end of loading is the same as defined in the above section. At time τ, the wave contains the phase transformation information for propagation to the *A-B* plane. Due to the one-dimensional deformation assumption, the stress and strain will remain constant across the cross section area. The stress is defined as σ_{AB} in Fig.E1. Time *t* stands for the time after the *A-B* plane has been impacted by the wave and, thus, contains phase transformation information. After a short time interval, the stress in the *A-B* plane will change from σ_t to $\sigma_{t+\Delta t}$. By defining τ = 0, *t* become the time associated with the austenitic phase transformation to martensitic phase at the stress σ_t. The whole deformation process discussed above is equivalent to a stress σ_{AB} loading of a rod in the *A-B* plane. In this case, $\sigma_{tr} = \sigma_{AB}$. In contrast to the constant stress σ^* of the experimental end of loading, the stress at the *A-B* plane after time *t* has the same value as the stress at position $(x_{AB} - C_0 t)$ at time τ. Although it can be assumed that a constant stress is maintained at a short time interval Δ*t*, the stress changes with time. A constant transformation rate is assumed at a small time interval in the model. To solve the stress, thermodynamic equations are needed to add to the wave field equations.

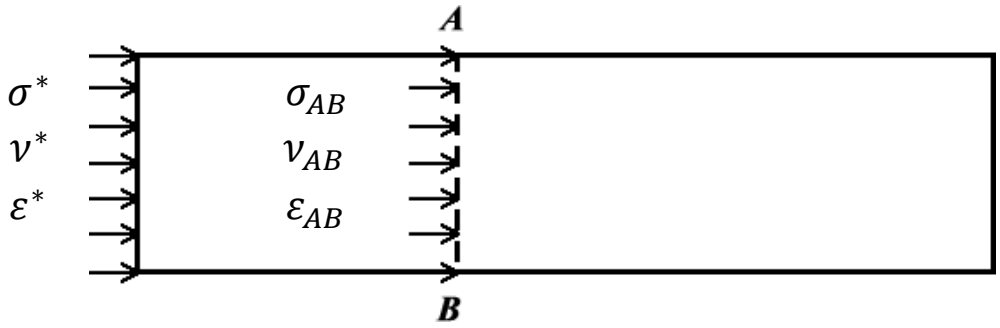

Fig.E1 Schematic showing the deformation state in a random plane

During the impact loading of the material, deformation occurs in a short time and the

thermodynamic equilibrium cannot be satisfied in the material. The rod under deformation is seen as an isolated system where energy is conserved at any given time. Suppose the rod has a cross section of A_0 and according to the energy conservation in a short time interval Δt, the following equation can be derived:

$$(\sigma_t v_t - \sigma_{t+\Delta t} v_{t+\Delta t}) A_0 dt + (U_t - U_{t+\Delta t}) \rho_0 A_0 dx + \frac{1}{2}(v_t^2 - v_{t+\Delta t}^2) \rho_0 A_0 dx = 0 \quad \text{(E1)}$$

The first term in the equation represents the work by the applied stress. The second term represents the internal energy change in the material. The third item is the change in kinetic energy. The equation can be rewritten as:

$$[\sigma v] + \rho_0 C_0 [U] + \frac{1}{2} \rho_0 C_0 [v^2] = 0 \quad \text{(E2)}$$

The evolution rate of internal energy can be derived from equation E2 as:

$$\rho_0 C_0 \frac{U_{t+\Delta t} - U_t}{\Delta t} = -\sigma \frac{v_{t+\Delta t} - v_t}{\Delta t} - \frac{1}{2} \rho_0 C_0 \frac{v_{t+\Delta t}^2 - v_t^2}{\Delta t} \quad \text{(E3)}$$

By combining equation (3.23) into (E3), the following equation results:

$$\rho_0 \frac{\partial U}{\partial t} = \frac{1}{2} g_{tr} \dot{\xi} \sigma - \frac{1}{4} \rho_0 C_0^2 g_{tr}^2 \xi \dot{\xi} + \frac{1}{2} \rho_0 C_0 v_{AB} g_{tr} \dot{\xi} \quad \text{(E4)}$$

In the discussion above, it is assumed that the deformation occurs at a constant high ambient temperature. A more common case is that the sample is deformed in air. Thus, the whole procedure cannot be considered as an isothermal case. Therefore, the thermal energy should be taken into consideration.

To account for the thermal energy change, two terms, q as heat flux and r as the rate of internal heat generation, are then added to equation (E4) as:

$$\rho_0 \frac{\partial U}{\partial t} = \frac{1}{2} g_{tr} \dot{\xi} \sigma - \frac{1}{4} \rho_0 C_0^2 g_{tr}^2 \xi \dot{\xi} + \frac{1}{2} \rho_0 C_0 v_{AB} g_{tr} \dot{\xi} + \rho_0 r - div(q) \quad \text{(E5)}$$

As we only take a small time interval into consideration, the first law of thermodynamics can be applied as:

$$U = G + TS - \frac{1}{\rho_0}\sigma\varepsilon \tag{E6}$$

According to (E6) , the partial differential equation of *U* can be written as:

$$\rho_0 \frac{\partial U}{\partial t} = \rho_0 \frac{\partial G}{\partial t} + \rho_0 T \frac{\partial S}{\partial t} + \rho_0 S \frac{\partial T}{\partial t} - \sigma \frac{\partial \varepsilon}{\partial t} - \varepsilon \frac{\partial \sigma}{\partial t} \tag{E7}$$

We can apply the second law of thermodynamics in the form of Clausius-Planck inequality as:

$$\rho_0 \frac{\partial S}{\partial t} + \frac{1}{T} div(q) - \frac{\rho_0 r}{T} \geq 0 \tag{E8}$$

Therefore, the driving force for phase transformation can be solved, which is discussed in detail in Chapter 3.

APPENDIX F

TEMPERATURE EFFECT ON THE STRESS-STRAIN CURVE

Experimental results on the temperature effect on the stress-strain curve of an SMA under high strain rate deformation is limited. Chen and Song [1] studied the temperature dependence of NiTi SMA's behavior at a high strain rate. The NiTi SMA is deformed in a temperature ranging from 0 ℃ to 50 ℃. The sample deforms in the austenitic state when the temperature is higher than 23 ℃. Therefore, the stress-strain curves for deformation at 35 ℃ and 50 ℃ are selected for comparision with simulated results, as shown in Fig. F1. According to Figure F, the current model provides a good prediction of the temperature effect on the stress-strain curve of an SMA during high strain rate deformation.

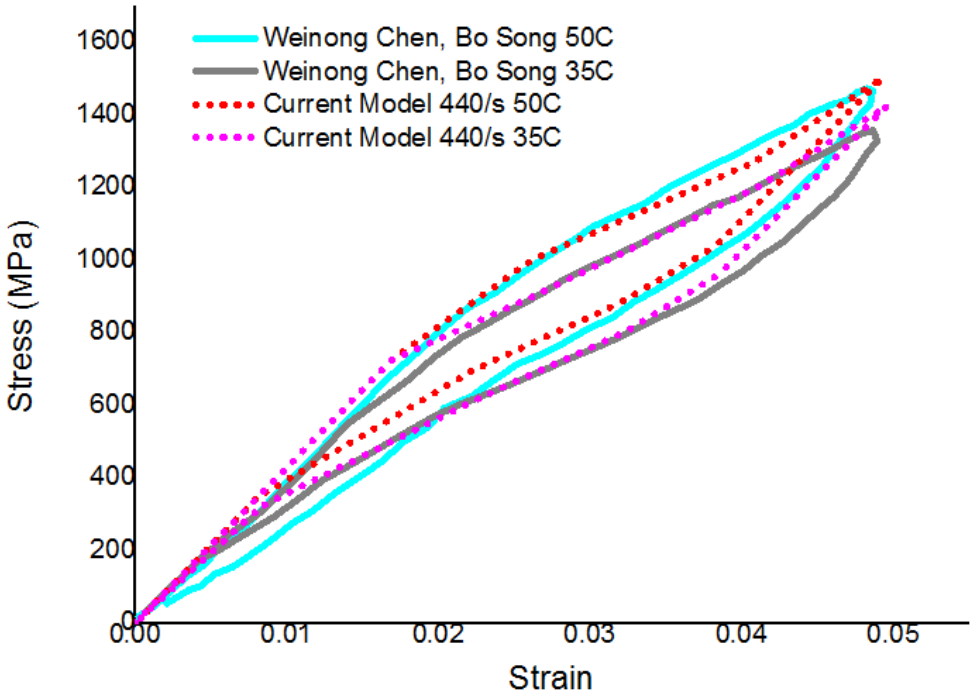

Fig.F1 Comparison of the experimental result [1], with current model and traditional model at strain rate 440/s at temperature 35 ℃ and 50 ℃

Reference:

[1] Chen W, Song B. Journal of Mechanics of Materials and Structures 2006;1:339.